Università degli Studi di Ferrara

DOTTORATO DI RICERCA IN
FISICA

CICLO XXVII

COORDINATORE Prof. Vincenzo Guidi

AN INNOVATIVE CYLINDRICAL MAGNETRON SPUTTERING SOURCE FOR THE DEPOSITION OF HIE-ISOLDE SUPERCONDUCTING Nb/Cu QWRs

Settore Scientifico Disciplinare FIS/03

Dottorando   **Tutore**

Dott. Daniel Adrien Franco Lespinasse   Prof. Vincenzo Palmieri

_____   _____

(firma)   *(firma)*

Anni 2012/2015

ACKNOWLEDGEMENTS

GENERAL CONTENT

FIGURE CONTENT

TABLE CONTENT

LIST OF ACRONIMS

SC: Superconductive/Superconducting.

ISOLDE: The On-Line Isotope Mass Separator.

QWRs; Quarter Wave Resonators.

CERN: European Organisation for Nuclear Research.

INFN: National Institute of Nuclear Physics.

LNL: National Laboratory of Legnaro (Italy).

SS: Stainless Steel.

RRR: Residual Resistivity Radio. The RRR is the residual resistivity radio that indicates the level of

purity in superconductive materials.

T_c: Critical temperature.

SEM: Scanning Electron Microscope.

NeFeB: Neodymium Iron Boron.

PVC: PolyVinyl Chloride.

RF: Radio Frequency.

SLAC: Standford Linear Accelerator Center.

ALPI: In italian (Acceleratore Lineare Per Ioni).

Eacc: Accelerating field

ESTRATTO

Nell'ambito del progetto Eucard è stato realizzato, in collaborazione con il CERN, l' R&D della tecnica di magnetron sputtering sulla geometria della cavità HIE-ISOLDE, come metodo alternativo per depositare film sottili di niobio. Nello specifico, presso i LNL dell'INFN è stata testata una nuova sorgente di campo magnetico per depositare un film sottile di niobio uniforme sul risonatore a quarto d'onda. La metodologia ha previsto tre fasi distinte. La prima fase, in cui un prototipo di cavità ed un catodo di prova sono stati usati per depositare acciaio inossidabile su quarzo. Lo scopo dell'utilizzo dell'acciaio è stato trovare i giusti parametri di sputtering e anche per analizzare l'uniformità del film. In questa prima fase sono stati testati diversi confinamenti magnetici che hanno permesso l'ottimazione della deposizione. Parallelamente è stata effettuata la deposizione di acciaio inossidabile su strisce di rame per realizzare il test di strippaggio come metodo per analizzare la presenza di zone non depositate. Nella seconda fase ci si è concentrati sulla deposizione di film sottile di niobio su campioni di quarzo posti lungo il risuonatore al fine di migliorare le proprietà superconduttive, specificamente Rapporto Resistività Residuo (RRR) e la temperatura critica (T_c). Tuttavia, altri confinamenti magnetici sono stati testati per mantenere l'uniformità del rivestimento. È stata studiata l'influenza sulle proprietà superconduttive di due parametri principali del processo di sputtering: la potenza e la temperatura del substrato. Dopo aver impostato i parametri di deposizione, è stato utilizzato un confinamento magnetico definitivo per depositare la vera QWR in rame. Allo scopo di analizzare la performance della cavità ai campi RF è stata necessaria la progettazione, costruzione e installazione di un criostato. Infine, è stata trovata una nuova sorgente magnetica per depositare un film sottile di niobio uniformemente su cavità Quarto d'onda. Si è riscontrato che aumentando la temperatura del substrato e la potenza dello sputtering, la temperatura di transizione del film sottile di niobio era intorno 9,3K ed è stato ottenuto un RRR massimo di 61. Solo 30 min. sono stati necessari per depositare il film con una uniformità di 2 ± 1 micron lungo la cavità. I risultati del SEM hanno permesso di analizzare la microstruttura del film di niobio. Grani più grandi sono stati trovati sul conduttore interno, più vicino alla sorgente magnetron. Inoltre un criostato di prova è stato costruito con successo per misurare le prestazioni RF; il sistema può essere utile per effettuare misure a 4,2 e 1,8 K. La prima cavità QWR depositata con il magnetron sputtering è sotto le specifiche del CERN; è stato misurato un Q massimo di $2e^8$ e un campo accelerante di 2MV/m; tuttavia come primo risultato è estremamente importante per partire con la fase di ottimizzazione. Alcuni parametri saranno cambiati per migliorare le prestazioni e spingere la comunità SRF ad utilizzare la tecnica magnetron sputtering come un metodo economico per depositare cavità superconduttrici in tempi brevi.

ABSTRACT

In the framework of Eucard project, it has been carried out, in collaboration with CERN, the R&D on magnetron sputtering deposition on the HIE-ISOLDE cavity geometry, as an alternative method to deposit niobium thin films. In this research a new magnetron configuration source was tested at the National Institute of Nuclear Physics (INFN-LNL), in order to deposit a uniform niobium thin film onto copper superconducting Quarter Wave Resonator cavities. The methodology was divided in three. A first part, in which a test dummy cavity and a test cathode were used in order to deposit stainless steel onto copper quartz. The purpose of the use of steel has been finding the right parameters of sputtering and also to analyze the uniformity of the film. In this first phase it have been tested several magnetic confinements, which allowed the optimization of the deposition. In parallel it was performed the deposition of stainless steel onto copper strips, to realize the stripping test as a method to analyze the uniformity of the film. The second part was focused on the deposition of niobium thin film onto quartz samples placed along the resonator to improve the superconducting properties, specifically Residual Resistivity Ratio (RRR) and Critical Temperature (T_c); nevertheless other magnetic confinements were tested to maintain the uniformity of the coating. It was studied the influence on superconducting properties of two principal parameters of the sputtering process: the power and the substrate temperature. After setting the deposition parameters, a definitive magnetron confinement was used to deposit the real copper QWR. The RF performance was also measured after the design, construction and installation of a test cryostat. Finally, it was found the magnetic source to deposit a niobium thin film uniformly over QWR cavities. Increasing the substrate temperature and the sputtering power, the transition temperature of the niobium thin film was around 9,3K and it was obtained a maximum RRR of 61. Only 30 min were necessary to deposit the film with a uniformity of 2±1 μm along the cavity. SEM results allowed to analyze the microstructure of the niobium film. Bigger grains were founds on the inner conductor closer to the magnetron source. In addition a test cryostat was successfully built in order to measure the RF performance; the system can be useful to perform measurements at 4.2 and 1.8 K. Respect to the RF performance the first Nb/Cu cavity is under the specifications of CERN with a maximum Q value of $2e^8$ and an accelerating field of 2MV/m; however this first result is extremely important to start with the optimization phase. Some parameters will be changed in order to improve the performance and push the SRF community to use the magnetron sputtering technique as an economical method to deposit superconducting cavities in short times.

To my parents Daniel and Gislaine
and my Sister Eliane.
They have given me the motivation,
support and the force
necessary to
reach
each one of my goals.

Chapter 1.

INTRODUCTION

Superconducting Quarter Wave Resonators (QWRs) take an important place in the construction of several particle accelerators, and for this reason it has been for years a relevant research topic for the superconducting cavity community.

Many research institutions have studied the sputtering technology applied to complex substrates. The development of the deposition of Niobium onto copper cavities started at CERN from 1980 [1], as a method to replace bulk cavities. Then, at Legnaro National Laboratories (LNL), since 1987 it has been studied the bias diode sputtering in order to deposit Niobium onto copper QWRs for the construction of ALPI accelerator, obtaining positives results: good film uniformity and good performance but lower deposition rates in comparison with other techniques such as magnetron sputtering technique [2].

Nowadays in order to increase the beam energy, QWR cavities with accelerating field of at least 6MV/m for 10W maximum power dissipation and at least $5e^8$ of Q value, are required to be placed in the HIE-ISOLDE linac at CERN. This requirements were reached by CERN with the bias diode with long times of deposition [3]. For this reason, it is necessary the parallel R&D on going at CERN and LNL in the quest for higher performances.

The magnetron sputtering is a deposition technique widely used in the thin film industry, however with this method the uniformity of the film is generally not easy to control; it is a real challenge to use this technique for the coating of really complex form as having QWRs substrates.

The aim of this investigation is to find a magnetron configuration source to deposit the cavities uniformly, in short times (40min and not 40 hours) and low cost, having a good superconducting performance.

In order to carry out the first stage of this study, it was necessary to develop and realize these topics: the construction of a vacuum system with a cathode adapted to the shape of the QWR, the

construction of a stainless steel test cavity and also a stainless steel test cathode in order to study the magnetic field configuration, the study of magnetic field lines using the 2D Finite Element Method (FEM) software, the construction of the magnetron body and the deposition of stainless steel thin films onto quartz samples to study the uniformity along the cavity.

The second stage of this investigation was focused on the setting of the process parameters and the upgrade of the magnetic field configuration. In this part, a double wall niobium cathode was built to carry out the niobium depositions onto quartz samples. The Process parameters were studied rigorously to improve the superconducting properties of the film such as residual resistivity ratio and the critical temperature.

The next part of the research was focused on the design and construction of the 1,8/4,2K QWR cryostat and the RF transmission line, in order to study the performance of the cavity at RF fields. Last part of this study was the deposition of the real copper QWR cavity of ISOLDE type and the measurement of the RF performance.

The results of this work has been patented by INFN with the Italian application ….*

- * Italian application number will be reported in the final version of this thesis

PHD. Thesis

Construction of an innovative cylindrical magnetron sputtering for ISOLDE SPC Nb/Cu QWRs cavities

- **HIE-ISOLDE Particle accelerator**
  - General particle accelerator
  - ISOLDE proyect
- **Bases of superconductivity**
- **RF Superconductive cavities**
  - RF superconductive cavities
  - Nb cavities
  - Nb/Cu cavities
  - QWRs cavities
- **Niobium properties**
- **Deposition of the film**
  - Sputtering
  - Diode Sputtering
  - Magnetron sputtering
- **Vacuum system**
  - Vacumm chamber
  - schemes
  - cathode
  - Magnetron
- **Experimental method**
  - Materials and equipments
  - Experimental procedure
  - Magnetron simulations
  - Chemical treatments
  - Measurements
    - Thickness
    - RRR and Tc
    - Q value and Eacc
- **The RF system**
- **Film caracterization**
- **Results and analysis**
- **Conclusions**

Chapter 2.

ION BEAM ACCELERATOR FACILITIES

The normal conductive particle accelerators have been first conceived in the 1930s, in order to supply charged particles to be investigated in many topics of particle physics. An accelerator can increase and speed up a beam applying electric fields, and also can focus the particles with magnetic fields.

Generally, in order to accelerate the protons, an electric field strips hydrogen nuclei of their electrons, then the electric fields switch from positive to negative at a specific frequency, pulling charged particles forwards along the accelerator. To ensure the particles in closely spaced bunches, the frequency is controlled.

In order to accelerate beams radio frequency (RF) cavities and magnets are needed. The RF cavities are metallic chambers spaced at intervals along the accelerator, they are shaped in order to resonate at determined frequencies, allowing radio waves that can interact with passing particle bunches. Each time the beam passes, the electric field is transferred to the particles. It is important that the particles cannot collide with the molecules of gases, because the beam is in an ultrahigh vacuum environment. Also various types of magnets are used in an accelerator. Dipole magnets, are used to bend the path of a beam or to focus it. Around the collision point are placed particle detectors in order to reveal the particles [4].

Depending on its shape and the path of the particles, accelerators can be classified as circular accelerator, where the particles travels around a loop, or linear accelerator if the beam of particles travels in a straight line, from one end to the other.

In 1964 Fairbank, Schwettman and Wilson at Standford Linear Accelerator Center (SLAC), start the acceleration of electrons with superconducting RF structures. In this experiment 80 keV electrons were accelerated by a lead-plated onto a 3 cell of copper, reaching an energy of 500 keV. Form this test it was demonstrated that a multicell accelerating structure could be operated at high accelerating gradients (3MeV/m) and Q's of $1e^8$. From this experiment it was also demonstrated that were no big difficulties with the cryogenics [5].

Nowadays a big number of accelerators has been used in order to reach higher energies and the type of particles depends of each experiment [4].

2.1. Isolde facility

The on-line isotope mass separator ISOLDE, is an accelerator used for the production of a big amount of radioactive ion beam that can be used or studied in the field of materials sciences, solid state physics, nuclear physics, atomic physics and life sciences. ISOLDE itself, is a multidisciplinary activity that contributes on accelerator development, silicon detectors and data processing, and simulations for beam-detector interactions.

ISOLDE is a source of low-energy beams of radioactive nuclides, with unstable neutrons. This accelerator can allows the study of many atomic nuclei, including the most exotic species.

This facility is located at the Proton-Syncotron Booster (PSB) at CERN, the European Organization for Nuclear Research. ISOLDE project has collaborators around the world and its principal members are Belgium, Denmark, Finland, France, Germany, Greece, India, Ireland, Norway, Romania, Spain, Sweden and United Kingdom [6].

At ISOLDE, a target can be irradiated with a proton beam from the PSB at 1,4 GeV and at 2μA of intensity to produce radioactive nuclides by spallation, fission or fragmentation. After the nuclear reactions the volatile nuclear products are extracted as a radioactive ion beam that could reach the highest intensities available all over the world. The accelerator has produced more than 600 isotopes with half-lives bellow to millisecond of around 70 elements (Z= 2 to 88). [7].

Figure 2.1 shows the ISOLDE facility at CERN.
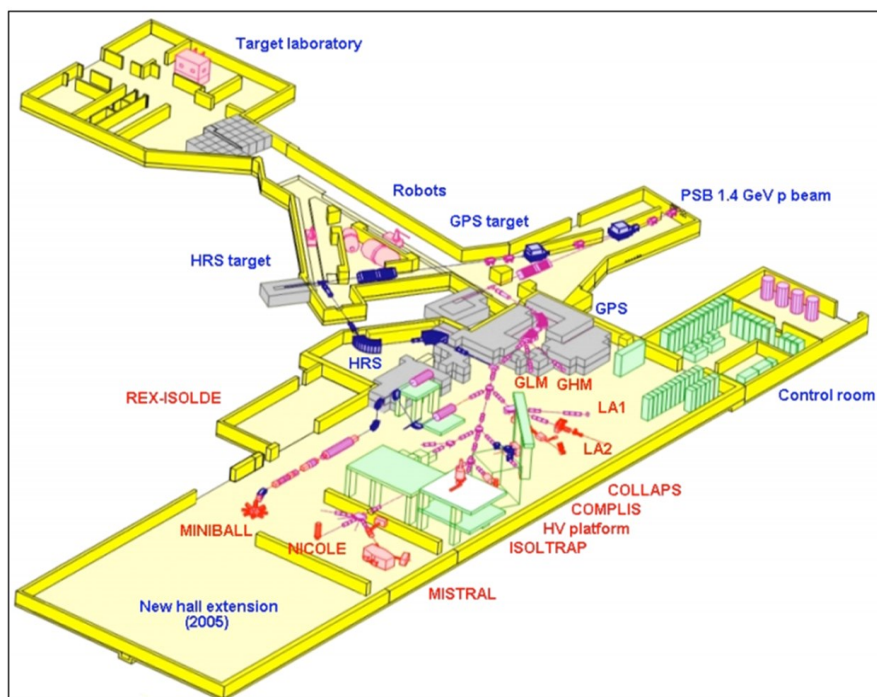
Figure 2.1 The ISOLDE facility [8]

2.2. REX-ISOLDE

The post accelerator REX-ISOLDE is a facility built to accelerate radioactive ion beam of higher energies such as light medium mass nuclei for reactions with energies up to 3,1 MeV/u. REX-ISOLDE has already accelerated several species of radioactive ions. This accelerator has been upgraded to provide the maxim um energy of 5.5MeV/u.

Nowadays the Radioactive Ion Beams (RIBs) are accelerated to high energies by a normal conducting linac, starting with the ion charge impulse. The REX-ISOLDE scheme is shown in Figure 2.2. The system is formed by a Penning trap (REXTRAP), a charge breeder (REXBIS) and an achromatic mass separator. The normal conducting accelerator has been designed with an accelerator voltage for a corresponding mass/charge ratio (A/q) of 4.5 and it delivers a final energy of 3 MeV/u for A/q < 3.5 and 2.8 for A/q < 4.5. The first accelerator stage is provided by a 101, 28 MHz Radio Frequency Quadrupole (RFQ) which takes the beam from 5 keV/u up to 300 keV/u. That beam is re-bunched into the 101,28 MHz drift tube (IH) structure to increase the energy to 1.2 MeV/u. To give

further acceleration to 2.2 MeV/u and finally a 202.58 MHz three split ring cavities are used, and in order to vary the energy from 2 to 3 MeV/u a 9 gap IH cavity is used [8].
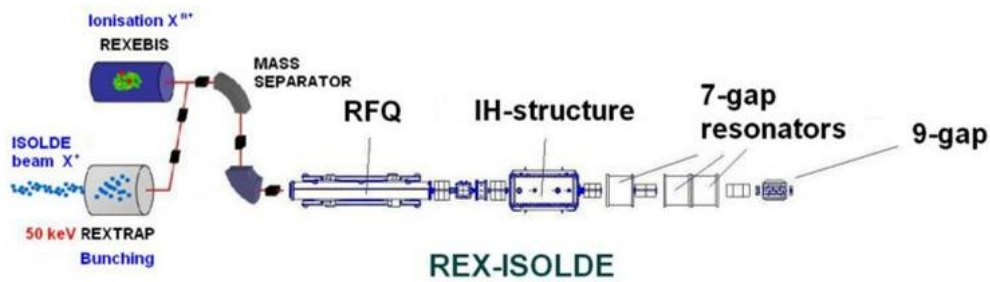
Figure 2.2 REX ISOLDE scheme [6].

2.3. HIE-ISOLDE

The HIE-ISOLDE project is part of the European nuclear physics strategy that has been created to expand the physics program in comparison with the REX-ISOLDE. Its operation can help to understand many scientific cases astrophysics and physics structure. The aim of the project is to increase the energy and the intensity of the delivered radioactive ion beam (RIB), filling the requests for a more energetic accelerated beam using superconducting (SC) linacs based on Quarter Wave Resonators (QWRs) cavities.

The development of this project started in 2008, and has been focused on the improvement of the high β cavity (β = 10.3%), for which it has been decided to apply the Nb sputtered onto Cu substrates technology. The SC linac has been designed to have an effective accelerating voltage of at least 39.6 MV, with an average synchronous phase φs of 20 deg. It is necessary to reach this voltage to achieve a final energy of at least 10MeV/u and a relation A/q= 4.5. Due to the steep variation of the ions velocity it is also necessary to have at least two cavity geometries, thereby the acceleration will be efficient throughout the whole energy range. 32 cavities are needed in order to have a full acceleration voltage and the geometry of these cavities can be of two types: low ß (β0 = 6.3%) and high ß (β0 = 10.3%). The "ß" cavities works with the fundamental beam frequency of 101, 28 MHz. The design was chosen to reach 6MV/m with a consumption of power of 7 W per low ß cavities and 10 W per high ß cavities [9].

Chapter 3.

BASES OF SUPERCONDUCTIVITY

3.1. General properties of superconductors

In 1911 H. Kamerling Onnes, studied the electrical resistance of mercury with the temperature observing that the resistance dropped sharply to zero at a temperature of 4,2K. The same properties were later discovered in some other metals. The phenomenon was named "superconductivity" and the corresponding metals were called "superconductors".

The temperature at which the resistance is close to zero is called critical temperature T_c and it is different in each material with superconductive properties. The highest critical temperature between pure metals is shown by niobium, T_c=9,25K; and the lowest has been found by tungsten, T_c=0,0154K. However these are both low temperatures and the temperature range is very wide, since the two extremes differ by about a factor of a thousand.

K. Onnes in 1914, has carried out subsequent investigations about superconductive properties. He has shown that superconductivity can be destroyed not only by increasing the temperature and also by applying a sufficiently strong magnetic field. The critical field (H_c) in which the superconductivity is destroyed decreases with the increment of temperature. The following formula describes empirically the dependence H_c (T).

$$Hc(T) = Hc(0)[1 - (\frac{T}{Tc})^2 \ ] \qquad (3.1)$$

Also the superconductivity can be destroyed by a strong electric current. If the superconductor is not too thin, the magnetic field produced by a critical current must be equal to zero at the surface of a superconductor.

Meissner and Ochsenfeld in 1933, have discovered another superconductive properties. If a metal is placed in a magnetic field smaller than H_c, then during the transition into the superconducting state the field is expelled from its interior; the true field or magnetic induction B that is the average microscopic field is zero in the superconductor. This effect is called Meissner effect. (See Figure 3.1).
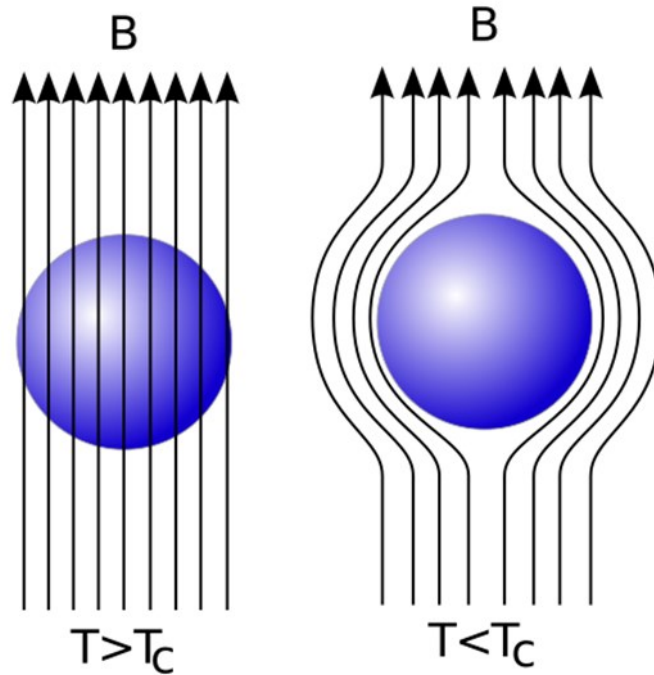
Figure 3.1.Meissner effect.

In more detailed investigations it has been shown that only in the bulk of a massive sample the magnetic field is equal to zero. In a thin layer which is called penetration depth (λ), the field decreases gradually from a given value to zero. The thickness of this layer is usually of the order of $1e^{-5}$ to $1e^{-6}$ cm. If a superconductor is placed in an external magnetic field, currents appears in the surface layer, producing a magnetic field on its own, that compensates the external field inside the superconductor [10].

There are two types of superconductors. The first one is the superconductor type I, mainly comprised of metal sans metalloids that have two characteristic properties: Zero DC electrical resistance and perfect diamagnetism when the material is cooled below a critical temperature T_o. Above T the material is not a very good conductor but is a normal metal. The second property is the perfect diamagnetism or also called Meissner effect, explained before [11].

The behavior of a superconductor type I is approximated by a parabola, and defines the limit of presence of superconductivity. It can be a sharp transition from the superconducting state to the normal one [12], as can be seen in Figure 3.2.
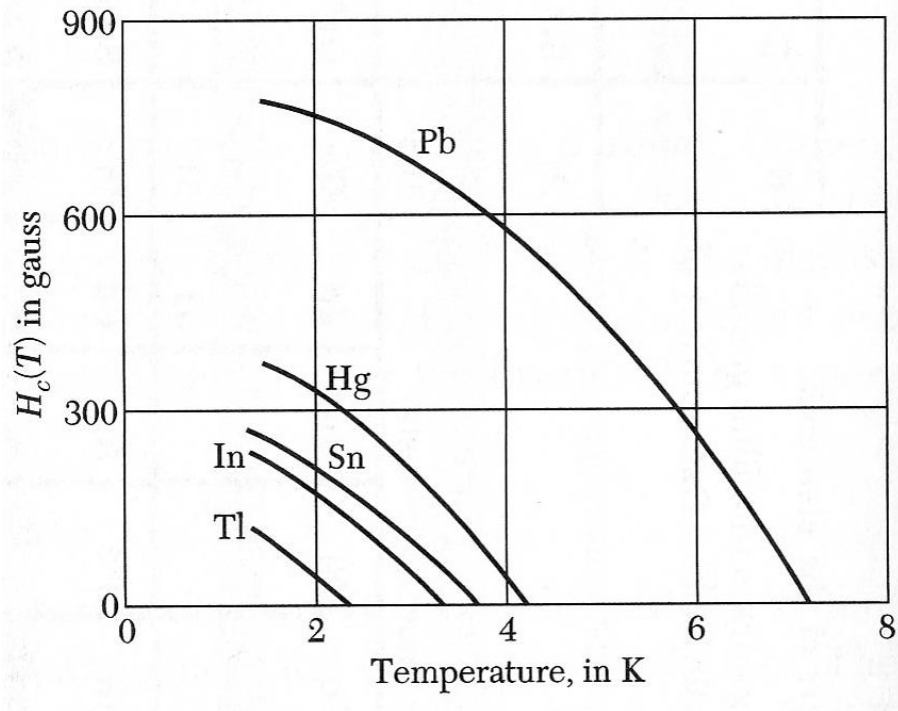
Figure 3.2. Critical field versus temperature for some superconducting elements [13].

The same transition can be seen drawing the magnetization versus the magnetic field.
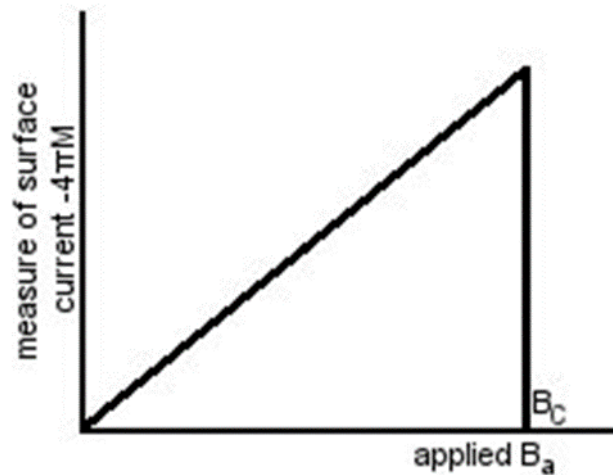
Figure 3.3. Magnetization versus magnetic field for superconductors type I.

The magnetization in the superconducting state is equal to $-H/4\pi$, while is zero in the normal state. The critical field of this type of superconductor is quite low (approximately less than 10^{-1} Tesla).

Second type superconductors are usually alloys and compounds. They have a high critical fields and high critical currents. The characteristic of this kind of superconductor is the magnetic

11

behavior. They have two critical fields H_{c1} (T), below which the material is totally superconducting and H_{c2}, that is the upper critical field over which the material is entirely normal conducting. (See Figure 3.4).
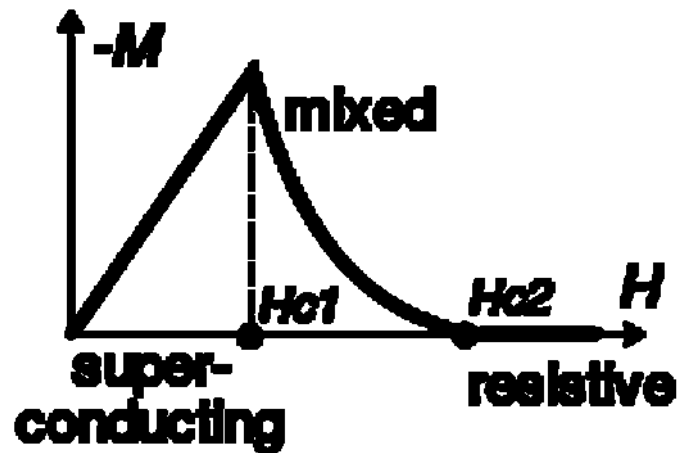
Figure 3.4. Critical magnetic field for superconductors type II.

In previous figure it can be seen the magnetization versus field for a second type superconductor, where shows an incomplete region of Meissner-Ochsenfeld effect.

Superconductors of second type are also perfect conductors of electricity (with zero DC resistance). It totally excludes the magnetic field in the Meissner state when the applied magnetic field is below the lower critical field, then when the applied field is between H_{c1} and H_{c2} the flux is partially excluded and above this field the material becomes normal conductor. The sample shows an incomplete Meissner state in which there is a partial penetration of magnetic flux in a complicated microscopic structure of thin normal conducting filaments surrounded by superconductive regions. Such kinds of filaments are called "vortexes" [12].

Fundamentally, a superconductor can be defined as a conductor that has a phase transition below a transition temperature T_c in which the conduction electrons form pairs called "Cooper pairs", which can carry electrical current without any resistance to the flow and which are also responsible for the perfect diamagnetism [11].

3.2 Coherence length in superconductors

A very successful microscopic theory was developed by Bardeen, Cooper and Schrieffer which is called BCS- theory [14] for classical superconductors like lead or tin. They assumed that electrons begin to condense below T_c to pairs of electrons, the called Cooper pairs. The two electrons in a pair have opposite momentum and spin. They experience an attractive force mediated via quantized lattice vibrations called phonons. This bound state of the two electrons is energetically favorable. As the overall spin of these two paired electrons is zero, many of these pairs can co-exist coherently, just like other bosons. The coherence length describes the distance over which the electrons are correlated. It is given by:

$$\xi_0 = \frac{\hbar V_f}{\Delta} \tag{3.2}$$

Which Vf is the Fermi velocity that represents the velocity of the electrons close to the Fermi energy and $2 \cdot \Delta$ is the energy necessary to break up a Cooper pair. Typical values for the coherence length in niobium are around 39 nm. [15]

3.3. London Penetration depth

Respect type I superconductor, the magnetic field is not completely expelled, but penetrates inside the material over a small distance, otherwise the shielding current density would be infinitely large. The distance called "London penetration depth" is given by the characteristic length of the exponential decay of the magnetic field inside the superconductor.

$$H(x) = H(0)e^{\frac{-x}{\lambda l}} \tag{3.3}$$

The penetration depth value is:

$$\lambda l = \sqrt{\frac{m}{\mu_0 \, n_s c^2}} \tag{3.4}$$

Where e is the charge of an electron, m is the mass and ns the number of superconducting charge carriers per unit volume. A typical value for the penetration depth in niobium is 32 nm.

13

The theory did not allow for impurities in the material nor for a temperature dependence of the penetration depth. The scientists Gorter and Casimir introduced the two-fluid model where a coexistence of a normal- and superconducting fluid of charge carriers is postulated.

$$n_{c=} n_s + n_n \tag{3.5}$$

They suggested a temperature dependence of the superconducting charge carriers.

$$n_s(T) = n_s(0).\left(1 - \left(\frac{T}{T_c}\right)^4\right) \tag{3.6}$$

Combining the last two equations, the penetration depth shows the following temperature dependence:

$$\lambda_l(T) = \lambda_0 \left(1 - \left(\frac{T}{T_c}\right)^4\right)^{\frac{-1}{2}} \tag{3.7}$$

The Ginzburg-Landau parameter is defined as:

$$k = \frac{\lambda_l}{\xi_0} \tag{3.8}$$

κ is a parameter that allows to identify the two types of superconductors:

$$k < \frac{1}{\sqrt{2}} \quad superconductor\ type\ I \tag{3.9}$$

$$\tag{3.10}$$

$$K > \frac{1}{\sqrt{2}} \quad superconductor\ type\ II$$

14

Niobium has $\kappa \approx 1$ and is a weak type-II superconductor. The role of impurities was studied by Pippard, [16] the study was based on the evidence that the penetration depth depends on the mean free path of the electrons in the material. The dependence of ξ on the mean free path is the following.

$$\frac{1}{\xi} = \frac{1}{\xi_0} + \frac{1}{\ell} \qquad (3.11)$$

He introduced an effective penetration depth:

$$\lambda_{eff} = \lambda_l \cdot (\frac{\xi_0}{\xi})^{\frac{1}{2}} \qquad (3.12)$$

Here again ξ_0 is the characteristic coherence length of the superconductor. This relation reflects that the superconducting penetration depth increases with a reduction of the mean free path [17]. For pure ("clean") superconductor ($\ell \to \infty$) one has $\xi = \xi_0$. In the limit of very impure ("dirty") superconductors where $` \ell \ll \xi_0$, the relation becomes instead

$$\xi = \ell \qquad (3.13)$$

The mean free path in the niobium is strongly influenced by interstitial impurities like oxygen, nitrogen and carbon.

3.4. The skin effect in normal conducting case

If a RF electromagnetic field is oscillating inside the cavity, only the electrons of a thin layer called skin depth on the resonator walls, are interacting with the radiofrequency field and the loss are confined in such a layer [18].

There is an analogy between the shielding mechanism of a microwave field in a normal conductor and the shielding of a static magnetic field in a superconductor. If a microwave of frequency is incident on a metal surface, the field decays over a distance (skin depth). If the frequency is much lower than plasma frequency, the mean free path of the electrons is smaller than the penetration depth.

$$\delta = \sqrt{\frac{2}{\sigma \mu_0 \omega}} \qquad (3.14)$$

Where σ is the conductivity of the metal. In this regime, the skin effect is shown. The surface resistance can be calculated.

$$R_{surf} = \frac{1}{\sigma\delta} -$$

(3.15)

In this case the resistance decrease at cryogenic temperatures because σ increase when T→0. Regarding pure metals, at low temperatures ℓ may be larger than δ which leads to the anomalous skin effect. The resistance when ℓ →∞ is represented for the following equation:

$$R_{surf} = [\sqrt{3\pi} \left(\frac{\mu_0}{4\pi}\right)^2]^{\frac{1}{3}} \omega^{\frac{2}{3}}(\frac{l}{\sigma})^{\frac{1}{3}}$$

(3.16)

3.5 Superconducting cavities
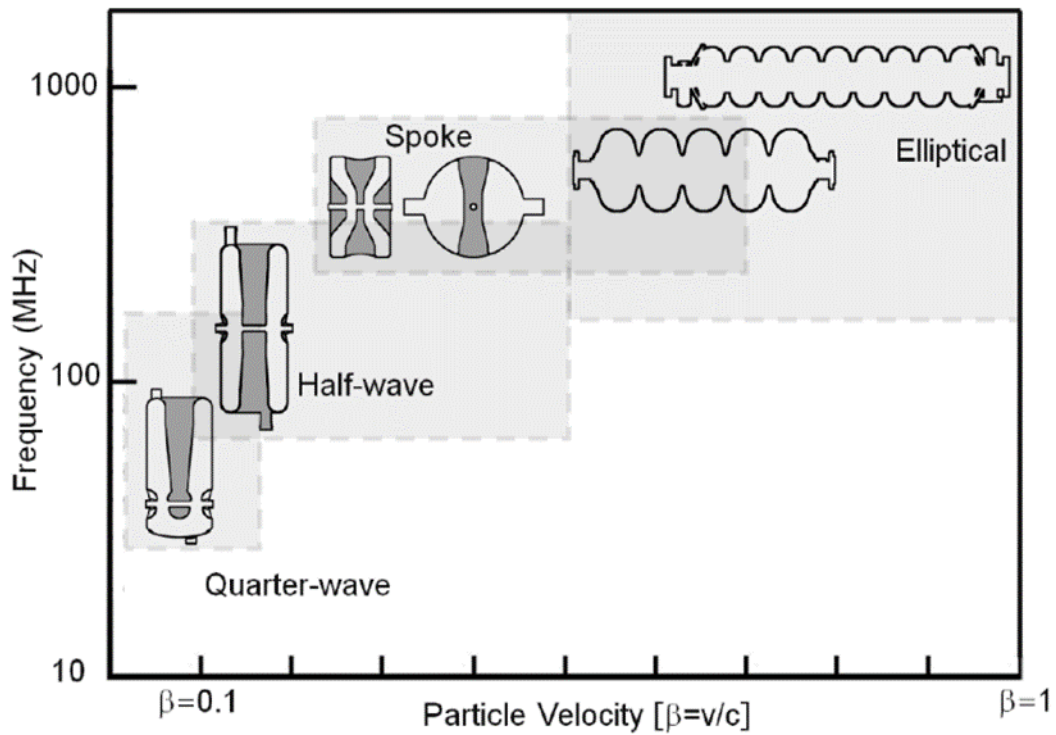
Figure 3.5 Classification of accelerating structures. [13]

The efficiency with which a particle beam can be accelerated in a radiofrequency cavity depends on the surface resistance. The smaller the resistance i.e. the lower the power dissipated in the walls, the higher the radiofrequency power available for the particle beam. This is the fundamental

16

advantage of superconducting cavities as their surface resistance is much lower and outweighs the power needed to cool the cavities to liquid helium temperatures. Figure 3.5 shown a classification of accelerating structures taking into account the resonant frequency and the velocity of the particles. This study will be focused on the low beta QWR cavities.

An important component of the particle accelerators the device that provides energy to the charged particles. This device is an electromagnetic cavity resonating at microwave frequency [19]. A resonant cavity is the high-frequency analog of a LCR resonant circuit and the RF power at resonance builds up high electric fields used to accelerate the particles. The energy is stored in the electric and magnetic fields.

At low frequencies, the parallel- connected capacitor and inductance will resonate at a frequency [12].

In a RF cavity in order to accelerate particles, an RF power generator supplies an electromagnetic field. The RF cavity is molded to a specific size and shape so that electromagnetic waves become resonant and it can be accumulate inside the cavity. Charged particles passing through the cavity feel the overall force and direction of the resulting electromagnetic field, which transfers energy to push them forwards along the accelerator.

The field in an RF cavity is made to oscillate (switch direction) at a given frequency, so timing the arrival of particles is important [4].

The energy gained per unit length is an important parameter of accelerating cavities. This is conveniently derived from the accelerating voltage of a particle with charge e while traversing the cavity:

$$V_{acc} = |\frac{1}{e} x\ u| \tag{3.17}$$

In which u is the energy gained during the transit

For particles travelling close to the velocity of light c on the symmetry axis in z-direction
($\rho = 0$) and an accelerating mode with eigen frequency ω this gives [15].

$$V_{acc} = |\int_0^d E_Z \ (dz)e^{iwz/c}dz| \tag{3.18}$$

The accelerating field is

$$E_{acc} = \frac{V_{acc}}{d} \tag{3.19}$$

An alternating current is flowing in the cavity walls to sustain the radiofrequency fields in the cavity. This current dissipates power in the wall as it experiences a surface resistance. One can look at the power P_{diss} that is dissipated in the cavity to define the global surface resistance $R_{surf.}$.

$$P_{diss=} \oint_A \frac{1}{2} R_{surf} H^2{}_{surf} dA \tag{3.20}$$

If R_{surf} is independent of the position

$$= \frac{1}{2} R_{surf} \oint_A H^2_{surf} \ dA \tag{3.21}$$

H_{surf} represents the magnetic field amplitude on the surface. Usually, one measures the quality factor Q0 [15].

$$Q_0 = \frac{\omega \ W}{P_{diss}} : \tag{3.22}$$

Where

$$W = \frac{1}{2} \mu_0 \int_V H^2 \ dV \tag{3.23}$$

is the energy stored in the electromagnetic field in the cavity. R_{surf} is an integral surface resistance for the cavity. The surface resistance and the quality factor are related via the geometrical constant G which depends only on the geometry of a cavity and field distribution of the excited mode, but not on the resistivity of the material [15]:

18

$$\omega = \frac{G \oint_A H^2 \, dA}{\mu_0 \int_V H^2 \, dV} \tag{3.24}$$

$$Q_0 = \frac{\omega \mu_0 \oint_V H^2 \, dV}{R_{surF} \oint_A H^2 \, dA} = \frac{G}{R_{surf}} \tag{3.25}$$

and

$$G = \frac{\omega \, \mu_0 \int_V H^2 \, dV}{\oint_A H^2 \, dA} \tag{3.26}$$

3.6. QWR cavities

The Quarter Wave resonator is a basic resonant structure that consist of a length of transmission line shorted at one end and "open" at the other end, the length is nearly a quarter of the free space wavelength of the lowest resonator frequency . The high impedance at the open extreme can be used to accelerate the particles, building up high voltages needed for particle acceleration. The QWR was created in 1981 for heavy ion acceleration [20].

The main advantages of the QWR are the followings:
1. A broad curve of the transit time factor.
2. A structure which is simple to manufacture and balance electrically.
3. High frequency of the lowest mechanical mode.
4. Low peak surface field values.
5. Efficient cooling of the inner conductor.
6. Elimination of the end plates which are necessary in split loop and spiral resonators and which can be a source of frequency drifts and lossy joints.

Mostly, QWRs are used in the acceleration of low velocity ions. These types of cavities can been made using different materials (lead-plated copper, niobium explosively bonded to copper, pure niobium metal and niobium sputtered on cooper).
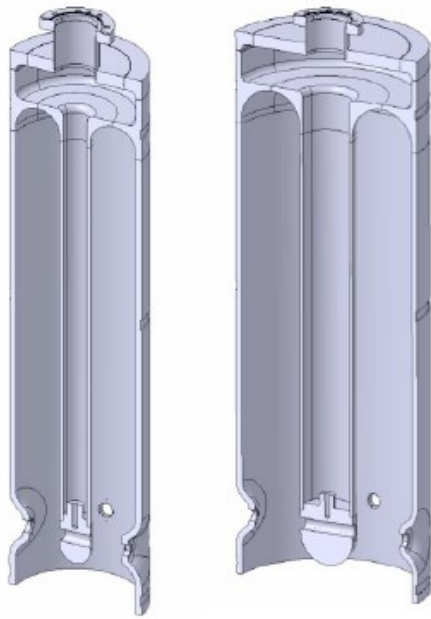
Cavity	Low β	high β
No. of Cells	2	2
f (MHz)	101.28	101.28
β_0 (%)	6.3	10.3
Design gradient E_{acc} (MV/m)	6	6
Active length (mm)	195	300
Inner conductor diameter (mm)	50	90
Mechanical length (mm)	215	320
Gap length (mm)	50	85
Beam aperture diameter (mm)	20	20
U/E_{acc}^2 (mJ/(MV/m)^2)	73	207
E_{pk}/E_{acc}	5.4	5.6
H_{pk}/E_{acc} (Oe/MV/m)	80	100.7
R_{sh}/Q (Ω)	564	548
$\Gamma = R_s \cdot Q_0$ (Ω)	23	30.6
Q_0 for 6MV/m at 7W	$3.2 \cdot 10^8$	$5 \cdot 10^8$
TTF max	0.85	0.9
No. of cavities	12	20

Figure 3.6. Low and high ß cavities [25].

3.7 Niobium properties

The English Hatchett C., who at the time named this new element columbium discovered niobium in 1801. Niobium is the 41st element of the periodic table and it is a transition metal of V group and fifth period. The content of niobium in the Earth's crust is 1e[-3]. Niobium is widely used in metallurgy, jewels, for nuclear power stations and in the space sciences. Recent research has focused on superconductive properties of niobium and niobium alloys. In the family of superconducting elements, it has the highest critical temperature.

The Nb is a lustrous, grey, ductile, paramagnetic metal, although it has an atypical configuration in its outermost electron shells compared to the rest of the members. Its crystal system is based on body centered cubic (BCC) and it is considered a refractory metal due to its very high melting point. The following table presents some properties of niobium [21].

Table 1 Niobium properties

Atomic number	41
Atomic mass [g/mol]	92.91
Melting point [°C]	2468
Boiling point [°C]	4927
Atomic volume [m3]	$1,8e^{-29}$
Vapor pressure at 1800 °C [Pa]	$7 e^{-6}$
Density at 20 °C [g/cm3]	8.56
Lattice structure	body-centered-cubic
Lattice constant [Å]	3,030
Hardness at 20 °C cold-worked [HV10]	110 – 180
Hardness at 20 °C recrystallized HV10]	60 – 110
Young's modulus at 20 °C [GPa]	104
Poisson's ratio	0.35
Linear coefficient of thermal expansion at 20 °C [m/(m•K)]	$7,1 e^{-6}$
Thermal conductivity at 20 °C [W/(m•K)]	52
Electrical conductivity at 20 °C [1/(Ω•m)]	$7 e^{-6}$
Specific electrical resistance at 20 °C [(Ω•mm2)/m]	0,14
Superconductivity (transition temperature) [K]	9.26
Specific Heat 20°C	0,27

3.8. Nb and superconducting cavities

Nb as pure element has the highest critical temperature (9,25K in its bulk form) and also the highest thermodynamic critical field ($1,6e^5$ A/m). The mechanical properties of Nb are good enough to machine the cavities that require a precise handling. In superconductive resonator it is mandatory to have high values of Quality factor (Q), as high as possible. In order to have a Q value of $1e^{10}$ at 1,8K the surface resistance should be at 4,2 K around 900 nΩ and few nΩ at 1,7 K for the TESLA type cavities; there is a strong dependence of the surface resistance with the temperature. The residual

surface resistance of Nb sheets can be from few nΩ to several hundreds of nΩ and it is related to the surface preparation and purity.

However a high quality niobium must be used due to the presence of high accelerating fields that can decrease the thermal conductivity and break the superconducting state. For this reason it is useful to develop purification techniques and electro- polishing methods that minimize the presence of defects on the surface [22].

The performance of a superconducting cavity is limited by a quench or breakdown of superconductivity. The thermal breakdown (quench) is that heating can originates at submillimeter-size regions of high RF losses, called defects. If the temperature of a good superconductor outside the defect exceeds the superconducting transition temperature (T_c), the RF losses increase considerably, as a growing region becomes normal conducting, leading to rapid loss of stored energy called "quench." An obvious approach to avoid quench is to prepare the niobium material with great care to keep it free from defects [23].

One method of insurance against thermal breakdown is to raise the thermal conductivity of niobium by raising the Residual Resistivity Ratio. With high thermal conductivity metal, any large defect can tolerate more power before driving the neighboring superconductor into the normal state. Normal material quality control and treatment procedures should avoid such large defects. However with 10000 cavities there is the possibility of encountering a few [23].

3.9 Residual Resistivity Ratio (RRR)

An accurate measurement of the Residual Resistivity Ratio (RRR) of niobium samples is important in the construction of superconducting radio frequency (RF) cavities [24]. The purity of a metal can be characterized by this parameter, which is defined as the ratio between the electrical resistivity at 300 K and the resistivity at 4,2 K which are the resistivity of Nb at room and liquid helium temperatures.

$$RRR = \frac{\rho(300K)}{\rho(4,2K)} \tag{3.27}$$

In pure metals having a lattice without structural defects at temperatures close to 0 K, resistivity tends to be zero [25] as is shown in figure 3.7.
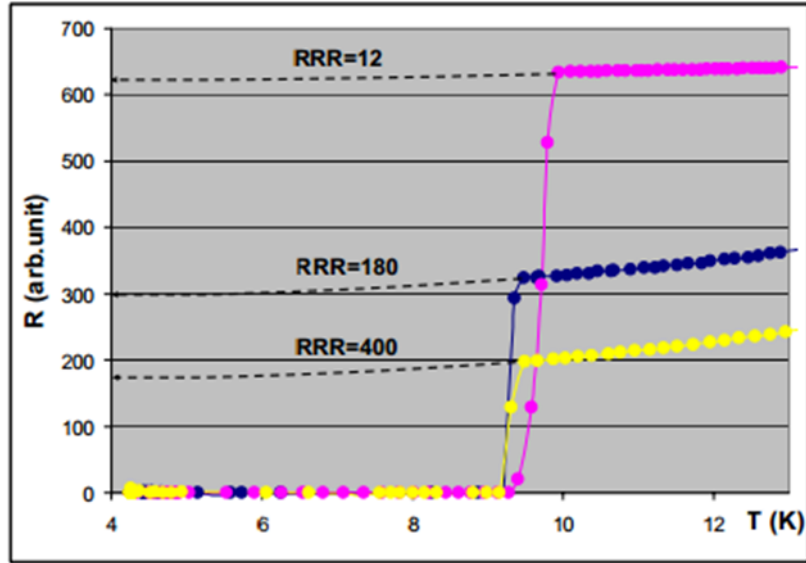
Figure 3.7 Typical R (T) curves for Nb samples of different purity [22].

At a certain temperature, the resistivity ρ (T) is proportional to the sum of resistivities from crystalline state ρ_{cryst} (grain boundaries density, dislocations, etc.), impurities ρ_{imp}, surface ρ_{surf} and phonon interaction which is a function of temperature ρ_{ph} (T). For DC

$$\rho(T) = \rho cryst + \rho imp + \rho surf + \rho_{ph}(T) \qquad (3.28)$$

Where the residual resistivity contains

$$\rho_{res} = \rho cryst + \rho imp + \rho surf \qquad (3.29)$$

If the resistance measurements are performed on sufficiently large, well recrystallized samples, and at very low temperatures, then the terms ρ_{cryst}, ρ_{surf} and ρ_{ph} (T) are negligible, and the residual resistivity depends mainly on the impurity content of the sample [26].

The most popular is the data of [9] determined because of resistance measurements on niobium voluntarily contaminated by impurities [25].

Superconductors are free from energy dissipation for direct current (DC) applications, but it is not the same for alternating current (AC) and particularly not in microwave fields, where current

changes its sign after every $1e^{-9}$ seconds. In this regime, the high frequency magnetic field penetrates a thin surface layer and also induces oscillation of the electrons, which are not bound in Cooper pairs. The power dissipation caused by motion of unpaired electrons can be characterized by a surface resistance R_{surf}. Surface resistance of super conductor is composed of two terms as given below

$$R_{surf} = R_{BCS}(T) + R_{Res} \tag{3.30}$$

Where R_{BCS} is the BCS surface resistance which is expressed as

$$R_{BCS} = \frac{A}{T} f^2 e^{\frac{-\Delta}{KT}} \tag{3.31}$$

That can be written also as

$$R_{BCS} = \frac{A}{T} e^{\frac{-S\,Tc}{2T}} \tag{3.32}$$

$2\Delta = SKT_c$. S is the strong coupling factor, generally equal to 3, 56, but for niobium it was found around 3, 8±0,2 and A, a constant which depends on material parameters of superconductors such as penetration depth, coherence length, the Fermi velocity and mean free path. The energy required to break cooper pair is 2Δ.

It is experimentally observed that below a certain temperature, surface resistance is higher than the BCS prediction. The additional temperature independent term R_{RES} is called as residual surface resistance. The term residual indicates that the causes of losses are often not so clear, because both physical phenomena and accidental mechanism like dust, chemical residuals or surface defects on the cavity walls contribute to the residual [18].

3.10. Basics of Q drops

Manufacturing of radiofrequency cavities by deposition of superconducting thin films is an extremely important topic because of the necessity to reduce costs. For this reason superconducting cavities manufactured by thin film coating of Nb or Nb compounds (Nb3Sn, NbN, NbTiN and other materials) could be an attractive alternative to bulk niobium cavities in terms of lower cost and higher limits for both, critical temperature and superheating magnetic field. But the main disadvantage of

thin film cavities is the continuous decrease of the quality factor Q_0 versus accelerating field $E_{acc.}$. Next figure shows a typical Q_0 versus E_{acc} for niobium thin films onto copper cavities.
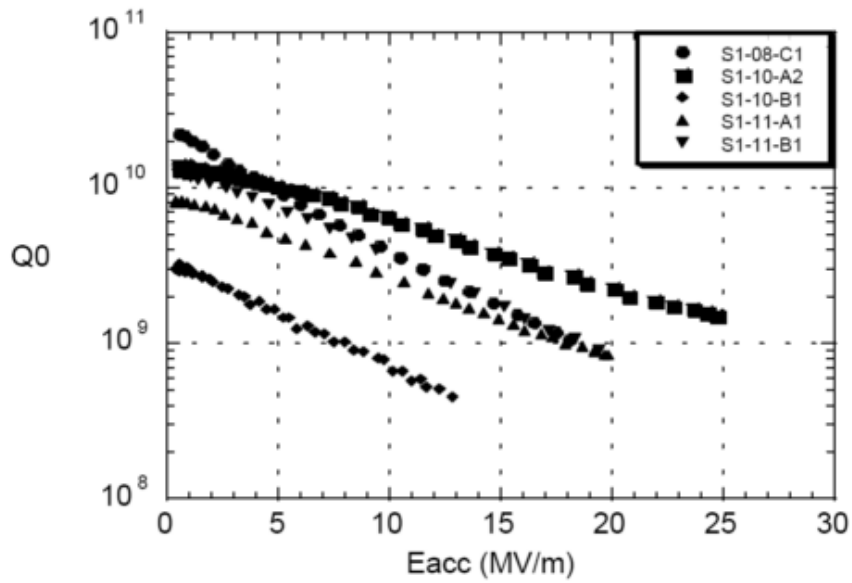
Figure 3.8.Example of typical Q vs Eacc at 1,7 K of niobium coating on copper cavities of 1,5GHz [27].

However it is possible to get very good performance by the using of the niobium film technology. The use of film cavities for accelerators operating at 1.7 K was not contemplated because of the supposedly "intrinsic" limitations of films, which could prevent operation at high RF amplitudes with high Q values. Nevertheless, such limitations are experimentally not confirmed. Next figure shows the Q value as a function of the accelerating RF field for some of the best performing cavities studied at CERN in which Q values of $1e^{10}$ at 15 MV/m and $4e^9$ at 20 MV/m were obtained. The operating range can probably be further extended by improving the manufacturing process.
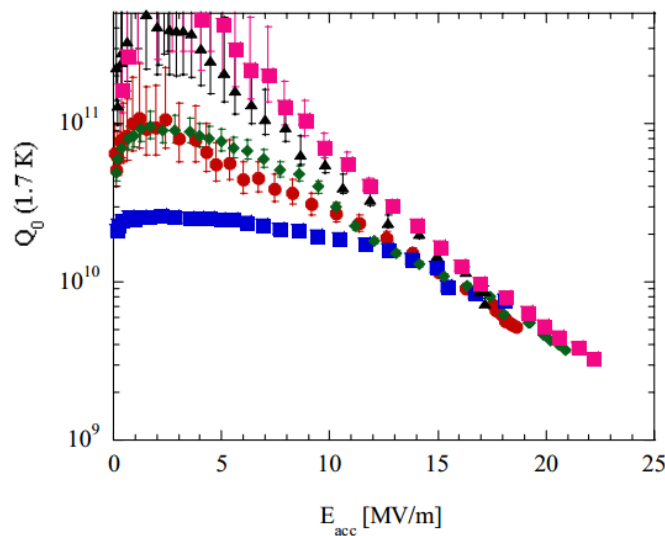
Figure 3.9 The Q factor versus accelerating field for the best Nb-Sputtered Cu 1,5 GHz cavity fabricated at CERN [28]

In order to understand the Q-drop in thin films, it will be necessary to discuss the Q-drop in niobium bulk cavities.

3.11 Bulk cavity Q-drop

Some years ago, the Q drop was considered as a typical feature of BCP cavities since the KEK group could show that the electro-polishing process did not give significant problems. The Q-drop was named by K. Saito the "European headache". Few years after, the CEA/ Saclay group discovered that an in-situ bake at moderate temperatures between 90-120°C partially alleviated the Q-drop problem. The same was shown later in the study of electro-polished cavities, which had also shown Q-drop at DESY, a fact that created confusion as to the claimed superiority of electro-polishing. Later, it was understood that a moderate temperature baking was part of the Japanese electro-polishing procedure. It has to be noted, however, that the baking effect is generally more pronounced in electro-polished cavities, i.e. often a small residual Q-drop remains in the chemically polished (BCP) cavities after baking.

But it is necessary to note that Q-drop is not at all unusual. This problem can have many different origins and explanations. A material with a low RRR, for instance, shows higher resistance at low field, stronger Q-slope and earlier onset of Q-drop. The lower the RRR, the stronger the above features. However, there are exceptions to this rule. One example for this was observed in 9.56 GHz cavity that reached a 150 mT peak magnetic field with very little Q-drop, made from a material of RRR ~50. Cavities made from deep drawn polycrystalline sheet material, which haven't undergone the initial 100 micron etching to remove the "damage layer", also show strong Q-slope and early onset of Q-drop [49].

Recently Visentin [51] showed that the Q-drop can also be avoided with a heat treatment at 145°C for 3 hours, instead of the established 48 hours at 120°C. It was a significant technological advancement, which allowed shortening of the cavity processing time. Since both, these baking conditions result in the same oxygen profile in the Nb surface, as calculated from a simple diffusion model, this finding also suggests a possible role of oxygen in the Q-drop phenomenon. The role of oxygen was already suspected when measurements indicated that the reduction in BCS resistance that

26

accompanies the baking disappears after removing of ~100 nm of material from the surface. This is consistent with the thermal diffusion length of oxygen at the baking temperature and duration.

The baking effect on the BCS resistance remains after long-term exposure to air and high pressure water rinsing. The baking effect on the BCS resistance saturates after a certain bake-out time. When removing surface layers in a baked cavity in small steps, the BCS resistance slowly rises again. After removal of 300 nm from the surface the BCS resistance of before baking is restored. But recent studies showed that Q-drop re-appears after removal of ~10 nm from the Nb surface through anodization in a baked cavity. This could indicate that the origin of the Q-drop effect is located in an even thinner surface layer. Possibly this could also hint at the change of BCS resistance with baking being just a secondary benefit of the baking, with both effects, BCS resistance change and Q-drop, actually having different origins [51] [53].

Respect to the thin films, Q-slopes in the bulk case have different origins. In Figure 3.10 it is possible to note a softer Q-slope for the bulk cavity at medium accelerating fields and a steeper one above 25 MV/m. Performances of E_{acc} are in both cases limited by the RF power supply available.
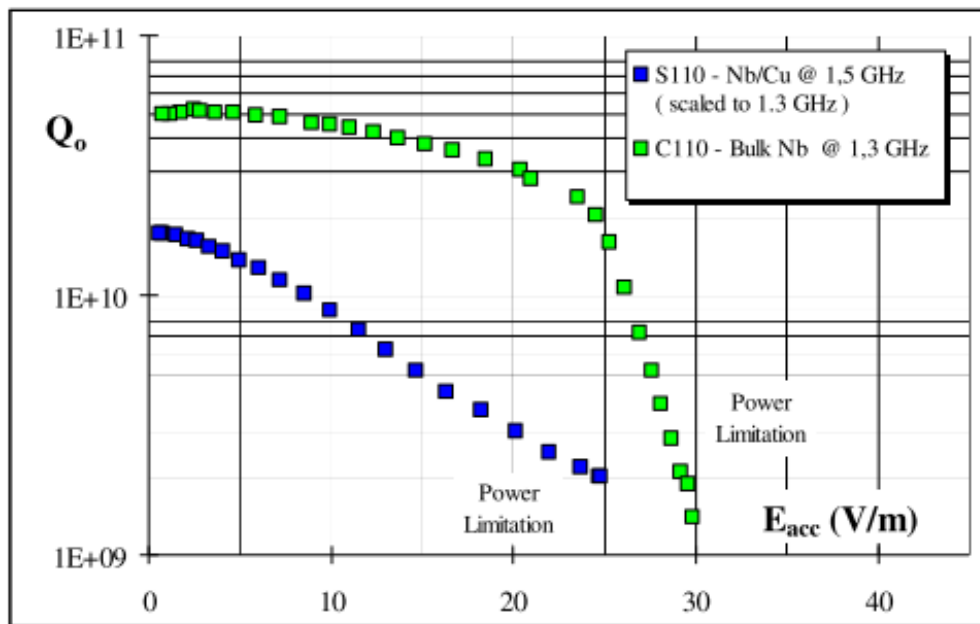
Figure 3.10. Comparison of Q drops between thin films and Nb bulk cavities

The physical reason of the high field Q-slope removal by baking is a challenging issue and many studies have been carried out in order to find an explanation. In parallel, several theories have

been pushed forward to explain the Q-slope existence. In order to understand the Q-slope, it is necessary to review the latest results with the secret hope to clear up by the way the thin film issue.

For a bulk cavity, it is necessary to consider three different Q-slopes in the Q_0 (Eacc) curve: at low (LF), medium (MF) and high fields (HF). This slopes can be seen in the next figure.
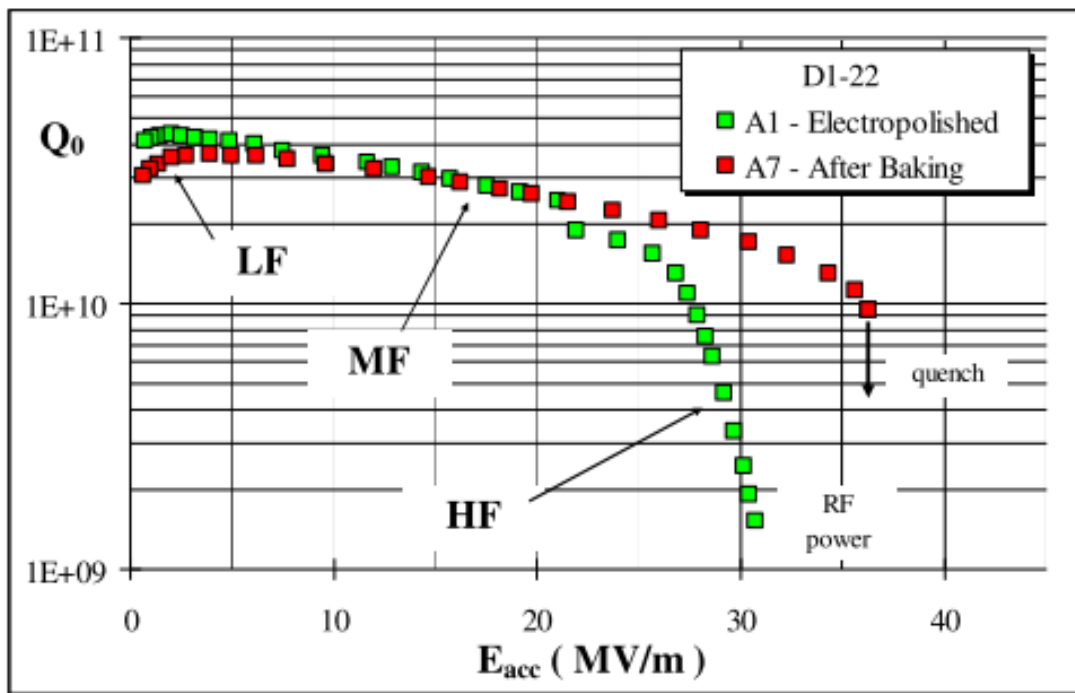
Figure 3.11 Low, medium and high field Q-slopes

3.11.1. Low Field Q-slope

Halbritter [54] analyzed the topic, saying that the Q-slope at low field is due to the presence of NbO_x clusters in niobium, located at the oxide-metal interface, providing localized states inside the Nb energy gap, therefore increasing the surface resistance. This explanation could help to understand some experimental observations:

• After cavity baking, the low field Q-slope enhancement could be caused by additional clusters due to the interstitial oxygen diffusion.

• After hydrofluoric rinse of the baked cavity, low field Q-slope is restored as before baking. Due to hydrofluoric acid just removes the niobium oxide and that a new oxide layer is later rebuilt at the surface, the low field Q-slope origin is necessarily located in the oxide layer or at the oxide-metal interface as NbO_x clusters.

By the other hand V. Palmieri [34], says that the low field increase of the Q-factor can be mathematically described by the presence of an overlayer made of a poor superconductor. The low field increase of Q factor can be easily explained by simply calculating the surface impedance of the bilayer system (as is shown in next figure) made of the base superconductor SC2 coated by a thin layer of a poorer superconductor (SC1) of a given thickness *a*. The penetration depths of the two superconductors are respectively λ2 and λ1. It is necessary to note the experimental evidence that some of the most striking cases of Q-increase at low fields are found in cavities whose internal surface was either specially or contaminated by the presence of over layers.
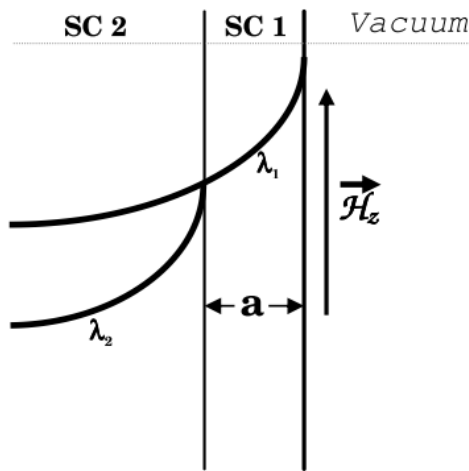
Figure 3.12. 2 Bilayer system made of the bulk niobium (SC 2) and of an over-layer of a superconductor (SC 1) with poorer superconducting properties.

In this model is presented a hypothesis in which being the over-layer a contaminated film, for low field intensities, its penetration depth λ1 can depend on the reduced magnetic field b = B/BC as in the following relation:

$$\lambda_1(B) \cong \lambda_1(0) + \alpha * b \tag{3.33}$$

By only this statement, it can be explained how, at low fields, the Q-factor can increase versus magnetic field. It is also possible to say that, the more λ1 increases with magnetic field, the more the "clean and high performance" SC2 is involved. After some calculations and algebra, the final relation for a bilayer Q factor is the following

$$Q_{TOT} = Q_1(0) * \left(1 - e^{\left(\frac{-a}{\lambda_1 - \alpha b}\right)}\right) + Q_2(0) * e^{-k2b} * e^{\left(\frac{-a}{\lambda_1 - \alpha b}\right)} \tag{3.34}$$

By previous equation, it can be noted that the role of SC1 is strongly dissipative and that the SC1 related Q-factor is increasing versus field. As far as the second term is concerned instead, by increasing the field, the penetration depth in SC1 becomes higher and the losses are more and more shifted into the SC2 that is a pure superconductor and has lower losses. This mechanism however shows a maximum. Strong fields saturate the SC2, giving rise to normal dissipative fields. The composition of the two terms presents also a maximum at even lower field value. The dependence of the maximum of Q_{Total} versus the thickness a of SC1 can also be observed. At a first sight, the Q rise versus field can appear as a benefit, but it is easy to observe that for lower values of a, the value of the Q_{Total} at the maximum also increases, proving that actually the presence of the over layer is a source of losses and it is not beneficial. However the presence of a Q-increase versus field can give useful information about the superficial contamination: the higher is the field at which the maximum occurs, the thicker is the over layer [34].

3.11.2. Medium Field Q-slope

Respect to the Q_0 (Eacc) evolution in the medium field range, a linear and a quadratic increases of the surface resistance R_S ($\propto 1/Q_0$) on the peak surface magnetic field B ($\propto$ Eacc) have theoretically been established .The linear dependence (Equation 7.1) is linked to hysteresis losses due to Josephson fluxons in weak links (oxidation of grain boundaries). As regards quadratic dependence (see Equation 7.2), it is produced by a surface heating due to the thermal impedances of Nb and Nb-He interface.

$$R_S = a + b\, B \tag{7.1}$$

$$R_S = R_0 \left(1 + \gamma \frac{B^2}{B_c^2}\right) \tag{7.2}$$

Here B_c is the thermodynamic critical field of niobium and R_0 is the surface resistance at small magnetic fields [54].

3.11.3. High fields Q-slope

An obstacle towards achieving reproducibly high accelerating gradients is represented by anomalous losses, when the peak surface magnetic field is above about 90 mT. Those losses can cause a sharp degradation of the cavity quality factor in the high field region, effect known as "Q drop", a precipitous decrease in the cavity quality factor when exceeding 20-30 MV/m.

A refinement in the expression of the γ parameter of the precedent thermal model (equation 7.2) takes into account the non linear correction due the RF pair. This non-linear thermal model could explain both the medium field and the high field Q-drops. But the predicted Q-slopes cannot fit experimental ones at high fields.

While low field and medium field models successfully explain the Q slope, the cause of this sudden increase in surface resistance at high fields is yet unknown. Several mechanisms have been suggested as possible explanations of this effect, but they cannot explain some of the established experimental facts. Mainly six models trying to explain the Q drop mechanism, somehow in agreement with some experimental fact and in disagreement with others [51].

3.12 Hot spot and large grain cavities

For cavities with fine Nb grain structure, a global surface heating with a large scattering has been observed at high fields. This point has sustained some theories about magnetic field enhancement and segregation impurities at grain boundaries. But, since the large grain and single crystal cavities coming, the observation is different. The surface heating is located in hot spots, far from the identified grain boundaries proving that those are not involved in the high field Q-drop. However, hot spots existence can be used for the explanation of the Q-drop origin. Theoretically, these located sources of dissipation can be caused by defects like vortex penetration at grain boundaries, precipitates or non uniform surface oxide layer. Breakdown magnetic field reduction, non linear effect and high field Q-drop increasing are the consequences of hot spots [51].

3.13. Thin film and special cavities Q drop

Superconducting energy gap dependence with the magnetic field Δ(H) could explain the thin film Q-drop, through the low value of the l/ξ_0 key parameter, that is the ratio between the electron mean free path and the coherent length of Cooper pair. According to the Granular Superconductor Theory, losses should be linked with the nature of the Nb coating itself, due to the penetration of

Josephson fluxons in weak links: oxidized sputtered islands in this case. The increase of the thermal resistance at the superconductor-substrate interface could also be put forward as an explanation.

By the other hand, other authors associate the limited performances of thin film cavities with less fundamental facts: lower surface resistances could be reached through significant progress in manufacturing process and in preparation cleanness of the copper cavity substrate.

The sputtered Nb on copper cavities produced by CERN show a strong Q-slope and rarely reach gradients beyond ~20 MV/m, where the Q-drop usually appears. It is therefore difficult to understand these cases in terms of their relevance to the Q-drop phenomenon. The sputtering technology, however, is optimized for the exploration of the effect of different coatings. Some cavities were "dry-coated" with pure oxygen in the sputtering apparatus, which reduced the residual resistance [55] Al-coatings, intended to substitute Nb-oxides, were also tested, showing no effect on the surface resistance [55]

Also, recent single crystal cavities produced by Jefferson Laboratory. Interestingly they as well showed Q-drop and baking benefit, possibly indicating that grain-boundaries do not play the central role in the Q-drop. The measurement result is shown in next figure
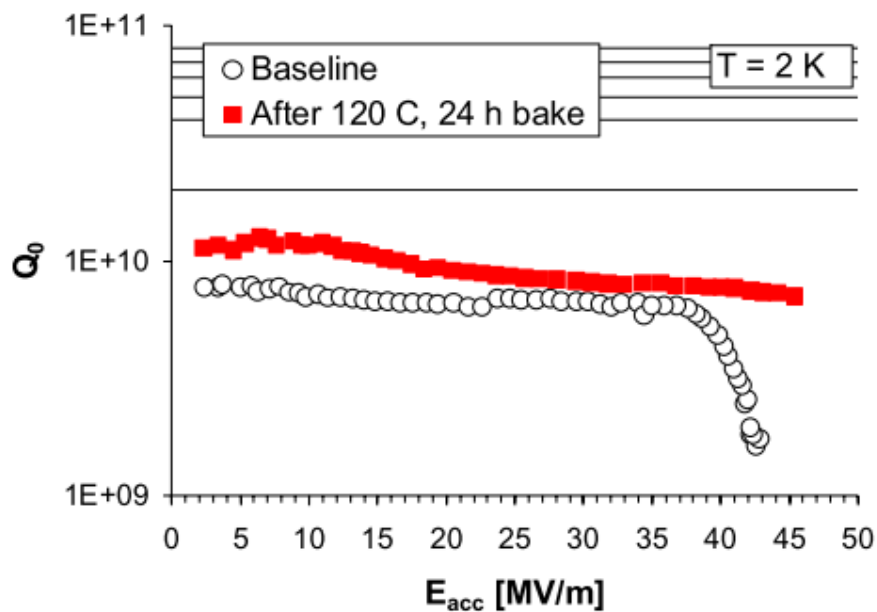
Figure 3.13 Test result of the single crystal cavity at Jefferson laboratory [57]

Certain cavities, however, reached fields beyond the typical Q-drop onset field without showing Q-drop. Among them is the "defect-free" Jefferson Laboratory cavity. This particular world-record single-cell cavity was made from RRR 200 material from Tokyo Denkai. [51]

3.14 Limitations on SRF Cavities

Here it will be mentioned several of the more important limitations along with the method in which they were overcome. In Figure 3.14 is given an overview of the limiting mechanism to reach high values of accelerating fields and Q values. Then it will be described each mechanism separately.
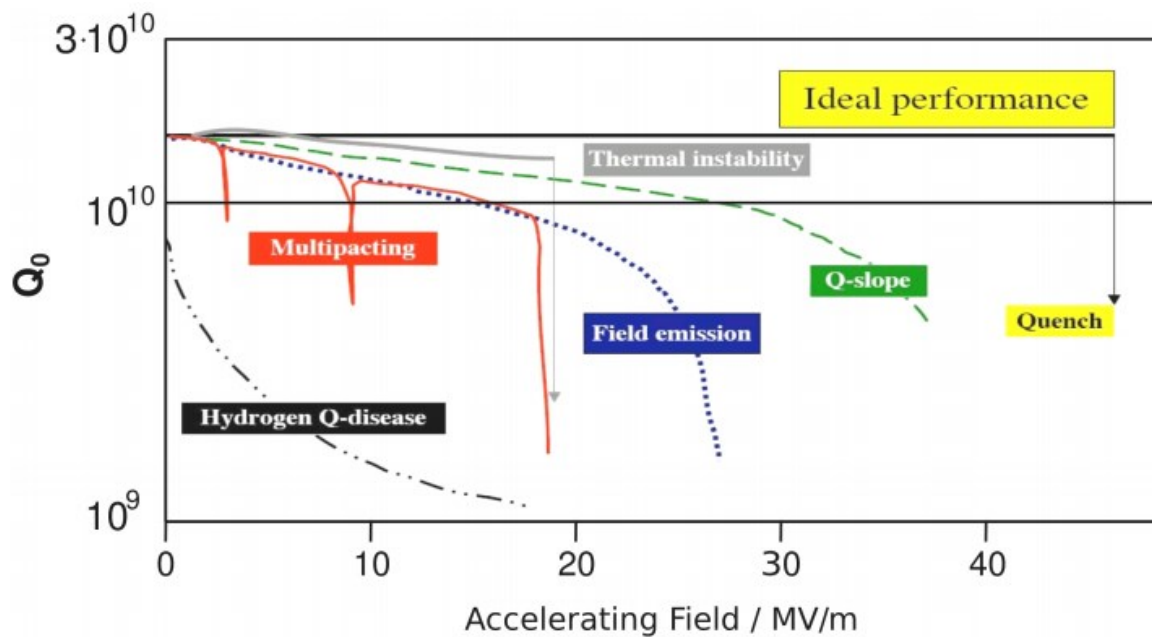
Figure 3.14. Performance limitations regarding the quality factor Q or the accelerating electric field E in the Q vs (E) curve [57].

3.14.1 Q-disease

In this mechanism the degradation of the quality factor starts from Eacc ≈ 0, and it is due to hydrogen contamination of the niobium surface that is exposed to the RF field. The production and treatment procedures of niobium cavities (forming and welding, chemical treatments, etc.) can cause contamination since the niobium lattice has a large affinity for hydrogen [57]. The creation of Nb-H

leads to low quality factors ($Q0 \approx 1e^8$) already at low fields for cavities with high RRR and high frequencies. Losses induced by the contamination have to be attributed to the formation of niobium hydrides in the RF surface during cool down at temperatures between 150-60 K. Reducing the hydrogen pollution it is possible by baking the cavities at 700-900K to degas the bulk material. A rapid cool-down along the critical temperature reduces the probability to create hydrides.

Fortunately, this mechanism experimentally has been absent on Nb/Cu technology due to the less demand on cryogenic system cooling velocity and reliability [58].

3.14.2 Multipacting

Multipacting, multiple impact electron amplification (MP) in cavities is a resonant process in which an electron avalanche builds up within a small region of the cavity surface due to a confluence of several circumstances. Electrons in the high magnetic field region of the cavity travel in circular orbit segments returning to the RF surface near to their point of emission, and at about the same phase of the RF period as for their emission. Secondary electrons generated upon impact travel similar orbits. If the secondary emission yield for the electron impact energy is greater than unity, the number of electrons increase exponentially to absorb large amounts of RF power and deposit it as heat to lower the cavity Q. This form of MP is named "one surface" or "one-point" MP. Depending on the cleanliness of the surface, the secondary emission coefficient of niobium surfaces prepared by cavity treatment methods is larger than unity for electron impact energies between 50 and 1000 eV [59].
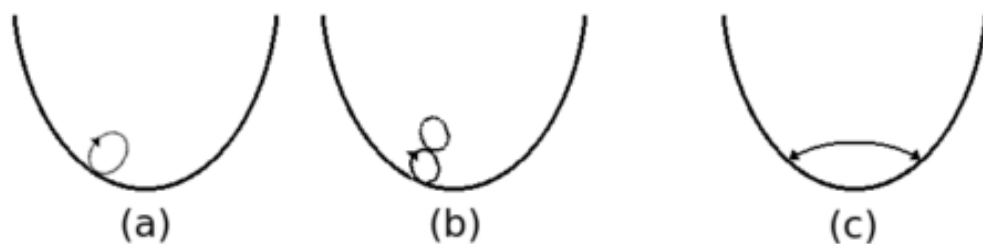
Figure 3.15 Schematic examples for multipacting (MP): (a) 1st order MP, (b) 2nd order MP, (c) two point MP [38].

As was shown in previous figure, the RF field induced in the cavity accelerates and deflects the electron in a way that it may hit the cavity wall again.

3.14.3 Field emission

Field emission is a general obstacle to reach high surface electric fields in accelerating cavities. At the onset of field emission, the Q value of a niobium cavity typically starts to fall due to the exponential increasing electron currents emerging from emitting spots on the surface [59].

Field emission means the emission of electrons from the metal surface by the electric field itself. In general, the electrons are trapped in the metal. Application of a sufficiently high electric field leads to a decrease of the potential barrier inhibiting the release of electrons. Electrons can escape the material through the potential barrier and induce a dark current.

The electrons may either hit the cavity or material like flanges or couplers causing radiation, which can be detected using x-ray sensors, and eventually thermal breakdown if the energy deposition of the electrons in the superconducting material is too high. Dark currents along the beam axis can cause problems in the accelerator itself. Other reasons for field emission, especially for high accelerating fields, can be surface irregularities leading to field enhancement and to the liberation of electrons. Those are still an important limitation. [57].

A detailed temperature map shows line heating (see next figure) along the longitude at the location of the emitter.
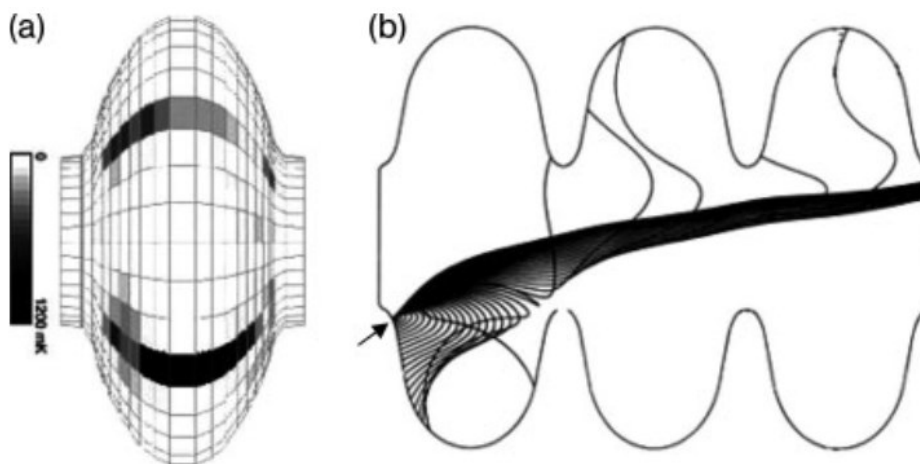
Figure 3.16 a) Temperature map from the heating of impacting field emitted electrons b) Calculated field emitted electron trajectories in a three-cell 1.5 GHz cavity operating at E pk=50 MV/m [41].

There are two emission sites producing a line-heating profile. In Figure 3.16 b, the field emitter is located (at the arrow) in an end cell, just below the iris, where the surface electric field is

44 MV/m. Note that a significant number of electrons emitted in the part of the RF cycle when the magnetic field is strong bend back and strike the wall near the emitter [41].

3.14.4 Thermal breakdown

Thermal breakdown, or quench, is a phenomenon where the temperature of part or all of the RF surface exceeds the critical temperature, becoming normal conducting and rapidly dissipating all stored energy in the cavity fields. Thermal breakdown is generally a localized effect, in which a defect in the RF surface dissipates power faster than the surrounding superconducting walls.

The field at which breakdown occurs is dependent upon multiple factors, including thermal conductivity of the bulk niobium, heat transfer from the niobium to liquid helium bath, and size and resistance of the defect.

The primary method of bypassing the thermal breakdown limitation has been improving the thermal conductivity of the niobium. Improved thermal conductivity comes from improved purity of the metal [60].

Chapter 4.

THIN FILM DEPOSITION

Thin films allow combining the bulk properties of materials with the surface properties of other. Many materials are needed as the demand for high technology products increases. An efficient, and most often less expensive way to meet the increased demands is the use of thin films. Thin films are material layers with thickness ranging from a few atomic layers (~ nm) to a few micrometers. Thin films can be deposit by several techniques: electroplating, chemical vapor deposition, physical vapor deposition, and a number of combinations of these methods [27].

Physical vapor deposition methods for producing coatings in a vacuum environment can be separated into two main groups: (1) those involving thermal evaporation techniques, where the material is heated in vacuum until its vapor pressure is greater than the ambient pressure, and (2) those involving ionic sputtering methods, where high-energy ions strike a solid and knock off atoms from the surface. Ionic sputtering techniques include diode sputtering, ion-beam sputtering and magnetron sputtering.

In this chapter will be explained the principal ionic sputtering techniques in order to deposit thin films.

4.1 Sputtering

The sputtering process was first reported in 1852 by Grove. It has involved significantly since then to the point that in the last 50 years it has been used to deposit thin films in many applications [28].

Several terms can be used to understand the sputtering process: cathodic sputtering, diode sputtering, RF or DC sputtering, ion-beam sputtering and reactive sputtering, but all of these processes are variants of the same physical principle. Sputtering is the process where atoms or molecules of a material are ejected from a target by the bombardment of high energy particles. Specifically, cathodic sputtering is a process in which the bombardment is produced by positive ions derived from an electrical discharge in a gas and the material is ejected from the target in order to obtain quantities of material that can be coated directly onto substrates.
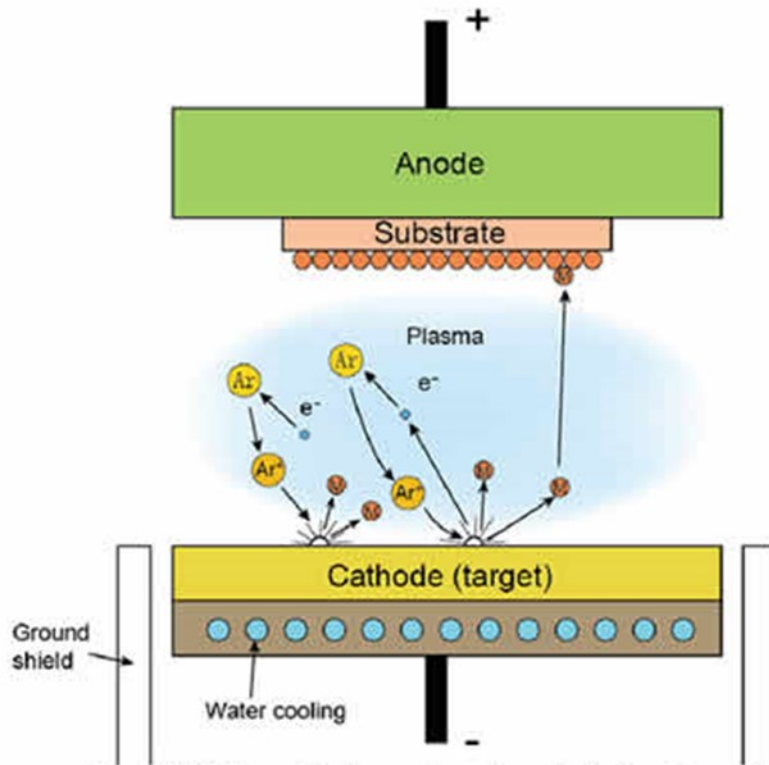
Figure 4.1 Sputtering deposition. In DC diode sputtering system, Ar is ionized by a potential difference, and this ions are accelerated to a target. After impact, target atoms are released and travel to the substrate

In order to have an efficient and useful coating process, several criteria must be met. I) Ions of sufficient energy must be created and directed towards the surface of a target to eject atoms from the material. II) Ejected atoms must be able to move freely towards the substrate with little impedance to their movement. This is the reason why the sputtering technique is a vacuum process: low pressures are required to maintain high ion energies and also to prevent too many atom gas collisions after ejection from the target. It is important to explain the concept of mean free path (MFP) that is the average distance that atoms can travel without colliding with another gas atom. The MFP varies with the pressure and in order to obtain relatively unimpeded travel through a gas, it is necessary to work at pressures around 1 Pa ($1e^{-2}$ mbar) or better; above this pressure the material is subjected to many gas collisions and the deposition rates are very low.

4.2 Sputtering mechanism

As sputtering process is a glow discharge or a plasma process, which uses ionized gas atoms or molecules accelerate in an electric field to erode a material from a source, a strong negative field is applied to the target to attract positive ions, hence a sputter deposition is referred to as the cathode. If a thin film with the same chemistry composition as the target is desired, a noble gas (e.g. Argon) ambient is typically used.
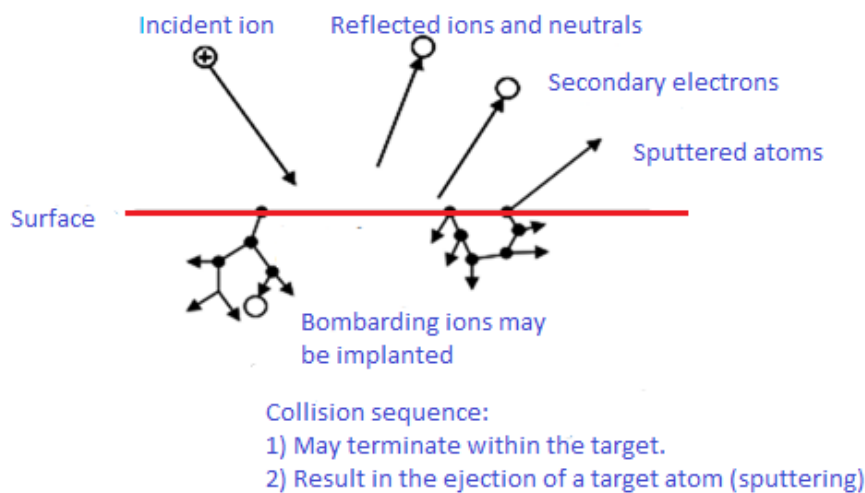
Figure 4.2. Interactions of ions during the deposition.

Figure 4.2 shows the phenomena that can occur during the sputtering process in which, 1) the ion may be reflected, probably being neutralized in the process. 2) The impact of the ion may cause the target to eject an electron, usually referred to as a secondary electron. 3) The ion may become buried in the target. This is the phenomenon of ion implantation. 4) The ion impact may also be responsible for some structural rearrangements in the target material. 5) The ion impact may set up a series of collisions between atoms of the target, possibly leading to the ejection of one of these atoms.6) .This ejection process is known as sputtering.

When an ion with energy more than about 30 eV hits a surface, part of this energy and momentum of the incoming ion will through lattice collisions, be reversed and may cause ejection of surface atoms, i.e. sputtering. [29]. The sputtered atoms leave the target surface with relatively high energies (~10 eV) respect evaporation atoms (~0.1 eV). The average number of the atoms ejected

from the surface per incident ion is called sputtering yield [30]. The ion source is usually a plasma (an electrically neutral mixture of positive ions and electrons) generated by electron impact in a noble gas at sub-atmospheric pressures (2-3 Pa). The ions are accelerated in an electric field obtained by applying a negative potential with respect to the plasma potential to an electrode immersed in that plasma. The ejected or sputtered atoms can be condensed on a substrate to form a thin film.

The sputtering yield S, depends on several factors, such as the mass and the energy of the incident particles, the mass and energy of the sputtering atoms, the crystallinity of the target, etc. This term can be described as:

$$S = \frac{Number\ of\ sputtered\ atoms}{number\ of\ incident\ ions} \tag{4.1}$$

The S value can range from 0,1 to 10. The deposition rate is a function of the sputter yield, the flux of ions impinging on the target, transport of the deposited flux to the substrate, and sticking of that material to the substrate.

4.3. DC Magnetron sputtering

In order to get high sputtering rates and good film performance, DC magnetron sputtering is widely used.

As was explained before, in the basic sputtering process, a target (or cathode) plate is bombarded by energetic ions generates in a glow discharge plasma, situated close to the target. The bombardment process causes the removal or sputtering of target atoms that can condense on a substrate as a thin film.

Secondary electrons can be emitted from the target surface due to the ion bombardment and these electrons play an important role to maintain the plasma. The sputtering process has been used for many years and many applications however this process is limited by low deposition rates, low ionization efficiencies in the plasma and high substrate heating effects. This limitations have been overcome by the development of magnetron sputtering.

The magnetron target is based on the work carried out by Penning more than 60 years ago, however the planar magnetron, which is the most widely used target assembly was not introduced until 1970 [31].

Magnetron sputtering involves placing magnets behind the sputtering target. The resulting magnetic field influences the trajectories of moving charge particles by the Lorentz force. The result is the confinement of the electrons near to the sputtering target that increases the ionization in the working gas. Ions are not confined here due to the charge to mass ratio is much smaller, and therefore ion trajectories are not strongly influenced by the magnetic field [27].

Magnetrons uses the fact that a magnetic field configured parallel to the target surface can constrain secondary electron motion to the vicinity of the target. The magnets are arranged positioning one pole at the central axis of the target and the second pole is formed by a ring of magnets around the outer edge of the target. Trapping the electrons in this way it is possible to increase the probability of ionization that results in a dense plasma in the target region. This in turn, leads to increased ion bombardment of the target, giving higher sputtering rates and also higher deposition rates at the substrate. In addition the efficiency of this process allows the discharge to be maintained at lower operation pressures (typically, $1e^{-3}$ mbar, compared to $1e^{-2}$ mbar) and lower operating voltages (typically,-500V, compared to -2 to -3 kV) than basic sputtering mode [33].
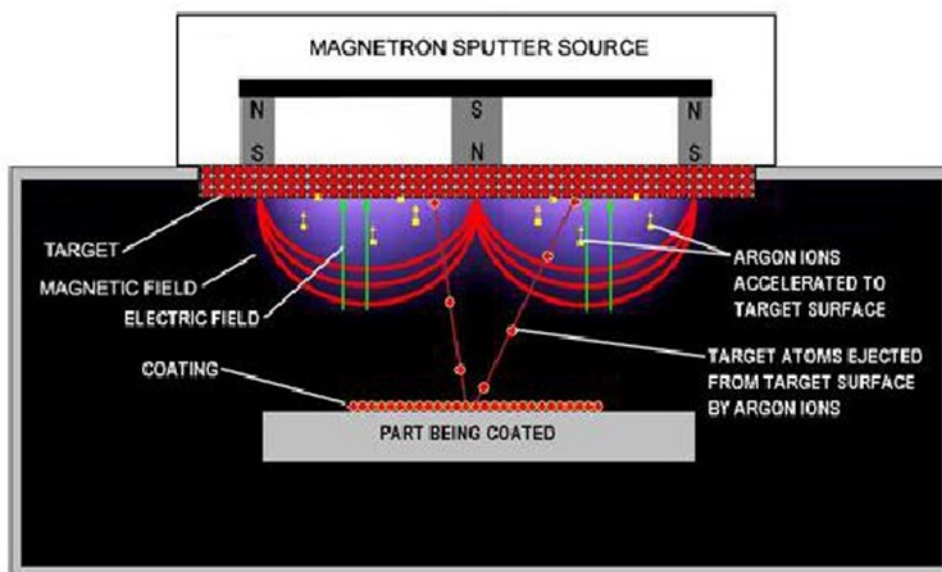
Figure 4.3. Magnetron sputtering technique.

The efficiency of the available electrons can be incremented by a magnetic field parallel to the cathode surface that confines the plasma. A general rule for the shape of the magnetic field is:

1) "The magnetic field must born from the cathode and die onto the target".
2) A plasma confinement is achieved, while magnetic and/or electrostatic mirrors trap the electrons. The magnetic field traps and forces the electrons to describe helical paths around the lines of magnetic When vectors B and E the particles are freely accelerated, while when there is an electric field component E⊥(Volts/cm) perpendicular to B, a drift of speed V_E occurs.

$$V_E = \frac{\vec{E} \times \vec{B}}{B^2} \tag{4.2}$$

4.4. Balanced and unbalanced magnetrons

The difference in performance between the two types of magnetron is very significant. In a conventional magnetron (CBM) the plasma is strongly confined to the target region. A region of dense plasma normally extends some 60 mm from the target surface. Films grown on substrates positions within this region will be subjected to concurrent ion bombardment which can strongly influence the structure and properties of the growing film. Substrates placed outside this region are in an area of low plasma density and the ion current at the substrate is generally insufficient to modify the structure of the film.

The energy of the bombarding ions can be increased by increasing the negative bias applied to the substrate. However, this can lead to defects, increasing the film. Thus, it is difficult to deposit fully dense films on complex components using a conventional magnetron.

A drawing of a conventional balanced magnetron sputtering cathode is shown in figure 4.4 in which the magnetic field lines loop between the inner and outer magnets, and the return field lines are contained by the holder where the magnets are mounted [33].
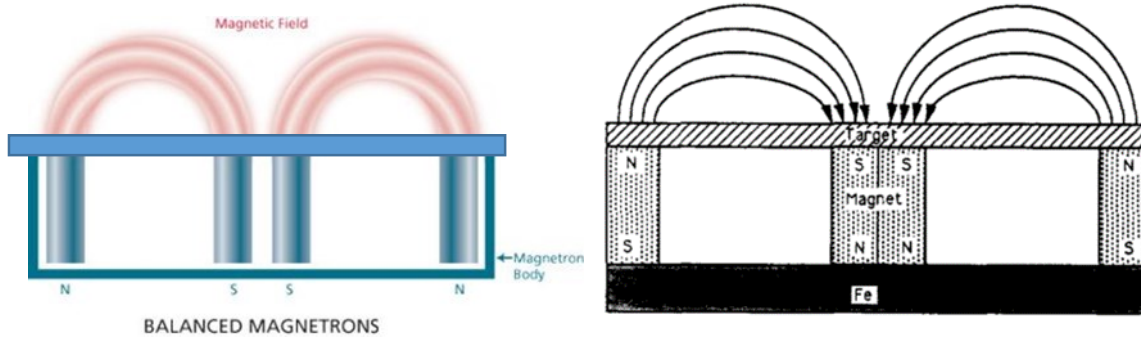
Figure 4.4.Cross section drawing of the conventional balanced magnetron.

When the conventional balanced magnetron is unbalanced, the strength of one set of magnets (the outer set or the inner set) is increased respect to the other and some of the magnetic field lines expand away from the target surface [33]. In this case, not all the magnetic field lines are closed between the central and outer poles in the magnetron, but some of them are confined towards the substrate, and some secondary electrons are able to follow these field lines. Consequently, the plasma is no longer strongly confined to the target area, but is also allowed to flow out towards the substrate. Thus, high ion currents can be extracted from the plasma without a bias on the substrate. This configuration is called "unbalanced magnetron of the second type".

However three is an opposite case in which the magnetic field lines do not close in on themselves, the lines are confined towards the chamber walls and the plasma density in the substrate region is low. This configuration is called "unbalanced magnetron of the first type". Figure 4.5 shows the configuration of the first and second unbalanced magnetron type.
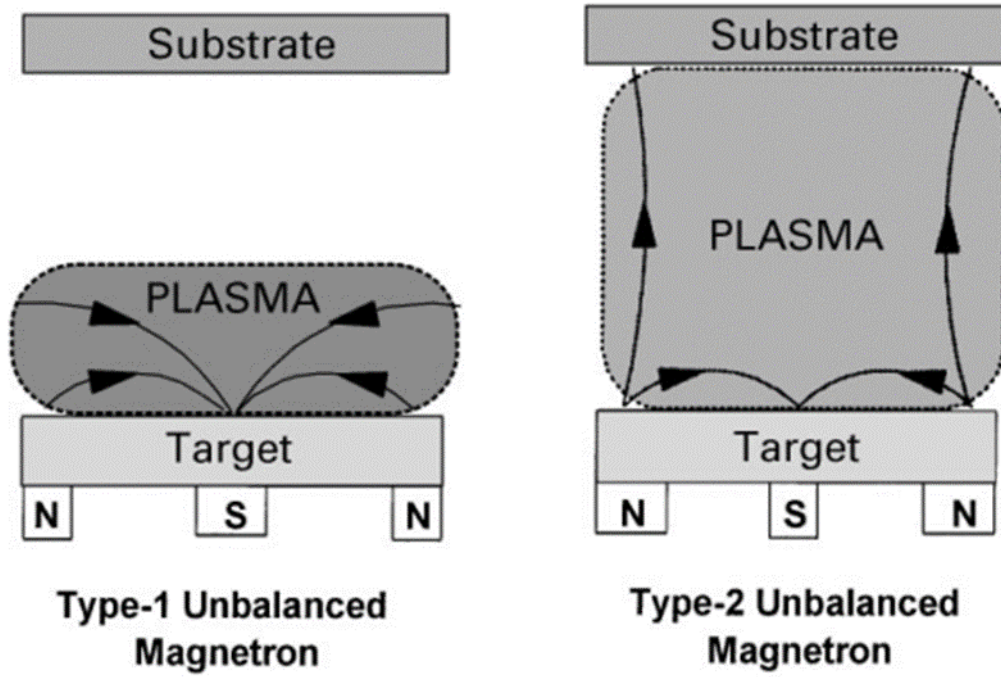
Figure 4.5. Plasma confinement of unbalanced magnetron.

Chapter 5.

THE VACUUM SYSTEM

In order to deposit a good superconductive thin film, a high vacuum system is required. For this reason a vacuum chamber was built taking into account the QWR cavity dimension and maintaining the highest standards of design. In this chapter will be presented the main parts of the vacuum system used to carry out the deposition of the thin film. The vacuum system consist of three mean parts: the cathode, the magnetron and the vacuum chamber. In one of this elements will be presented below.

5.1. 3D drawing of the vacuum chamber

The vacuum chamber is formed of a stainless steel vessel of 700 mm diameter and 2000 mm high. Inside the chamber is contained the niobium cathode, within which is located the circular magnetron as is shown in the following figure.
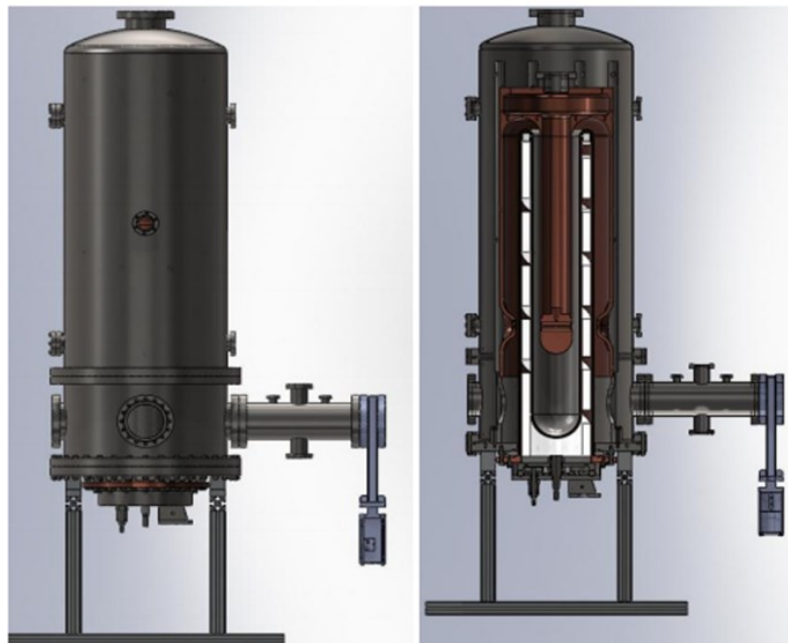
Figure 5.1. 3D drawing of the vacuum chamber. Left: Front view of the chamber assembled. Right: Cross sectional view of the vacuum chamber.

The system consists of a number of essential elements for the construction of a high vacuum system. Two pumps are connected in order to reach a vacuum of $1e^{-8}$ mbar. The rotary pump is used

to reach a pressure of $1e^{-1}$ mbar; it is connected to an electro-pneumatic valve and also to a manual angle valve that can be used to make a connection with the He leak detector. The rotary pump is connected to a turbo molecular pump to reach a vacuum pressure of $1e^{-8}$ mbar. A Pirani gauge is placed between the rotary pump and turbo molecular pump to measure the pressure.

A VAT gate valve is placed to isolate the Ultra High Vacuum (UHV) from the vacuum chamber. There is a cross tube on the front side of the chamber where is placed a viewport order to see the argon plasma and the rotation magnetron during the deposition and a leak valve that is used to fill the chamber with the argon flux in order to generate the plasma during the magnetron sputtering process. Also there are two shut off valves, to fill the chamber with nitrogen during the venting and reach atmospheric pressure. Two gauges, a capacitor and a Bayard Alpert gauge are also connected to measure the pressure in this area.

The following figure shows the scheme of all components on the vacuum system.
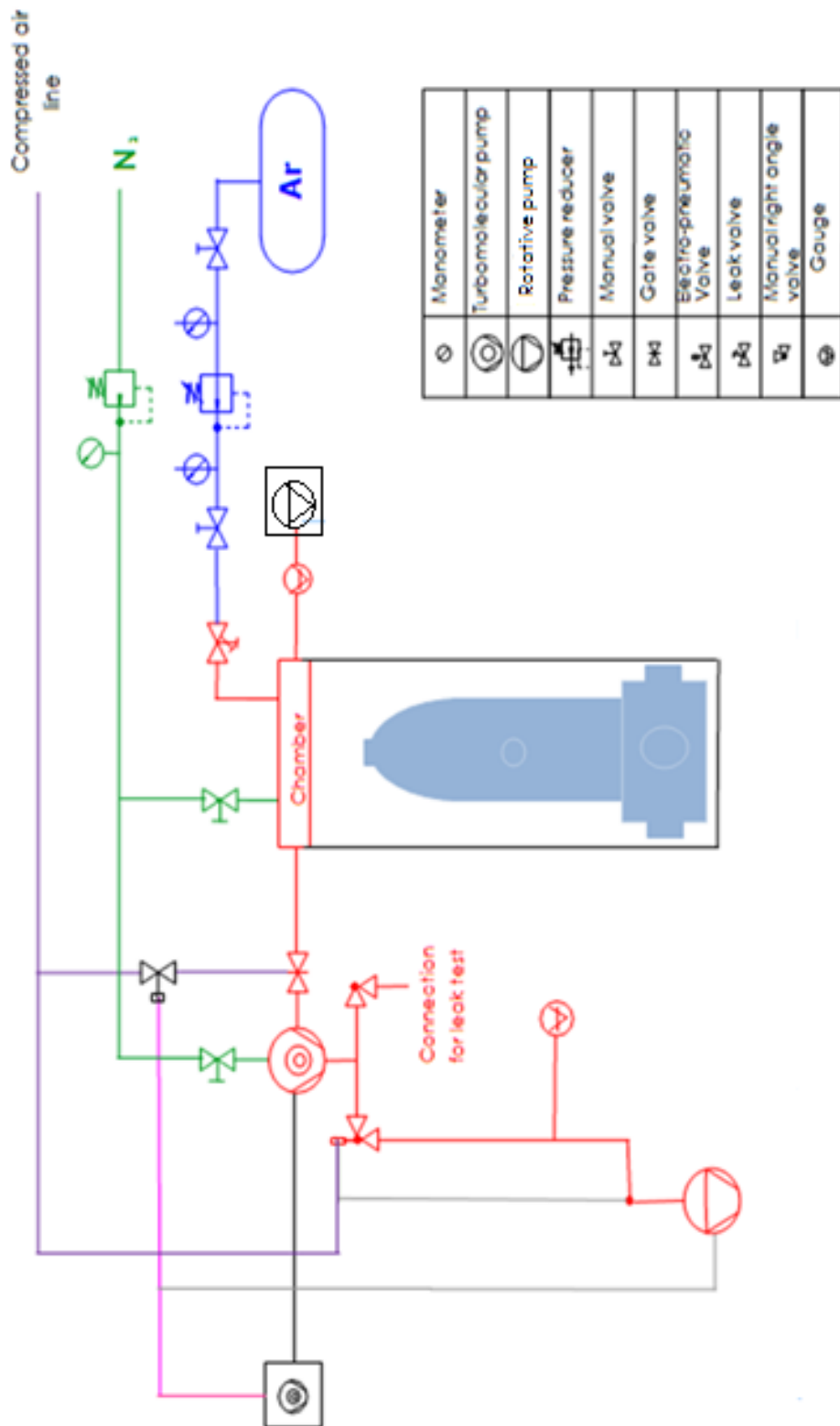
Figure 5.2 Scheme of the vacuum chamber assembled [33].

Figure 5.3. Vacuum system assembled.

5.2. The cathode

Part of the methodology was focused on the construction of the cathode with the appropriate shape to deposit the film over the internal walls of a QWRs cavities. Figure 5.4 shows the procedure to build the cathode in which two sheets of niobium were formed mechanically in order to do concentric cylinders, then it was welded by electron beam. By the other hand, Figure 5.5 shows the 3D drawing of the cathode and the cathode built.

Figure 5.4. Procedure used in the construction of the Nb.

Figure 5.5. Niobium cathode.

5.3. The magnetic field configuration

Two magnetic confinement were tested in order to deposit uniformly the thin films. A first configuration was formed using plastimag that is a material made of NdFeB. The second magnetic confinement was built using permanent magnets in order to create the magnetic path. Here will be explained both configurations used in this experiment.

5.3.1. Spiral path with plastimag

Cylindrical magnetron sputtering are been studied from 1970 when the first magnetrons were developed. They can be used to sputter from the surface of approximately cylindrical targets to deposit inside or outside the substrate [34].

In addition rotating cylindrical magnetron sputter deposition is popular for large scale industrial application. With this kind of magnetron the target should be a cylindrical tube which rotates around a stationary magnet configuration pointing in the direction of the substrate. In comparison with the use of planar magnetrons, the rotating cylindrical targets have higher target consumption (around ~80% - 90%), the cooling efficiency is better and consequently the deposition rates are better too and the debris formation is reduced [35].

Magnetron sputtering source can be defined as a diode devices in which magnetic fields are used to form electron traps which are so configured that the ExB electron drift currents close themselves along annular closed trajectories.

The construction of the magnetron is based on this principle in order to decrease the electron losses and increase the plasma [36]. In the first magnetron configuration the magnets are placed on a PVC tube to follow a double spiral path. This path is closed as is shown in figure 5.6. Because of the particular configuration, the magnets are made of Neodymium Iron boron that is a magnetic material easy to mold. The magnetic field of this magnets are axially oriented. With this configuration the uniformity should be satisfactory because the magnetron is connected to a motor to rotate during the cavity deposition

To deposit the cavity on the top, several configurations were be tested along the investigation in order to deposit a uniform thin film.

Figure 5.6. 3D drawing of the first configuration of magnetic field. B) Neodymium- Iron –Boron placed along the double spiral path.

5.3.2. "U" Path with permanent magnets

The scope of the construction of this magnetic source was the deposition of thin films onto cylindrical substrates, specifically superconducting quarter wave resonator cavities. This configuration was built taking into account the previous experience using the first source of magnetic field, so it was decided to improve not only the magnetic path configuration but also the choice of materials in order to make it lighter and easy to assemble.

The permanent magnets formed of Neodymium Iron boron are placed along a stainless steel tube following a particular path. The magnetron also is connected to a motor in order to rotate and consequently rotate the plasma on the cathode surface to guaranty a uniform thickness of the film.

As in previous configuration in order to confine the plasma on the top of the cavity, several configurations were tested and will be show in chapter 8. Figure 5.7 shows the second magnetron configuration.

Figure 5.7. Second configuration of magnetic field.

5.4. The rotation system

In addition to the particular configuration of magnetic field that are been proposed in this thesis, it is important to note one of the principal features that makes innovative this technology. There are several configurations of cylindrical magnetron configurations used to deposit thin films by the using of a rotating target that allows a uniform coating, however in this study is presented a new method in which the target does not move but the magnetic path is joined to a motor to be rotated during the deposition, in this way it is possible to confine the plasma along the substrate.

The magnetron structure is placed inside the cathode and supported by 36 stainless steel spheres that improve the rotation, then the magnetron is fixed by a motor on 5 N.m. Figure 5.8, shows the assembly of the rotation system.

Figure 5.8. Rotation system.

Chapter 6.

EXPERIMENTAL PROCEDURE

In this chapter will be explained the complete procedure to carry out the investigation. The first part will be focused on the materials and equipment used to build the vacuum system, to perform the deposition and characterize the films and the resonator, and then will be explained the methodology followed for depositions. At the end will be explained the characterization methods for the thin film and the cavity.

6.1. Materials and equipment

Table 2, shows the materials and equipment used

Table 2 Materials and equipment used in this project

MATERIALS	EQUIPMENT
Stainless steel 316L	Vacuum chamber
Quartz samples 9x9mm	RF equipment
Nb sheets 900x900mm	T_c and RRR equipment
Copper strips 900mm length	Scanning electron microscope (SEM)
PVC tube 900mm length	Profilometer
NdFeB magnets	Power supply 30Kw
Strip aid solution	Ultrasonic bath
Argon gas	Motor 5N.m
Nitrogen gas	Lathe
Liquid He dewar	Leak detector
Soap Rodaclean NGL	Gas analyzer
Ethanol	Cryostat
Acetone	Baking system

6.2. Methodology

The methodology used to carry out this project was divided in several stages. Hereunder will be presented in detail, each part of the procedure followed to improve the magnetic field source and then to deposit the QWR cavity.

6.2.1 Magnetic field configuration

In order to deposit uniformly the complex shape of the QWR, several configurations of magnetic field were tested. The first part of the methodology was focused on the analysis of the magnetic field lines and the interaction between the magnets placed on the bottom of the magnetron body and the magnets placed on the top of the magnetron body.

A FEM (Finite Element Method) tool was used to perform simulations of magnetic field in 2D. Simulations have been done changing the magnetic material, magnet shape and the distance between the magnets.

6.2.2. Small cathode configurations

Due to the fact that in the vacuum chamber it was impossible to see the plasma during the deposition, in addition to the simulations, a test cathode made with stainless steel was built and was placed in another vacuum chamber in order to observe the plasma during the sputtering process. The parameters used to turn on the plasma are shown in table 4. Figure 6.1 shows the test cathode.

On the other hand figure 6.2 shows the magnetron placed inside the test cathode during the deposition.

Table 3. Parameter used to test the configuration of magnetic field.

Parameter	Values
Vacuum pressure (mbar)	$1.5e^{-6}$
Sputtering pressure (mbar)	$8e^{-3}$
Power (W)	590
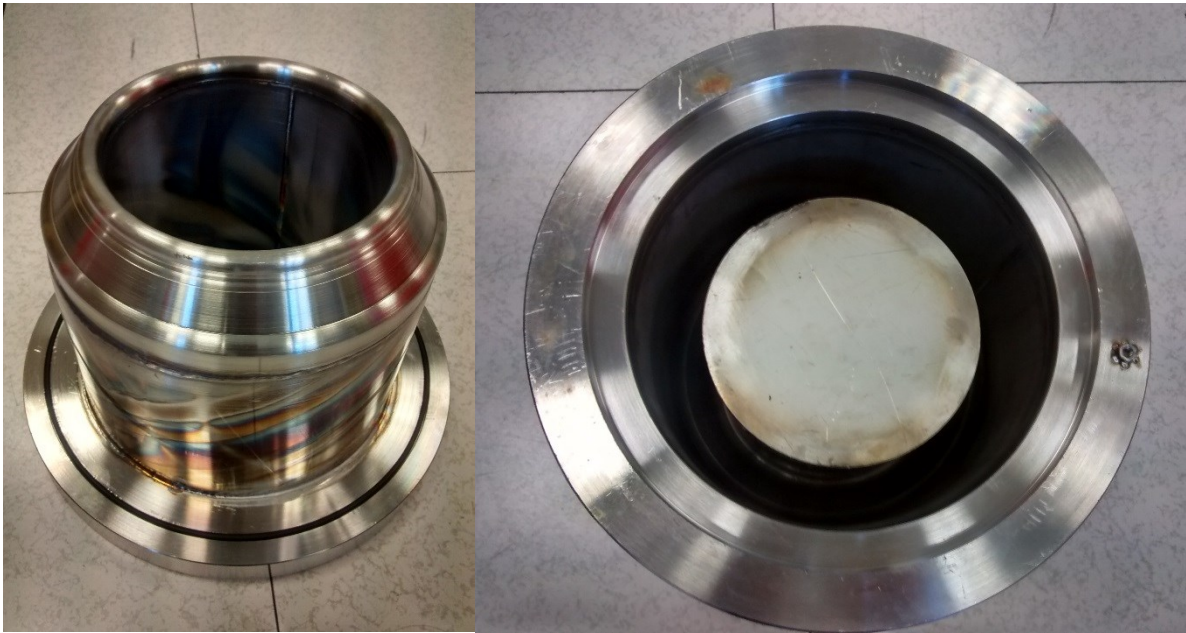
Figure 6.1 a) Stainless steel test cathode, b) top view of the test cathode.

Figure 6.2 Magnetron placed on the vacuum chamber during the sputtering process.

6.2.3. Deposition of Niobium onto copper quartz

The first aim of this project was focused on the uniform deposition of the thin film. In order to do this quartz samples of 9x9mm were placed over a sample holder along the QWR cavity interior. Quartz sample were cleaning using an ultrasonic bath with water and Rodaclean soup for 30 min, as in shown in Figure 6.3.

Figure 6.3 Ultra sonic bath used to clean quartz samples.

After the cleaning, quartz were immersed in a beaker with ethanol and subsequently dried with nitrogen. Quartz were placed in a sample holder that follows the same shape of the QWR cavity, as is shown in Figure 6.4. Samples were placed in strategic positions in order to measure the properties along the entire surface of the cavity (See Figure 6.5)

Figure 6.4. a) Sample holder b) sample holder on the QWR cavity.
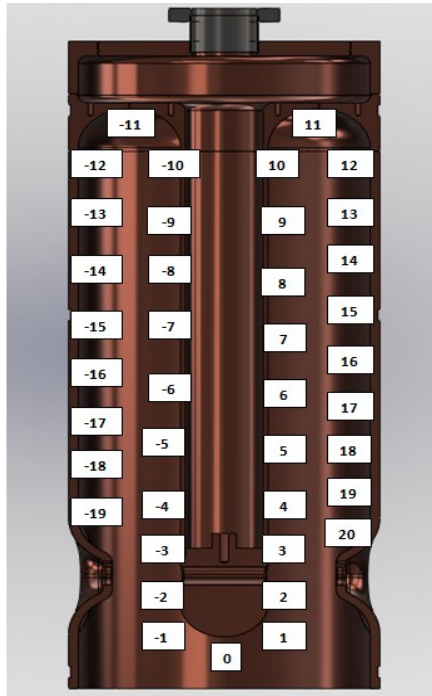
Figure 6.5. Sample positions on quarter wave resonator cavity.

6.2.4. Vacuum

After the mounting, the cavity and quartz samples were placed on the vacuum chamber. Figure 6.6 shows the cavity mounting.

Figure 6.6. QWR during the mounting on the vacuum chamber.

Ultra high vacuum is required for both purity and control of the sputtering process. An automatically vacuum system consisting of a rotary pump and a turbo mechanical pump was used in order to reach a base vacuum around $1e^{-7}$mbar. The rotary pump used as a primary pump to reach the

60

vacuum until $1e^{-1}$. On the other hand the Turbo molecular pump is used to pump the chamber in the UHV regime at lower pressures than $1 e^{-8}$ mbar. It works moving molecules or atoms, when they hit a surface in a fast moving and pushing the particle in a specific direction in conjunction with a gas flow in the same direction [38].

6.2.5 Baking

Outgassing is the spontaneous liberation of gases from the walls of a vacuum system. The gas could be released from two process: Gas diffusion from the interior of vacuum chamber walls to their inner surface. This process is followed by gas desorption into the chamber volume that contributes to the outgassing of the vacuum system. The second process is the release of vapors or gases absorbed onto the inner surface of the walls. In this process the gases can be adsorbed onto the chamber inner surface while it was exposed to the environment.

In high vacuum range the predominant gas is usually water vapor resulting from the environment humidity and Hydrogen in stainless steel is the main gas load in UHV/XHV systems. SS is the main gas load in UHV/XHV systems. In order to reduce the hydrogen content in the bulk, many techniques can be used. One of these techniques is the baking of the vacuum system to remove the water vapor which has to be performed around 150°C [38]. In this project the baking was controlled by an automatic system in which the temperature and time can be set (See Figure 6.7).

Figure 6.7. Baking controller.

Thermocouples and heating resistances were places on the vacuum chamber as in shown in Figure 6.8.

Figure 6.8. Resistors and thermocouples placed on the vacuum chamber.

6.2.6. Pre-sputtering

It is mandatory to reach a vacuum pressure as low as possible because the impurities interfere with the RF superconductivity of niobium and limit the performance of a sputter coated niobium film cavities. [40]In any vacuum system after the initial evacuation of the atmospheric air, the vacuum must be maintained by pumping the gases produced by the system components; for this reason has been used getters which are materials able to trap gas molecules to form stable compounds or solid solutions [41].

Niobium is a powerful getter that can be used to dissolve and trap gases like hydrogen and oxygen and also other light elements like carbon and nitrogen [41].

A strict methodology has been adopted both for preparing the system before the deposition. A niobium magnetron has been placed on the top of the vacuum chamber in order to be used as a getter pump before the deposition of the film. This process, designed in this procedure "Pre-sputtering" has been performed fixing the parameters shown in Table 4.

Table 4. Parameters used to perform the Pre-sputtering process.

Parameters	Values
Current	2(A)
Voltage	350 (V)
Time	15 (min)

Figure 6.9 shows the niobium magnetron placed on the top of the vacuum chamber.

Figure 6.9. Niobium magnetron placed on the top of the vacuum chamber.

6.2.7. Sputtering of niobium onto quartz samples

After this process the system was ready to deposit niobium thin films onto quartz samples. The sputtering parameters were changed continuously in order to improve the superconducting properties of the thin film. These will be shown in the next chapter with the results obtained in each deposition.

Figure 6.10 shows the vacuum system during the deposition on quartz samples.

Figure 6.10. Vacuum system during the deposition.

6.3. Characterization techniques

6.3.1. Thickness measurements

After the deposition quartz samples were labeled. The thickness was measured by using the profilometer. The profilometer is a tool that drag a stylus across a surface and records the topological profile.

Moreover, a profilometer is a device used to measure relative surface roughness, peak to valley, in order to quantify its roughness. They may operate in either contact or non-contact modes and may use optical or stylus techniques to make the actual measurements [42].

The profilometer used has the followings features: [42].
1. Combines high repeatability, low-force sensor technology, and advanced 3D data analysis.

2. 7.5 angstrom, 1 sigma step height repeatability and a vertical range of up to 1mm.

3. Scan lengths to 200 mm.

4. Low force sensor option offers stylus forces down to 0.03 mg.

5. High aspect ratio tips ideal for measuring Shallow Trench Isolation (STI) etch depth and deep structures.

Figure 6.11 shows the profilometer used to measure the thickness of quartz samples.
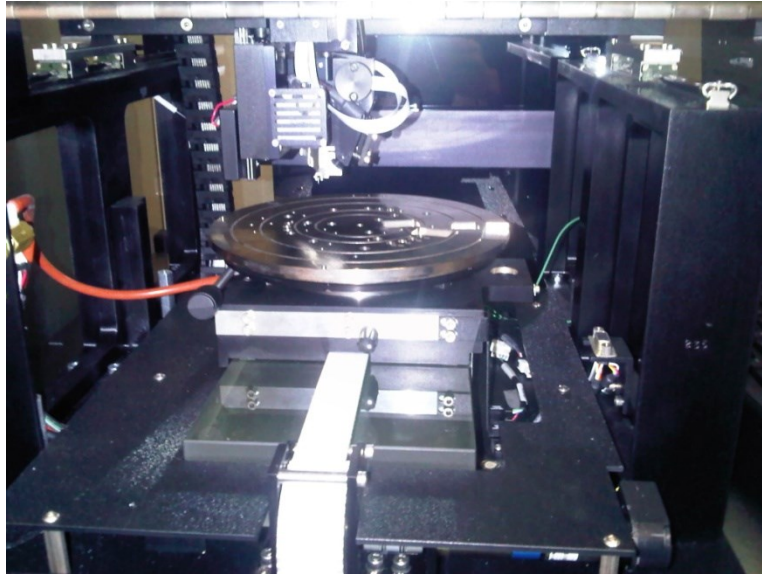
Figure 6.11. Dektak 8 Profilometer used to measure the thickness of quartz samples.

6.3.2 Residual Resistance Ratio and Critical Temperature

After the thickness measurements superconducting properties were also measured. Residual Resistance Ratio (RRR) and critical temperature (T_c) were measured by using the four point method.

The four point method is a DC technique in which the average size of the samples often is around 1-15 mm^2 and 30-300 mm length. The measurement starts cooling down slowly the sample by immersion into liquid helium and the temperature is controlled by temperature sensors. With the four point method one set of conductors drives the current through the sample and the second set picks up the voltage as is shown in Figure 6.12[25].
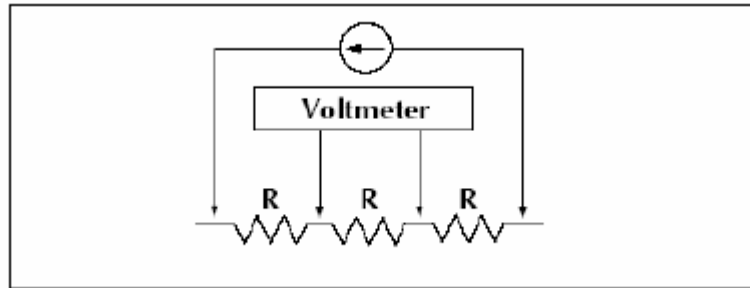
Figure 6.12. Scheme of four point method.
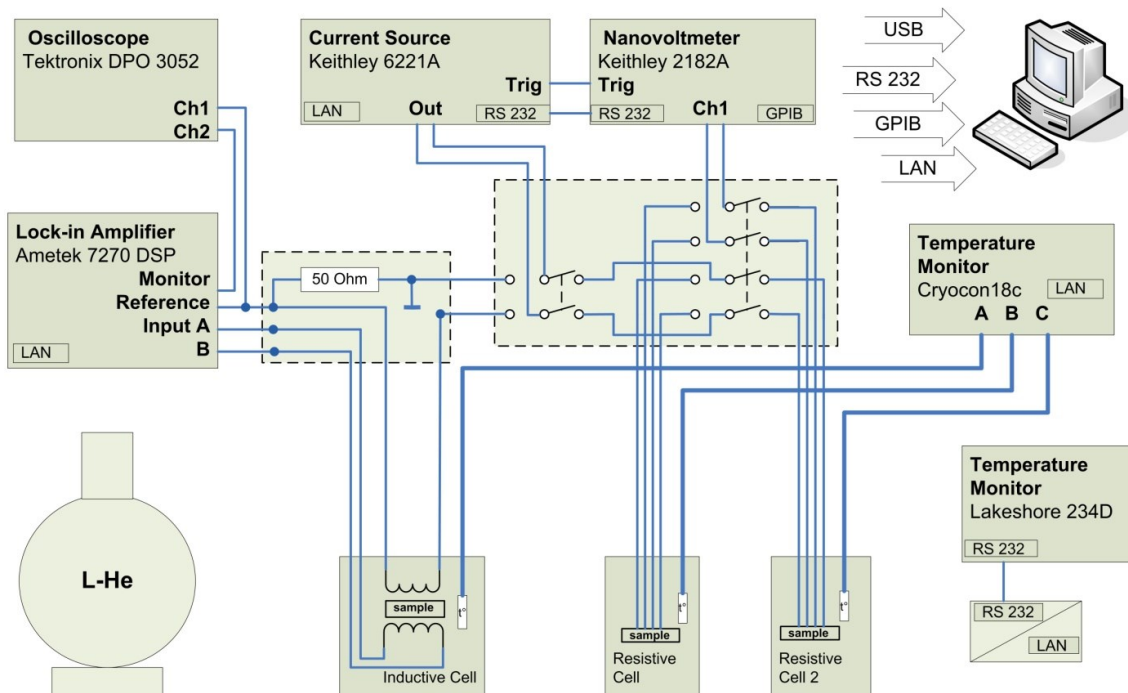
Figure 6.13. Measuring system layout [43].

The resistance is determined using the Ohm's law and in this case the resistance is measured between the two points on the sample where the voltage contacts are located.

The measuring system configuration used at the cryogenic laboratory was shown in Figure 6.13. It can take advantage of the new generation of the current sources that implement DC Delta measuring mode (fast polarity change) in conjunction with a new digital nano-voltmeter with synchronous bipolar readings for the high precision four point resistive sample measurement.

Figure 6.14. a) Resistive sample holder. B) Helium Dewar.

The temperature is measured by a CryoCon 18 temperature monitor that is in test phase using as reference the Lakeshore 234D cryogenic temperature monitor. All the instruments are interfaced with a computer running to a VisualBasic.NET 3.5 software that performs the necessary instruments configuration for two measurement types, the temperature dependence curve acquisition, scaling and visualization, saves the data and calculates three main values: RRR, T_c and dT_c at the end of the measurement [43]. In this project the four point method was used placing the quartz samples in a sample holder structure and cooling down in a liquid helium Dewar (see figure 6.14). A DC current of 2,5mA was applied to the sample and the resulting voltage was measured to determine the resistance, while a specific software was used to acquire data from 300 to 4,2K and plot the curve of resistance versus temperature.

$T_c \pm \Delta T_c$ was measured from the resistances vs temperature curve, applying the following equation:

$$T_C = \frac{T(90\%) + T(10\%)}{2}$$ (6.1)

While the error was calculated using the equation 6.2

$$\Delta Tc = \frac{T(90\%) - T(10\%)}{2}$$ (6.2)

6.3.3 Scanning electron microscope SEM

SEM is a characterization technique that can provide information on surface topography, crystalline structure, chemical composition and electrical behavior on the top of a specimen. In a SEM the incident electrons from an electron gun have energies of 2-40 keV. The most common electron gun is a tungsten filament that is heated to 2500°C to produce thermal emission electrons from its tip. The interaction of the electron beam with the specimen produces secondary, backscattered and Auger electrons, X-rays and perhaps light collected by various detectors in the specimen vacuum chamber. The signal from each detector can be fed to a monitor. The magnification of the image is determinate by the ratio of the side length of the monitor display to the side length of the raster on the specimen [44].

In order to understand the morphology and the grain size of the niobium deposited on the quartz, samples placed along the cavity walls were analyzed with a FEI Scanning Electron Microscopy (SEM XL-30).

6.4. Deposition of QWR

In the final stage of this research the methodology was focused on the surface treatments, the deposition and the characterization of the copper QWR cavity. The first step was the cleaning of the surface preparation of the cavity. A chemical etching was carried out at CERN for 20 minutes. The polishing agent (SUBU) is a mixture of sulfamic acid (H_3NSO_3, 5g/l), hydrogen peroxide (H_2O_2, 5% vol), n-butanol (5%vol) and ammonium citrate (1g/l) [45]. The working temperature of the etching is 72± 1°C. The cavity is after rinsed with sulfamic acid in order to passivate the surface and after was rinsed using 8mbar of ultrapure water in a clean room class 100. After the cavity was dried with ethanol.

After the surface preparation the niobium/copper plate was dismounted and preserved in vacuum. The cavity was mounted on the vacuum chamber in a clean room class 100, as is shown in Figure 6.15.

Figure 6.15. QWR cavity during the mounting on the vacuum chamber.

After the mounting five IR lamps and two thermocouples were connected and assembled over the cavity in order to heat during the outgassing of the cavity and also during the sputtering process (see Figure 6.16).
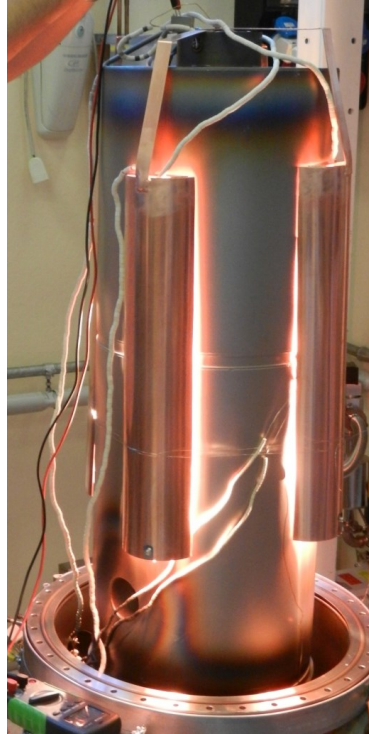
Figure 6.16. IR lamps test before the vacuum chamber closing.

After the mounting the vacuum chamber was closed and it was baked inside and outside for 72 hours at 200°C to reach a good vacuum before the deposition. Table 5 and Table 6 show the parameters used to carry out the pre-sputtering and the magnetron sputtering process.

Table 5. Parameters used to perform the pre-sputtering process of the QWR cavity.

Sputtering pressure (mbar)	Voltage (V)	Current (A)	Time (min)
$8e^{-3}$	335	1	10

Table 6. Parameters used to perform the magnetron sputtering process of the QWR cavity.

Sputtering pressure (mbar)	Power (kW)	Voltage(V)	Current (A)	Cavity temperature (°C)	Time (min)
$6e^{-3}$	30	400	72	450	40

After the sputtering process the QWR cavity was took out the vacuum chamber and it was moved to the chemical laboratory to perform a dust free cavity treatment: A high pressure rinsing was carried out with ultrapure water gun for 20 min, at 100 bar. Figure 6.17 shows the cavity during the cleaning.

Figure 6.17. High pressure rinsing.

After the cleaning the cavity was dried with ethanol and it was closed with a Polyethylene plate.

The cavity was transported to the clean room where the Nb/Cu tuning plate was cleaned with ethanol and dried with nitrogen. The Nb/Cu plate was mounted on the cavity, the RF contact between the cavity and the plate is ensured by mechanical clamping with 72 screws tightened at 5Nm each [45]Figure 6.18, shows the cavity during the mounting of the tuning plate.
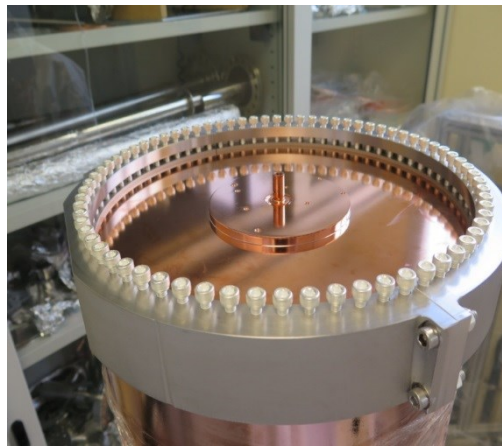
Figure 6.18. QWR cavity during Nb/Cu tuning plate mounting.

The cavity was moved to the cryogenic laboratory where it was mounted on the cryostat stand to start the measurement.

Chapter 7.

THE RF SYSTEM

This chapter presents the RF system used to measure QWR cavities. The first part will be focused on the cryostat design and theoretical bases of RF measurements; then it will be shown a detailed description of the RF system and the software and hardware used for QWR testing.

7.1 Cryostat design

The specific aim of this research is to deposit a superconductive film over the QWR; for this reason in order to get the superconducting properties of the cavity it is mandatory to develop a cryostat. It was the possibility to modify and adapt an existing cryostat located in the cryogenic lab at the laboratory of superconductivity (INFN-LNL) that was built to measure TESLA type cavities. This part of the methodology was focused on the design, construction and test of the QWR cryostat.

The test cryostat adapter was designed by the candidate and his co-tutor taking into account principally the cavity shape. The cryostat for single cells has been designed with the aim of adapting the new parts to the stand, without modifying the structure used to measure the TESLA type cavities. Thus, both types of cavity are measurable at the laboratory of superconductivity of LNL It was built a cryogenic structure including helium vessels or containers, thermal shields, vacuum vessels, supports, current leads, cryogenic lines and instrumentation. Basically, typical considerations were followed:

- Required size and orientation of the cryostat.
- Orientation of the cavity respect to the coupler and pick-up antenna.
- Refrigeration source and temperature.
- Necessary instrumentation and controls [46].

Each component of the cryostat was designed by the using of a CAD software ("Solid Works 2013") allowing the assembly to the main flange. This flange is equipped with two pumping lines (1,8 and 4,2 K), two electrical, two rotating and two RF feed through, a safety valve, the liquid Helium transfer line and its recovery line. Figure 7.1 shows the position of each component on the main flange of the cryostat stand.
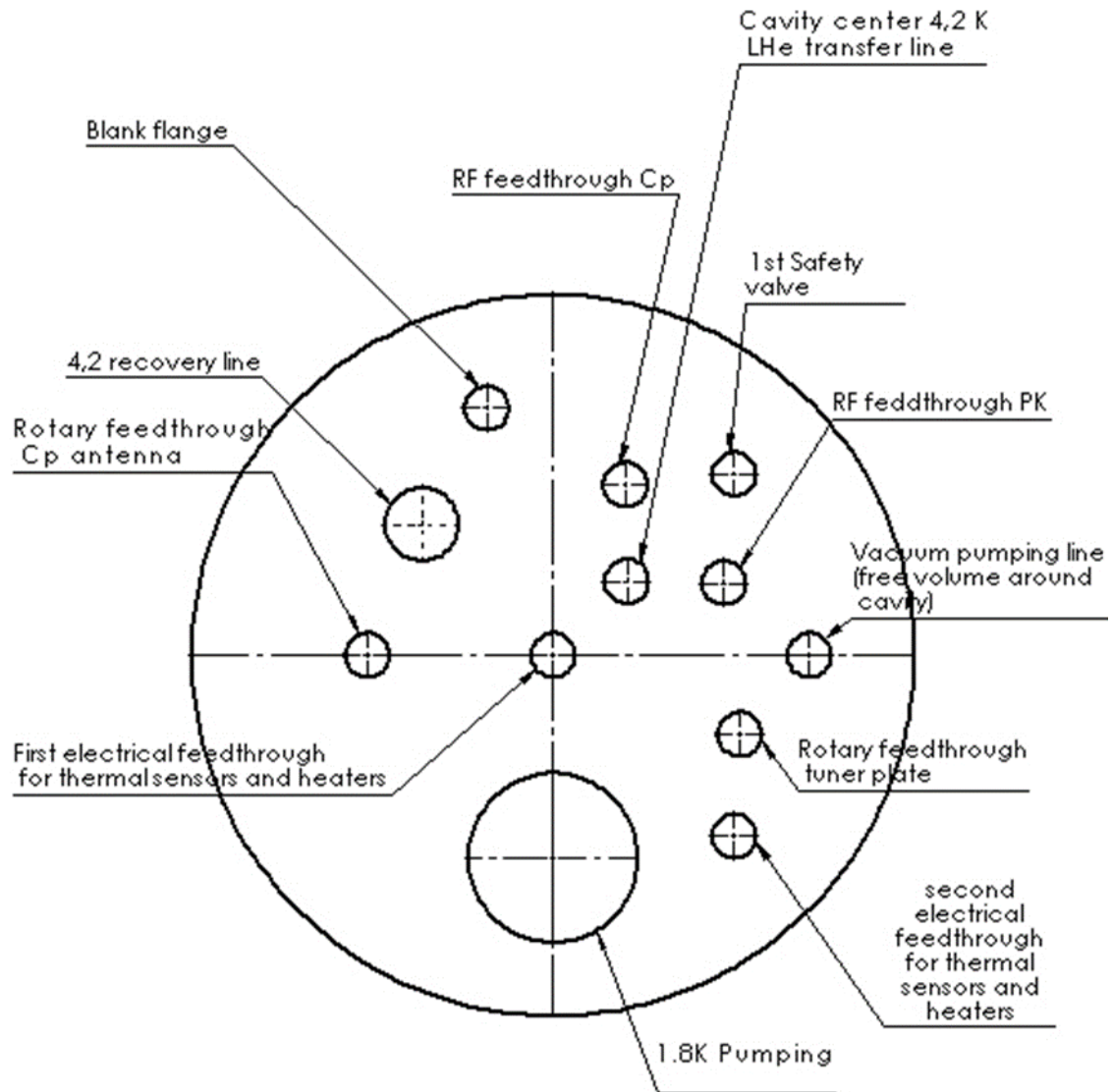
Figure 7.1 Top view of the cryostat flange.

To the cryostat stand it was connected a stainless steel tube using indium seals that remains malleable at cryogenic temperatures and fill imperfections creating a hermetic seal. Then seven thermometers were connected to the cryostat stand: four thermometers were connected to be fixed to the cavity while three thermometers measure the temperature on the copper thermal shields. Figures 7.2 and 7.3 show the cryostat stand during the mounting of thermometers, bellows and pumping lines.

Figure 7.2 Upside down of the cavity stand during the cryostat mounting.
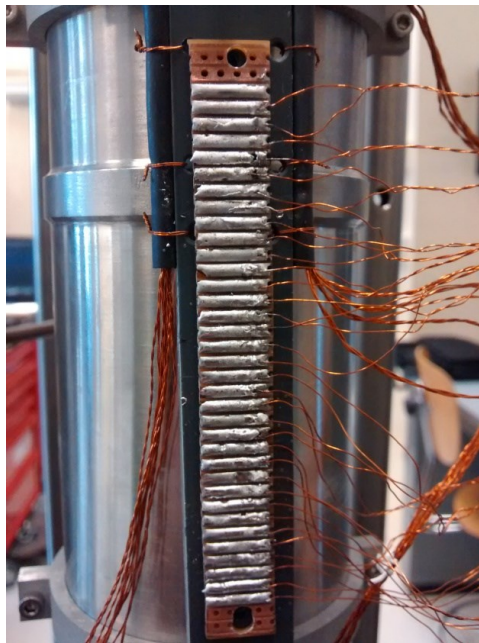
Figure 7.3 Thermometers during their mounting on the cryostat stand.

The cryostat is a device to control low temperatures, so the principal part was a cylindrical Helium vessel. To this vessel is held vertically the quarter wave resonator through a stainless steel bellow to fill the cavity in the center tube. On the other side of the vessel there are two main tubes: a liquid helium transfer line to cool the cryostat to 4,2 K and a tube to evacuate the helium gas by a warm line. Also in this vessel is linked a liquid helium transfer line to cool the system until 1,8 K. The thermal shields made of copper are placed on the top of the stand and can be cooled with the recovery helium cold gas. Figure 7.4 shows the test cryostat stand during its construction.
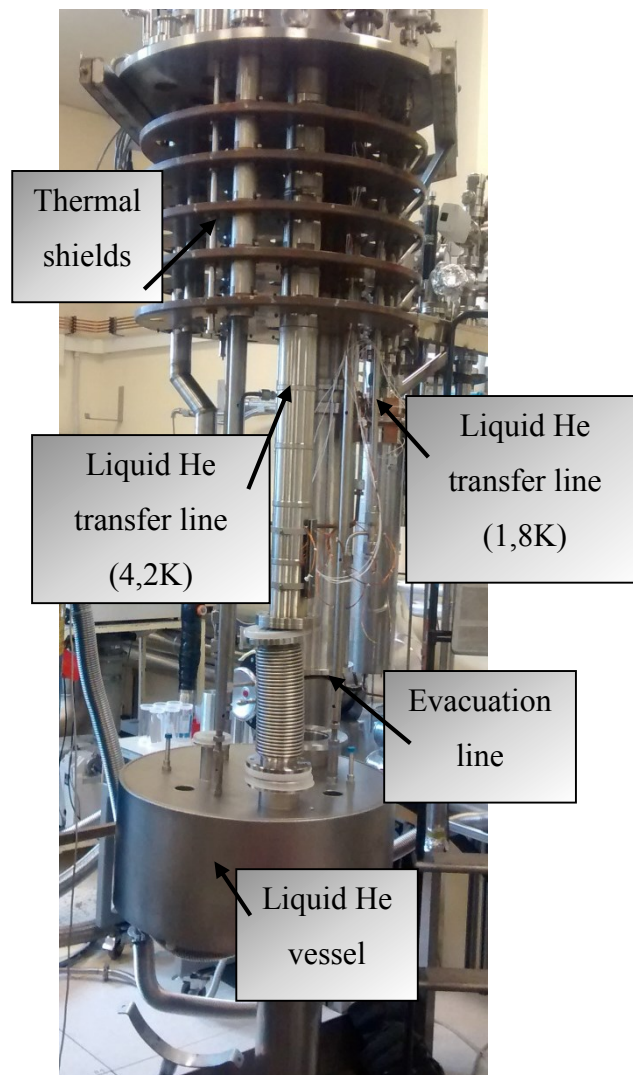
Figure 7.4 Cryostat holder structure during the construction.

A stainless steel flange is the support of the cryostat stand, and it separates the vacuum pressure to atmospheric pressure. Here are located the RF feed through, the thermal feed through, a safety valve, the transfer helium flange, two valves to select the helium pumping to 4,2 or 1,8 K and a valve to connect the pumping system.

A liquid helium supply at 1.8K must be introduced in order to keep the level constant. This task is carried out by a heat exchanger that uses the cooling capacity of the return gas stream to cool down the incoming liquid. The cooled fluid is sent into a liquid/gas separator. The low temperature portion is taken apart by a sintered brass plate in the middle of the separator.

The liquid flows by capillarity action towards the lower side while the gaseous phase remains on the upper part and it is used to refrigerate the copper screen. The stream of liquid is regulated by two valves which can be operated manually from the outside. By changing the pumping speed it is possible to set the evaporation rate and, in turn, the amount of power removed from the dewar. The pressure and thus the temperature, of the bath is regulated by controlling the system pumping speed [15].

The pumping system consist of a rotary pump and a scroll pump to reach the vacuum until $10e^{-2}$ mbar and a turbo molecular pump to reach a base vacuum of $1e^{-6}$ mbar.

On the other hand the RF bunker has a capacity of 400 liters of helium and it consist of two liquid cryogen vessels one to cool using helium and the second one two cool with nitrogen to reduce the consumption of helium. If the aim is to cool the bunker to 77 K, then the nitrogen is the sensible solution, but if it is necessary to cool down to 4 K, then it makes sense to first cool with liquid nitrogen to 77 K and then introduce helium, since nitrogen is about a thousand times cheaper than helium per Joule of latent heat [47].

These cryogen vessels are separated by two vacuum vessels in order to isolate thermally and for low heat transfer at cryogenic temperatures. At these low temperatures the gas molecules are so far apart that convection is virtually eliminated. [49].

Figure 7.5 shows the RF bunker with its respective zones.
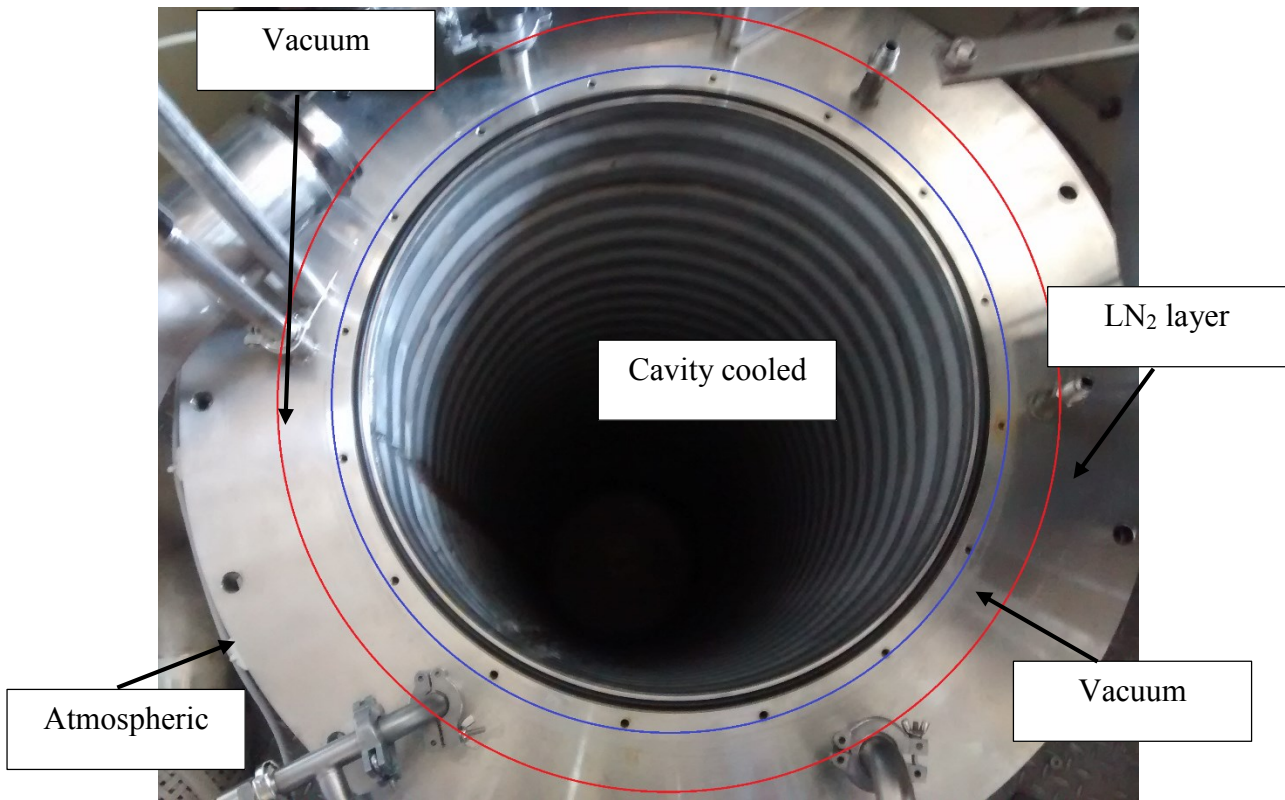
Figure 7.5 Cryostat bunker.

Each zone is equipped with the rotary and turbo molecular pumps, gauges and valves to reach high vacuum pressures.

After the assembling of the cryostat stand the cryostat test was performed following this order:

1. Check the pump line and vacuum.
2. Check the nitrogen line.
3. Check the helium line.

A leak test was performed by the using of a mass spectrometer in order to get a vacuum of $1e^{-6}$ mbar. An exchange gas (nitrogen gas) was introduced during cool-down in the space vacuum layer in order to speed thermalization. The final pressure was $1e^{-7}$ mbar.

7.2 RF generalities and test system

The principles and techniques that will be discussed in this chapter are used to evaluate the overall performance of a cavity, so it is required a specific test to find the effect of certain parameters that can affect the superconducting performance. The most generally used diagnostic techniques is to

measure the response of the cavity to RF fields. The most important figure of merit in evaluating the RF performance is the quality factor (Q0) of the cavity as a function of the electric field.

To excite a resonant mode of the cavity, it is necessary to connect the cavity to an RF source. The power from the RF source is carried to the cavity via a coaxial cable in a specific mode and it is inserted by an antenna called coupler.

The strength of the input coupler is adjusted by changing the penetration of the center conductor. The fixed output coupler is also called a transmitted power probe since it picks up the power transmitted through the cavity [19]. Figure 7.6 shows the coupler and pick up for the QWR cavity.

Figure 7.6. Coupler and pick-up for the quarter wave resonator cavity.

RF test are done inside the cryostat where the cavity is held vertically and ideally these test are performed at or close critical coupling to improve systematic errors and reducing the RF power requirements to a value close to that required for cavity wall losses.

SRF cavities have been in operation for over twenty-five years, and through that time many limitations have been encountered and overcome.

7.3. RF system

The Q measurements and RF processing of superconducting resonator can take advantage of computer-controlled processes and the procedure of measurements is similar for different resonators operating in a wide range of frequencies [15]. Here will be described the system that has been used for the QWR used in ALPI accelerator at LNL, and now for QWR of HIE-ISOLDE type.

Generally a control program carries out the typical procedures related to the cavity measurements in classical VCO-PLL system that allows adjusting and measuring the RF forward power, to find and update the cavity resonant frequency, to calibrate the pick-up signal, to monitor the transmitted power and to adjust the coupler position. The automatic procedure permit also to measure the cavity decay time, to trace the Q- curve and pulse RF conditioning, to calibrate cables and measurement instruments.

The system made by S. Stark [61], consists mainly of a RF signal generator for signals from 100 to 2000 MHz, an oscilloscope, a frequency counter and a DC amplifier, controlled by a PC. This components are communicated with a unique chassis that includes all the other low power RF components. Analog devices components perform the functions of the phase shifter, phase detector and variable gain amplifier. The operating frequency determines the choice of power amplifier. The RF power amplificatory is connected to an external circulator and also to a Narda Directional coupler.

Figure 7.7 shows the measurement system for superconducting cavity testing while Figure 7.8 shows the measurement circuit for cavity characterization.

Figure 7.7. Measurement system for cavity testing [61].
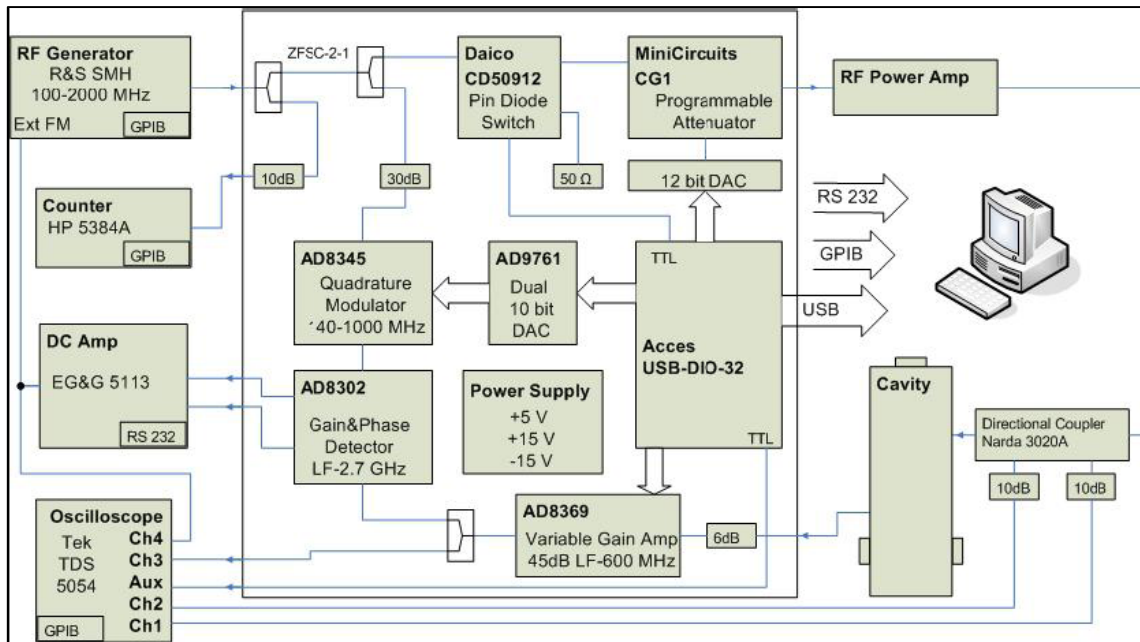
Figure 7.8. Measurement circuit for cavity characterization [61].

7.4. RF measurement

Once evaluated the operation of the cryostat and the RF system the cavity is transported to the cryogenic laboratory to start the measurement. The cryostat stand was took off of the bunker and the cavity was hold to the liquid helium vessel through a stainless steel bellow; then four thermometers were connected on the cavity: two thermometers were connected on the top, one near to the pick-up flange and the last one was connected on the Nb/Cu tuning plate.

Next part of the methodology was focused on the connection of the two antennas. Coupler and pick-up were fixed to the cavity through stainless steel flanges (see Figure 7.9. On the left side the pick-up antenna and on the right side the coupler antenna, both during the mounting.). The coupler rotating system was connected and tested using an automatic controller.

80

Figure 7.9. On the left side the pick-up antenna and on the right side the coupler antenna, both during the mounting.

The cryostat stand was placed into the bunker and the vacuum zones (External volume of the cavity, internal layer and external layer) were pumped using a system of rotary and turbo molecular pumps. The system was pump for 48 hours in order to reach a base vacuum of $1e^{-6}$ mbar.

An infrared lamp was placed inside the internal conductor of the cavity and it was baked for 24 hours at 80°C. Once the cavity was at room temperature, the lamp was took off the cavity to start the cooling of the system.

The precooling starts with the connection of the nitrogen transfer line from the external Dewar to the cryostat LN_2 layer, then the layer was filled for 24 hours. During the precooling it is possible to start with the warm conditioning.

Before the conditioning the power sensor warm calibration and the cables calibration must be done to reduce the thermionic and other noise and hence reduce the error in RF measurement. The calibration is done automatically following the software instructions.

No standard conditioning can be found, each laboratory must develop the optimum procedure and for its coupler and its RF conditions [62].

The conditioning aim is always to "touch" the surface area with RF, "burn" particulates and induce controlled gas layers desorption (they enhance the secondary electron emission coefficient and cause "local desorption outbursts" which could facilitate arcing events) [62].

The conditioning method used in this measurement was the power sweeping, in which the cavity was fed with from 3.2 W with a reflected signal of 45 %, for 8 hours.

To improve the vacuum conditions an exchange gas (He) was inserted into the internal layer. The final pressure was around $1e^{-7}$ mbar.

In order to measure the Quality factor (Q_0) and hence surface resistivity at low temperatures, liquid helium should be added inside the cavity.

Around 500 liters of liquid helium were used to cool the cryostat until 4,2 K Figure 7.10 shows the variation of the temperature during the cryostat cooling.
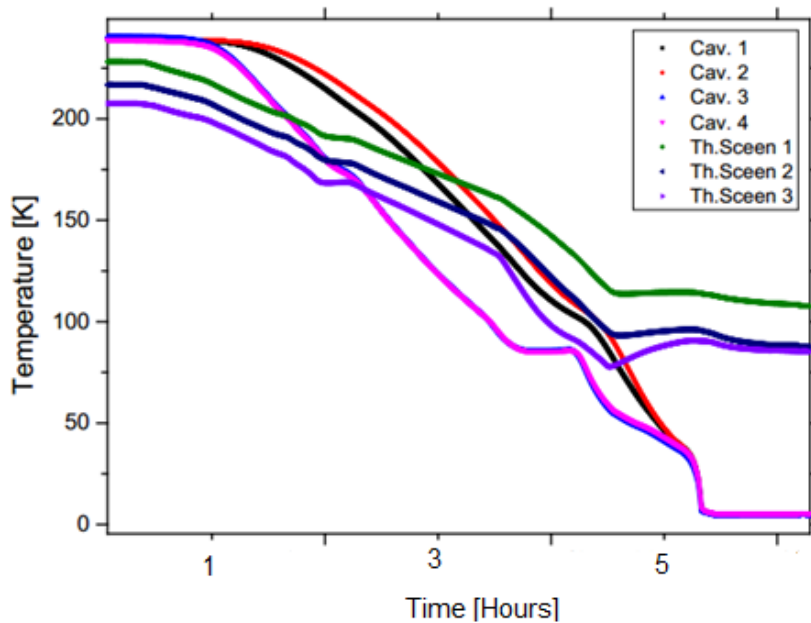
Figure 7.10. Temperature versus time during the cryostat cooling.

After the cooling it was necessary to perform the cool conditioning. The process was carried out for four hours feeding the cavity with 5W. After the cool calibration of the cables, the measure of the Q_0 was started increasing the power to get the Q vs Eacc curve.

Chapter 8.

RESULTS AND ANALYSIS

Here it will be presented the experimental results that have been acquired during the investigation. The first part is focused on the deposition of stainless steel onto quartz samples, testing several configurations of magnetic field. The second part shows depositions of niobium onto quartz samples and the evaluation of the thin film. Finally the deposition of the QWR and its RF performance will be presented in the last part of this chapter.

8.1 Spiral path with plastimag

As was explained before, the magnetic field used to deposit the thin film is produced by the combination of two magnetic paths. A first plasma is generated by plastimag magnets placed on the magnetron structure and the second one, generated by magnets placed on the top of the magnetron structure. The interaction of both plasmas, and eventually plasma holes on the top of the magnetron structure will be analyzed in this part in order to find the best configuration to deposit the QWR.

8.1.1 Stainless steel onto quartz samples/copper strips

The first part of the methodology started testing the magnetic confinement designed at the laboratory of superconductivity but never tested. The configuration presented before can be described as a balanced "braided" confinement, made with plastimag (NdFeB magnets). The magnetic structure was fixed to a motor in order to rotate it and to guarantee the uniform erosion of the cathode during the sputtering process.

To test this magnetic confinement a double wall cathode made of stainless steel has been used and the thin film deposition was performed onto quartz samples, at conditions given in Table 7.

Table 7 Parameters used to perform the Run 1

Run	Sputtering Pressure (mbar)	Power (kW)	Current (A)	Voltage(V)	Time (min)
1	$8e^{-3}$	10	21,5	430	60

A standard procedure was followed to carry out all depositions. The steps are listed below:

- Pumping the vacuum system until it reaches a base vacuum around 10^{-6} mbar.
- Baking the vacuum chamber at 200°C.
- Reach at least $5e^{-7}$ mbar of vacuum before the deposition.
- Set the turbo molecular pump on stand-by position.
- Connect the power supply to the cathode.
- Close the leak valve.
- Open the Argon line and subsequently open the leak valve until the desired gas pressure.
- Open the water line.
- Turn on the rotating system.
- Turn on the power supply and set it until the desired power.

After performing the deposition, the thicknesses were measured using the profilometer. The thicknesses were plotted as a function of the position of the samples as is shown below.
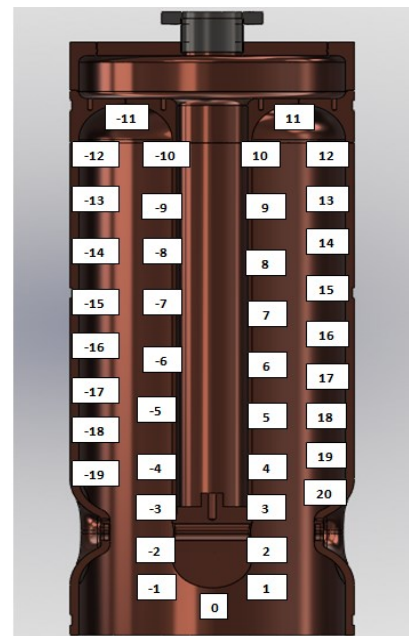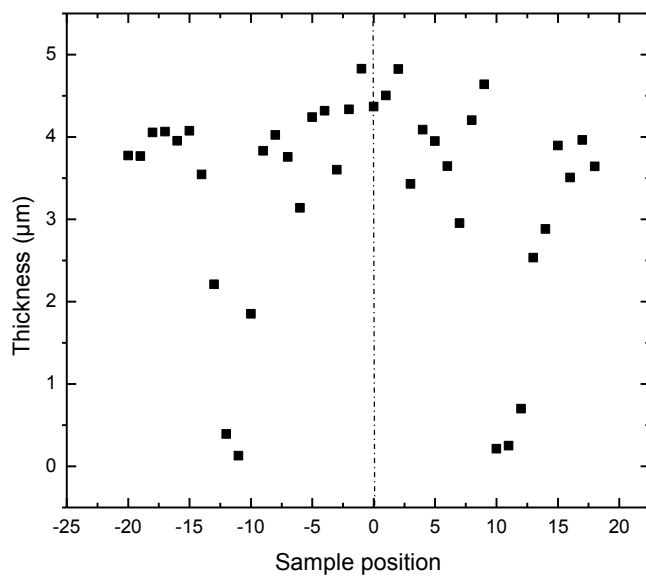
Figure 8.1 Deposition 1.Thickness vs sample position of stainless steel onto quartz samples.

Observing Figure 8.1, there are differences along the cavity profile. Higher values of thicknesses were found close to the inner conductor between positions -9 and 9 and lower values of

thicknesses were found on the top of the cavity where the deposition rate is around 1Å/s. The difference of thickness between the inner and external conductor may occur because the magnetron is closer to the central electrode. A good uniformity along the QWR cavity is difficult to obtain due to its complex shape [33]. However, previous studies based on the depositions of QWR showed that it is possible to increase the deposition rate during the sputtering process changing the deposition parameters, decreasing the distance between the cathode and the substrate or changing the magnetic confinement [33].

In order to study the continuity of the plasma along the cavity during the deposition, copper strips were placed inside the cavity and a further deposition was performed keeping the same magnetic confinement and the same parameters shown in Table 7. Then, the stripping test was performed to remove the stainless steel film. The results are shown below.

Figure 8.2 Copper strips deposited in RUN 1. a) Before and b, c) After stripping test.

Figure 8.2 confirms the previous results, there is an absence of plasma on the top of the cavity. The coating is gradually dissolved in the acid solution as a function of time. This means that the area where the coating is first dissolved, has finest thickness due to the fact that the action of the magnetic field is not uniform.

In addition, a viewport was placed on the top of the chamber to see the plasma during the deposition; with a reduced length cathode made of stainless steel it was possible to study several magnetic confinements in order to find the best combination to perform the next deposition. All configuration tested are presented in Table 8.

Table 8 Magnetic confinement tested in order to study the plasma on the top of the cavity

Magnetic confinement	Plasma	Observations
A: Spiral confinement without magnets on the top		Plasma hole
B: Spiral confinement without magnets on the top. Reducing the length of the spiral		Plasma hole still present
C: Spiral confinement + plastimag horseshoe		Smaller plasma hole
D: Spiral confinement+ Plastimag horseshoe + rectangular permanent magnets		Higher plasma density with plasma hole
E: Spiral confinement+ Reduced lengh plastimag curve		Low plasma density on the top
F: Spiral confinement + plastimag curves		Low plasma density on the top
G: Spiral confinement+ cylindrical permanent magnets		High plasma density on the top
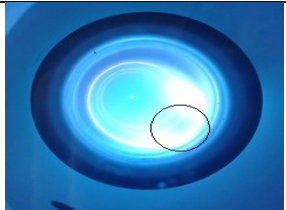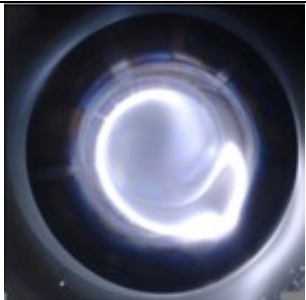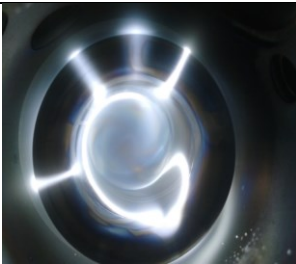
In this table it is possible to see the first magnetic confinement called **A**, where it was observed a plasma hole during the sputtering process. The absence of magnetic field was evidenced; it means that the magnetic field is weak in certain zones, therefore a deposit made with this configuration would have considerable thickness differences along the cavity.

A new test was done, reducing the length of the magnetron body and placing a base plate on the bottom, to build the configuration **B**. The spiral should be in a higher position and consequently the plasma density should be increased. In Table 8 is noted that the plasma hole is still present.

In order to increase the plasma on the top of the cavity, it was decided to perform further tests to study the interaction of the plasma generated by the magnetron body and a second plasma generated by a smaller magnetic path placed on the top. These tests were performed using a reduced length cathode, just built in order to explore different magnetic confinements on the top of the cathode. Several simulations were analyzed to study the interaction between the magnetic spiral oriented to the top of the chamber and some configuration of magnets placed over the magnetron body. The 2D simulations are presented in appendix A.

In parallel, several magnetic confinements were tested in the reduced length cathode. The configuration **C** was built by placing a stainless steel curve, denominated "horseshoe" covered with plastimag; that is a NdFeB material with a magnetization of 3800 G. The horseshoe was placed on the top of the magnetron body, opposed to the spiral, as is shown in Figure 8.3.

Figure 8.3. Construction of the C magnetic configuration

After observing Table 8, it is possible to note an increment of the argon plasma on the top of the cathode respect to the simple spiral configuration, however the field is not enough to close the entirely hole. For this reason it was decided to increment the magnetic field, adding magnets on the

surface of the horseshoe. Several configurations were tested in order to find the best combination to improve the plasma. Some of the configurations are shown in next figure.
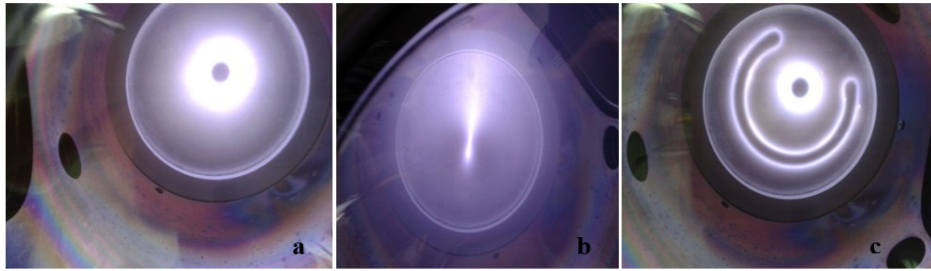
Figure 8.4. Argon plasma generated by: a) NdFeB cylindrical magnet in vertical position, b) NdFeB cylindrical magnet in horizontal position, c) Curve with plastimag and NdFeB cylindrical magnet in vertical position.

Based on this figure; the strong plasma is generated by the circular magnet placed in vertical position, however the dimension of this magnet is not compatible with the dimensions of the cathode. The solution was focused on the increment of the plastimag curve, as is shown in next figure.

Figure 8.5 D top magnetic configuration.

Table 8 shows the argon plasma generated by configuration **D** (rectangular magnets placed over the horseshoe structure). It is evident the increment on the plasma, the interaction between the plastimag horseshoe and the rectangular magnets creates a much stronger plasma as is required, but it was necessary to study the interaction of the spiral with the top configuration.

The horseshoe curve was placed on the top of the magnetron body, oriented as before in the opposite part of the spiral to avoid a repulsion between the magnetic field lines from both confinements. The argon plasma is presented in Table 8.

Unfortunately, the plasma hole is still present, probably the curve area in which are placed the magnets is too big and there is interference between the field generated by the spiral and the field generates by the horseshoe. A possible solution to this problem is to replace the curve structure with shorter curves that allow to see the interaction of the magnetic field lines. However, the field is not necessarily as strong as before, because the amount of magnetic material used (plastimag) is lower.

Several configurations were tested in order to replace the horseshoe configuration with a stronger magnetic confinement. The results are given in the following figure.

Figure 8.6. Argon plasma produced by different top magnetic confinement. Configurations differs in the amount of magnetic material used.

Figure 8.6 shows the argon plasma produced by four magnetic confinements. Figure 8.6.a, produces the weakest plasma. In this configuration it has been used two turns of magnetic material. By the other hand, the stronger plasma was produced by the last configuration (Figure 8.6.d), in which it has been used six turns of magnetic material (Plastimag). Based on these results it has been placed a six turns magnet, referred as "**E** confinement", on the top of the magnetron body, to analyze the interaction with the spiral. The result is shown in Table 8.

Observing Table 8 the magnetic confinement could be used because no contact occurs between the magnetic field lines. However, it may not be strong enough to increase the deposition rate on the top of the cavity.

Another magnetic confinement was tested (configuration **F**), changing the orientation of the plastimag. Table 8 shows the argon plasma in function of the amount of magnetic material used (number of turns).
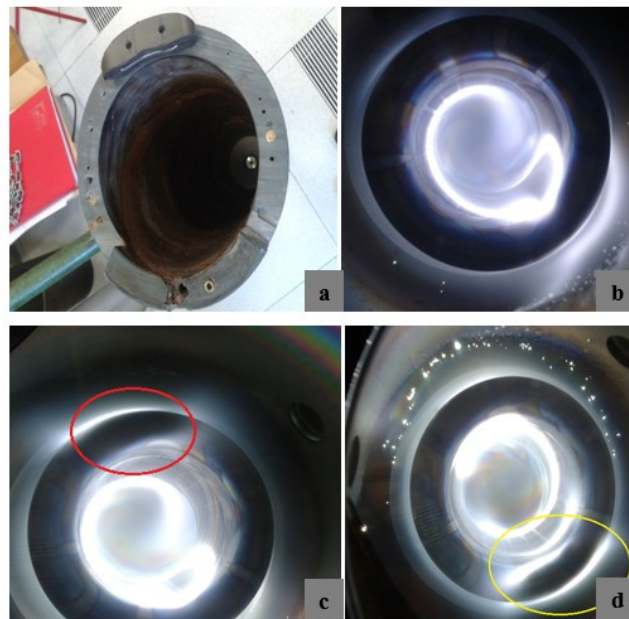
Figure 8.7. a) F Magnetic confinement, b, c, d) argon plasma generated by fourth magnetic confinement.

The set of figures shows the argon plasma produced by the fourth magnetic confinement. In table 8 is shown the top configuration created with four turns of magnetic material (plastimag) oriented vertically over the magnetron body. The plasma was turned on, but no evidence of the top configuration was observed. Increasing the number of turns the plasma is stronger, as it is evident in Figure 8.7 b and Figure 8.7 c, with 8 and 10 turns respectively; however it is weaker in comparison with the magnet oriented horizontally, as was presented previously.

A new magnetic confinement called **G** was tested. It consists in three cylindrical magnets of 5 cm length and 2cm diameter placed at 20 cm of distance. The results can be seen in Table 8, where there is a stronger plasma in comparison with previous confinement. The interaction between the spiral and the cylindrical magnets is good, with well-defined magnetic field lines. The **G** magnetic confinement was used to perform the next deposition. The parameters used are shown in Table 9.

Table 9 Parameters used to perform the Run 2.

Run	Sputtering Pressure (mbar)	Base Vacuum(mbar)	Power (kW)	Current (A)	Voltage(V)	Time (min)
2	$8e^{-3}$	$3e^{-7}$	10	22	450	30
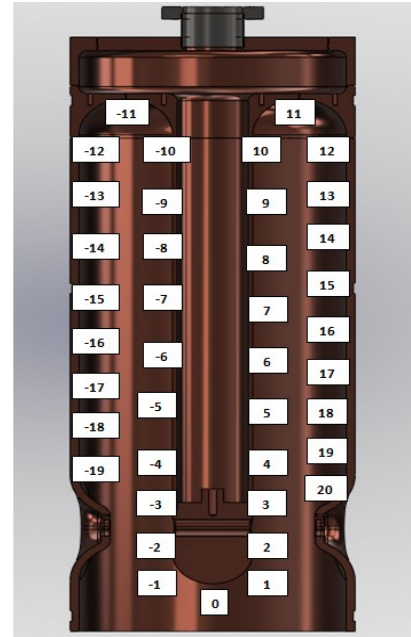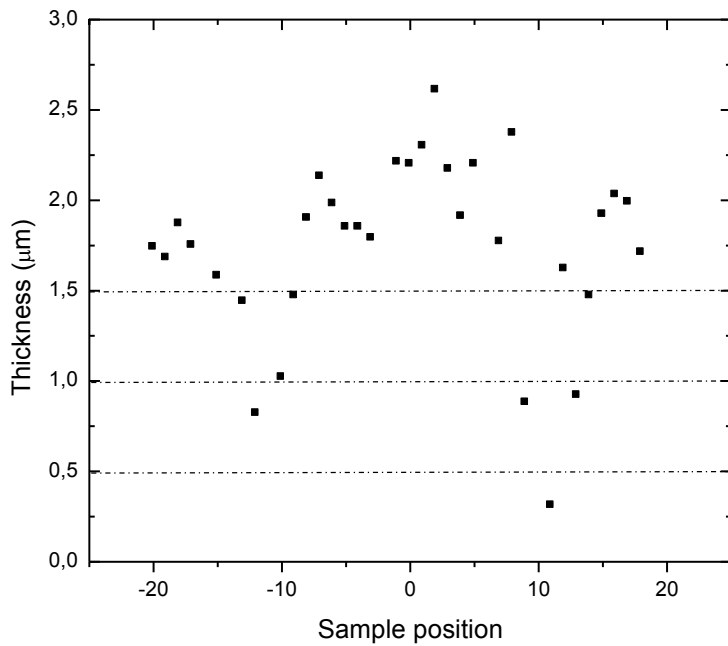
Figure 8.8. Deposition 2.Thickness vs sample position of stainless steel onto quartz samples.

In previous deposition it was placed the spiral with the crown of magnets and the thickness was 0, 2 μm on the top of the cavity, in 60 min of sputtering process. In this deposition the thickness was 0, 3 μm on the top of the cavity, setting the same parameters of process. The magnetic field hole is not present in positions ±10 and ± 12, as before. Also the stripping test was performed in order to locate the position of the magnetic field hole. The results are shown in Figure 8.9.
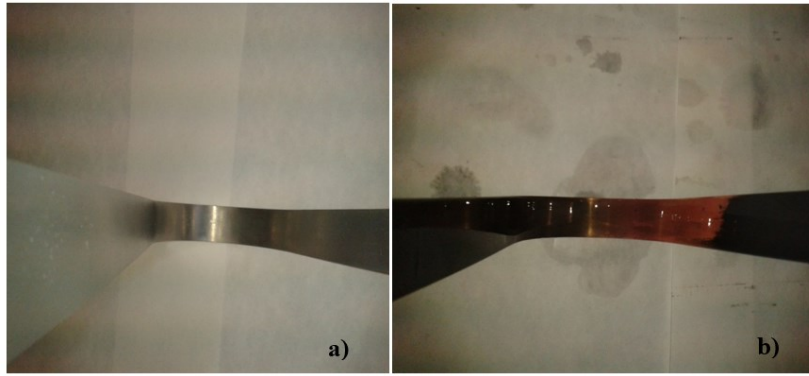
Figure 8.9. Copper strips deposited in RUN 2. a) Before and b) After stripping test.

After two hours changes on the surface were observed. The hole of magnetic field is still present, however it is smaller in comparison with the previous deposition. Due to the strong plasma generated by the cylindrical magnets the plasma has been improved, the results of stripping test are correlated with thickness measurements in which the thickness at the top of the cavity has been increased. It is necessary to intensify plasma whereby one more cylindrical magnet was placed over the magnetron body. The deposition was carried out with the same parameters used during the last deposition and the base vacuum during the deposition was $4e^{-7}$ mbar. The thickness in function of the sample position is presented in Figure 8.10, while Figure 8.11 shows the stripping test results.
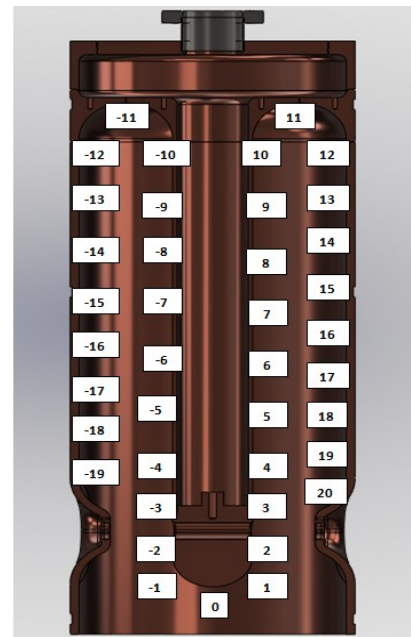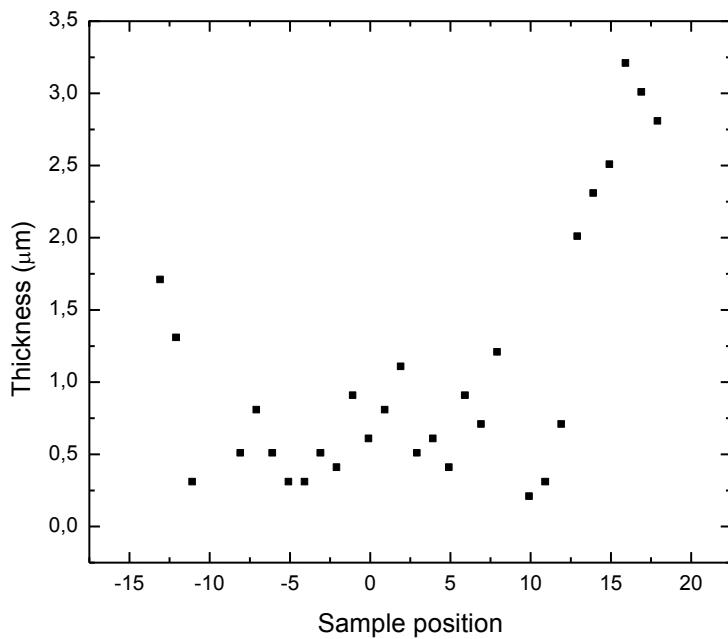
Figure 8.10. Deposition 3.Thickness vs sample position of stainless steel onto quartz samples.

Figure 8.11. Copper strips deposited in RUN 3,a) before and b, c) after stripping test.

Based on the last figures, the thickness in not uniform along the cavity; values of thickness are lower in comparison with the previous deposition. Also the stripping test was performed. There are 3 zones where the thickness is lower than 0, 5 µm. Most of the thickness values are less than 1 µm. Two separate plasmas cause problems. One possible explanation of this behavior is that magnets can be turned on at certain pressure ranges. Possibly not all magnets turn on used at the same pressure, therefore a new deposition is performed while keeping the same magnetic confinement but performing the sputtering process at a higher pressure. It was decided to use a pressure of $1e^{-2}$ mbar. The results are the following.
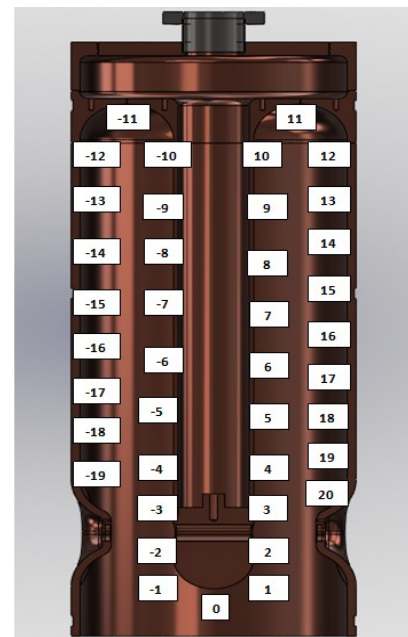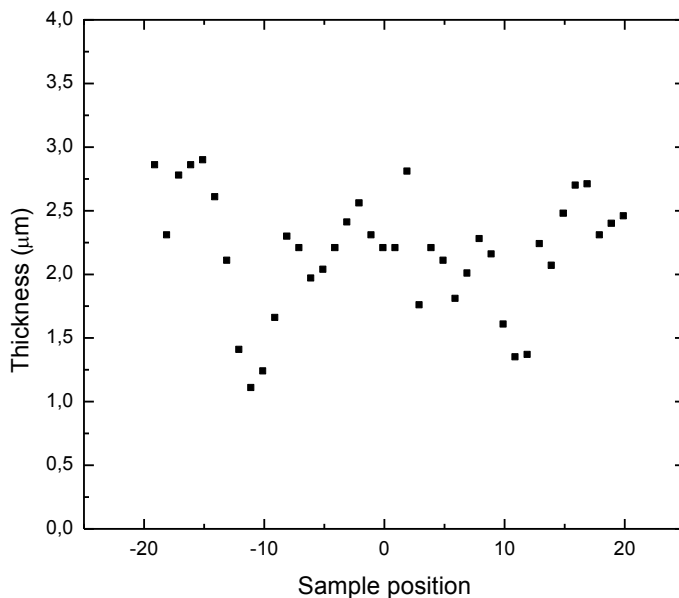
Figure 8.12. Deposition 4.Thickness vs sample position of stainless steel onto quartz samples.

Observing Figure 8.12, it is evident an improvement on the uniformity of the film; also the thickness on the top of the cavity has been increased with values higher than 1 μm. The setup achieved high sputtering rates (above 10 Å/s), and a reasonable thickness homogeneity (2±1) μm. The working pressure was $1e^{-2}$ mbar, increasing the argon pressure improved the thickness homogeneity along the cavity. This deposition allowed selecting a suitable range of sputtering parameters.

The stripping test was performed and the coating was removed more or less uniformly, except on zones where the thickness film is lower. After one hour evident differences on the top of the cavity can be noticed; however the film was removed uniformly after 2 hours. Stripping test results are shown in the following figure.
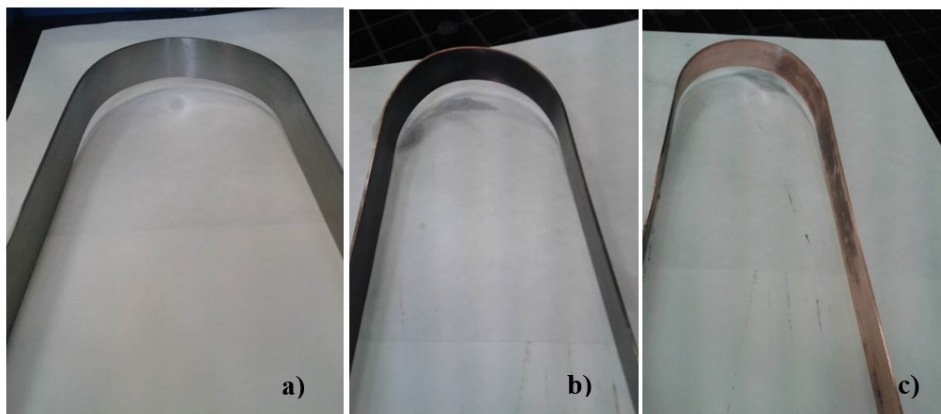
Figure 8.13. Copper strips deposited in RUN 4,a) Before and b, c) After stripping test.

Last result has proven the feasibility to use the magnetron sputtering technique and the magnetic confinement proposal to deposit a uniform thin film onto quarter wave resonator cavities. However, a last deposition of stainless steel onto quartz samples was performed, adding one more cylindrical magnet to the top of the magnetron body. The deposition parameters are presented in the table below.

Table 10 Parameters used to perform the Run 5.

Run	Sputtering Pressure (mbar)	Base vacuum (mbar)	Power (kW)	Current (A)	Voltage(V)	Time (min)
5	$1e^{-2}$	$2e^{-7}$	10	23	415	30

The thickness in function of the sample position is presented in Figure 8.14.
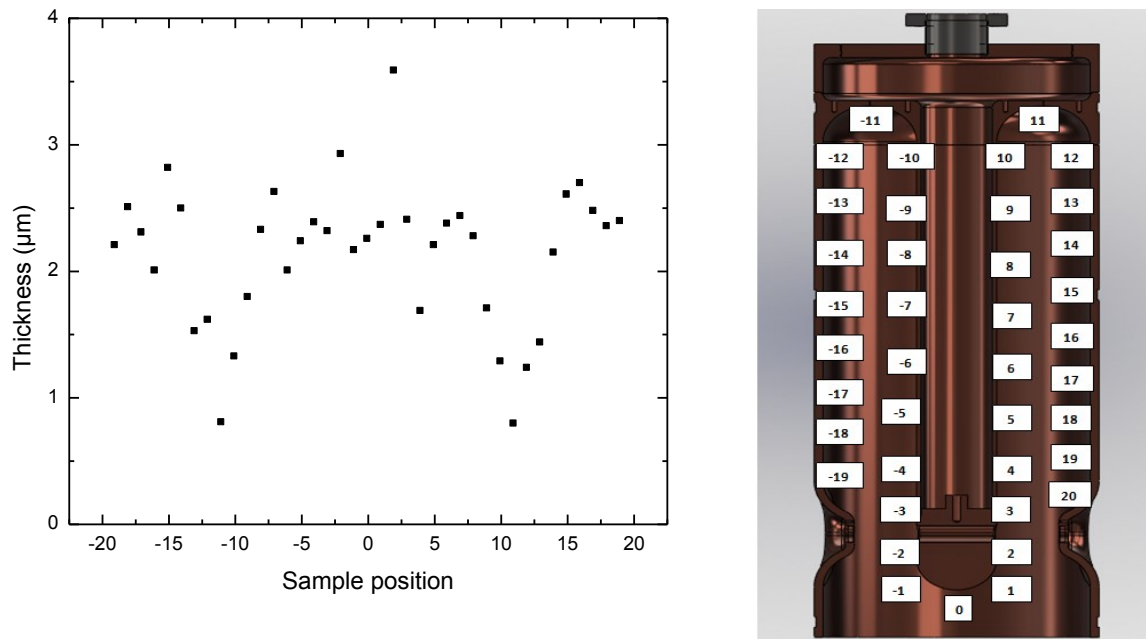
Figure 8.14. Deposition 5.Thickness vs sample position of stainless steel onto quartz samples.

Although the magnetic charge is higher, the uniformity of the cavity is not good. The thickness in critical zones, as on the top of the cavity, is lower compared to the previous deposition, and there are also points out of range as is noted in position (-2) in the central tube of the cavity. Based on this, it was decided that the best conditions of both magnetic fields and parameters are those of the fourth deposition. Henceforth, the research will be focused not only on the uniformity of the thin film, but on the niobium properties. Stainless steel depositions have been a starting point to set the appropriate parameters during the sputtering process and also to find the best configuration of magnetic field but here it was decided to stop the stainless steel test and work with niobium.

8.1.2 Niobium onto quartz samples

A double wall cathode made of niobium was built in order to deposit the thin film onto quartz samples and also to analyze its properties. To avoid contamination of niobium the vacuum chamber and the QWR cavity were cleaned using a process of abrasive blasting.

The vacuum system was assembled again .Then the system was baked for 10 hours in order to outgas the chamber. After the baking it was performed the cleaning of the cathode without any substrate, by the sputtering discharge in order to eliminate the surface impurities on the niobium.

Niobium thin films were sputtered onto quartz samples in order to measure the thickness and the superconducting properties (T_c and RRR). The parameters used on the first deposition are presented below.

Table 11 Parameters used to perform Run 1 of niobium onto quartz samples.

Run	Sputtering Pressure (mbar)	Base Vacuum (mbar)	Power (kW)	Current (A)	Voltage(V)	Time (min)
1	1e $^{-2}$	1e^{-7}	3	10	300	30

Because long periods are required for T_c and RRR measurement, and also because of the isometric shape of the QWR, only six samples were characterized. The thickness in function of the samples position are presented in Figure 8.15
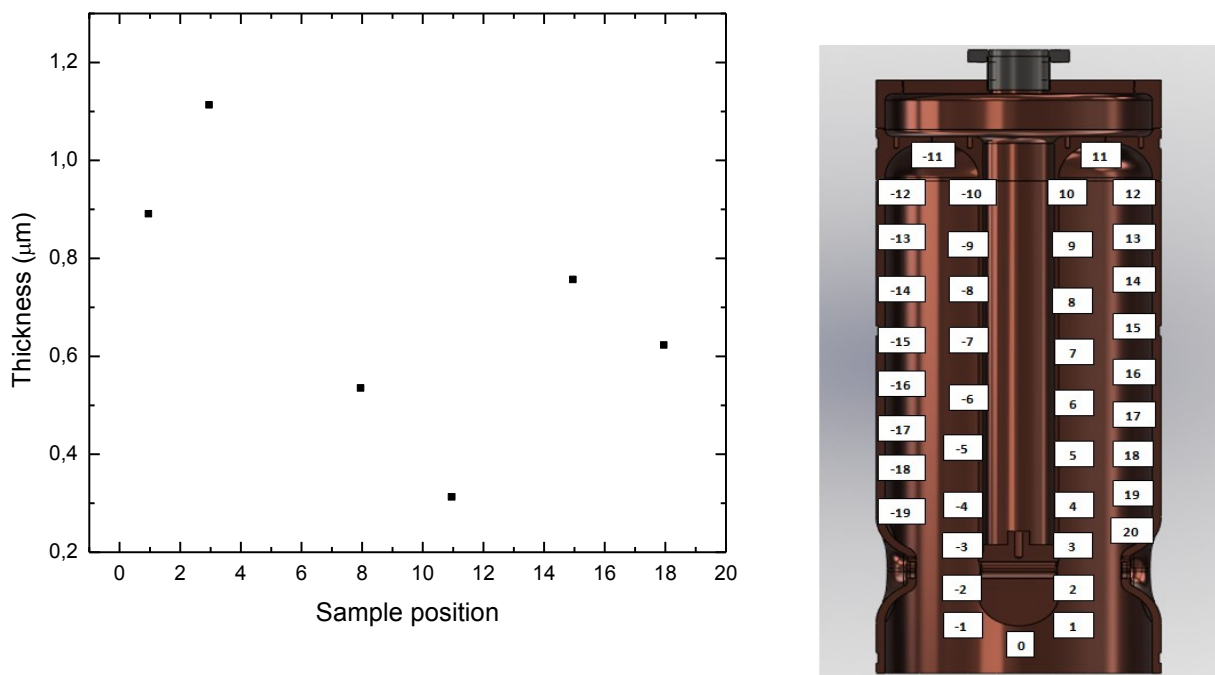
Figure 8.15. Deposition 1.Thickness vs sample position of niobium onto quartz samples

Up to this point it has been used a stainless steel cathode that allows understanding the appropriate parameters to deposit the film on the QWR. This experience has been taken into account to deposit the niobium thin film. It has been decided to work at low power and then to increase it in order to analyze the thin film properties. As is shown in Figure 8.15, the thickness is lower than previous depositions; there is a direct relationship between the power and the deposition rate during

the sputtering process. Increasing the power increases the deposition rate at certain pressures. The sputtering chamber pressure is inter-linked to the sputtering power. For low sputtering power, a high chamber pressure reduces the energy of the sputtered atoms and covers the substrate with charged particles [63].

In addition, the sputtering current and voltage play important roles in ionizing the plasma discharge. The deposition rate increases with an increase in current, which is the flow of ionized particles. The deposition rate increases slowly with an increase in the energy of the ionized particles, which is due to the potential difference or voltage [63]. Moreover, there is the effect of the distance from target and substrate. Because there are small differences on the niobium cathode design respect to the stainless steel cathode, probably has been modified the distance between the top of the cathode and the top of the cavity. It can be the explanation of the lower values of thickness on the top of the QWR.

Reducing the target-to-substrate distance (often called throw distance) is a simple, direct way to increase deposition rate [65]. By the other hand, residual resistivity ratio in function of the thickness is presented in the following figure.
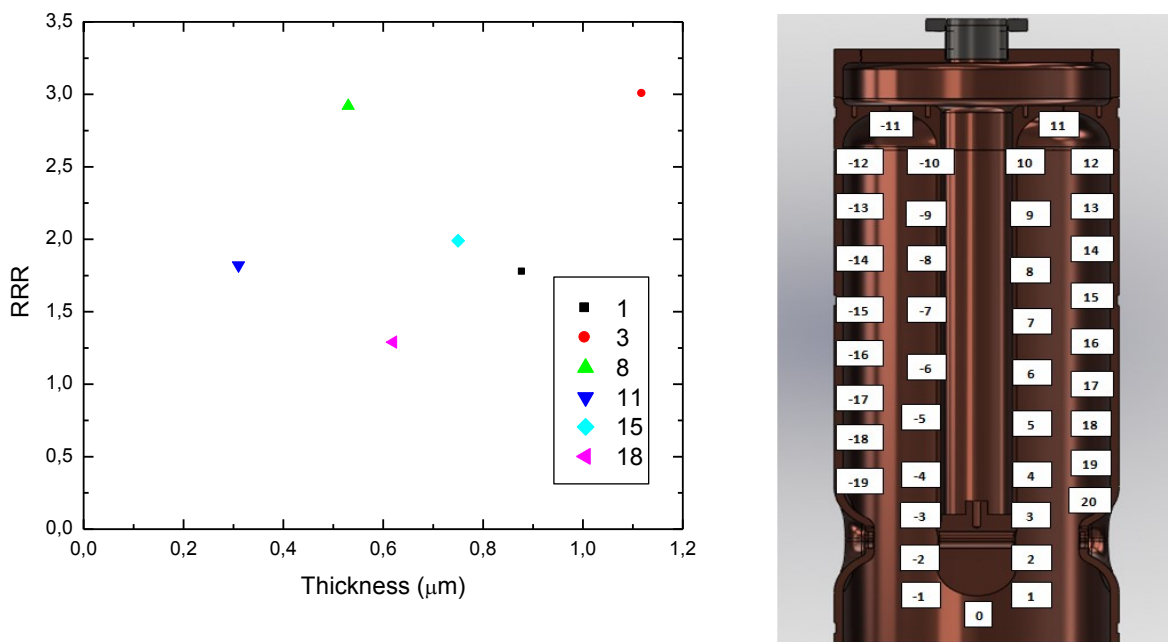
Figure 8.16.First niobium deposition. Residual Resistivity Ratio in function of the thickness for quartz samples placed in different positions along the cavity.

98

RRR values are too low, the maximum value is 3 for the sample number 3, which is the sample with the higher thickness. It is required at least a RRR value of 30, however a RRR value > 15 could be acceptable to have an admissible film. Some features are related to the film thickness. The RRR depends on the film thickness which mainly due to the grain size growing. The topography of thick films commonly become rougher with the grain size increasing that result in larger RF surface resistance.

However, thick films usually possess high stress that should be avoided in superconducting cavities. This behavior is because the temperature variation of the cavities is several hundred centigrade from sputter depositions to cryogenic applications. Thermal stress, if big enough, could cause the niobium films strip off from the wall of copper cavities.

Thickness of sputtered niobium films cannot be too thin as well, because the penetration depth is 30-40 nm for niobium and the superconducting state can be damaged with the penetration of RF currents and flows inside the normal conducting copper. In addition, niobium thin films often have not an integrity crystalline structure and they have many impurities such as oxygen and carbon.

Generally, niobium films sputtering coated on SRF cavities are no less than 1 μm in thickness, and the maximum thickness is around 4 μm.

The gettering effect of the sputtering deposited niobium films is another factor although of minor importance. Sputtered niobium films will getter ambient gas atoms, as more impurity gas atoms buried in sputtered films, surroundings become cleaner and following sputter will get more pure films. But if too much impurity buried in the interface of the copper substrate and the deposited niobium film, cryogenic properties of the cavity will be poor [65].

For this reasons the thickness results agree with the residual resistivity ratio results; it is possible that increasing the thickness the RRR will increased too.

On the other hand the lowest value of critical temperature (7,05K) was found at the top of the cavity in position 11, while the highest value was found in position 3 (8,85K). The transition of the sample placed in the 3rd position is shown in Figure 8.17
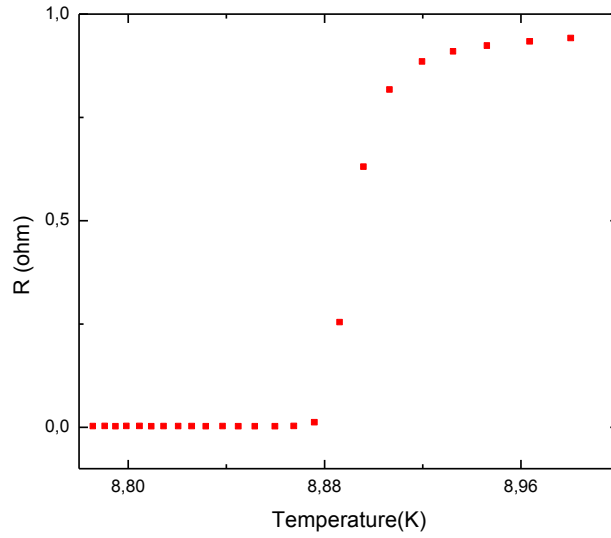
Figure 8.17.Superconducting transition of sample placed in position 3 of the QWR.

This is a poor result and is closely related to the BCS resistance, because losses depend exponentially from the critical temperature, If the T_c decrease the R_{BCS} will increase, as is shown in next equation.

$$R_{BCS} = \frac{A}{T} e^{\frac{-S\,Tc}{2T}} \tag{8.1}$$

The superconducting transition width is larger than for niobium bulk, in this case 0,1K. Generally ΔT_c is<0.02K for a bulk Nb. Lower T_c values are frequently correlated to the film morphology and to the impurity content. Depending of the substrate temperature, water and oxygen present in the vacuum or in the sputter gas may stick to those boundaries yielding smaller grain size and reducing T_c values. When sputtered with sufficiently clean gas, the grain boundaries between the columns stay fairy clean, because O and H desorb preferentially by plasma impact via electronic radiation damage [66] [67]. All samples of this run have critical temperatures lower than 8,85K, therefore it will be necessary to find the parameters to decrease the number of impurities, in which the starting point could be the increment of the substrate temperature.

In order to study the influence of the distance between the cathode and the cavity, the cavity holder was modified. The new distance is 5mm shorter. By the other hand the influence of the temperature was studied, placing an infrared lamp inside the central shaft of the stainless steel dummy cavity as is shown in Figure 8.18.

Figure 8.18. IR lamp placed inside the central electrode of the QWR

A new deposition was performed, keeping the same parameters of sputtering (3kW for 20 min with intervals of time of 5min). Moreover, the cavity was heated at 150°C during the sputtering process. The base vacuum reached was 1,98e^{-7}mbar. Figure 8.19 shows the thickness against the sample position.
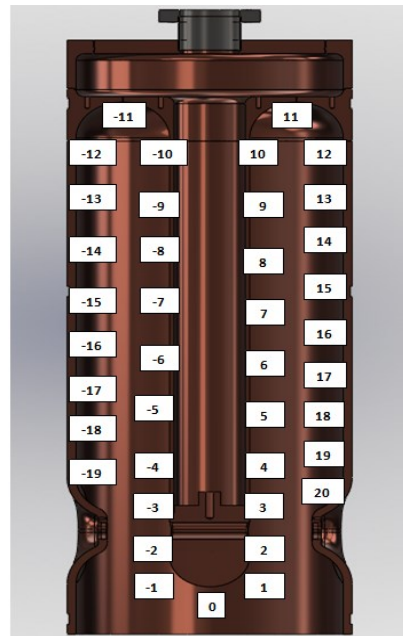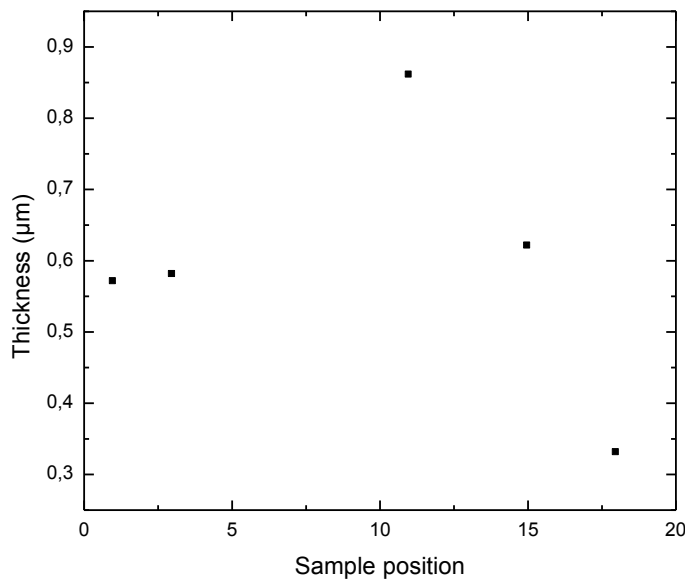
Figure 8.19. Deposition 2.Thickness vs sample position of niobium onto quartz samples.

Observing Figure 8.19, the thickness values are lower respect previous deposition. The thickness was increased only in one position that corresponds with the position on the top of the

cavity. This increment is caused probably because of the distance between the top of the cathode and the top of the cavity, evidently it has been increased the deposition rate in this zone. On the other hand, the following figure shows the RRR against the thickness for the quartz samples. In this case the sample placed on the top of the cavity (position number 11) has the lowest RRR value, even if it has the highest thickness. Probably the effect of temperature plays an important role in the RRR, sample number 3 located on the central electrode has the highest value of RRR. The RRR of niobium increases with the coating temperature since the higher surface mobility during the coating contributes to reduce lattice defects and impurities content like argon [68].
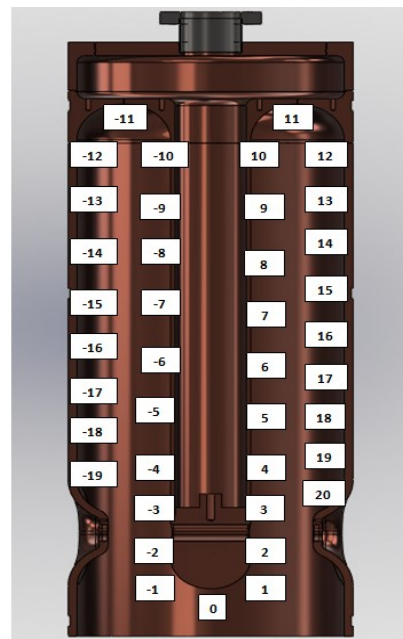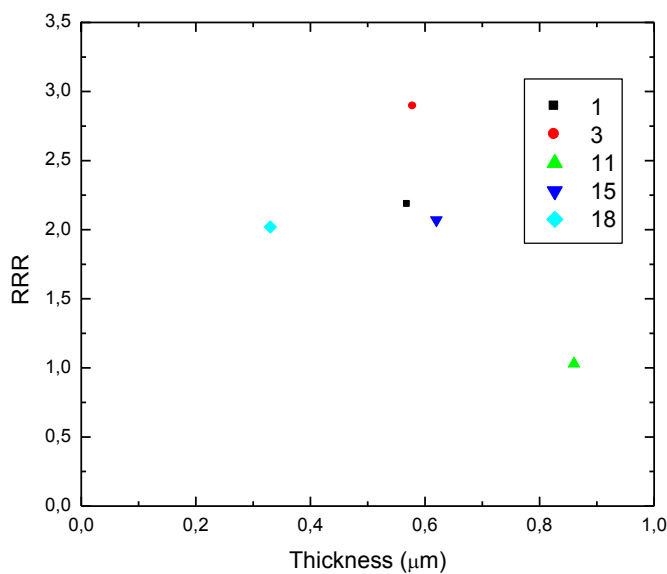
Figure 8.20. Second niobium deposition. Residual Resistivity Ratio in function of the thickness for quartz samples placed in different positions along the cavity.

In order to observe the morphology of the niobium, the samples have been analyzed with a SEM microscope at the inner and the external conductor and at the top of the resonator. Next figure shows the cross section of the cavity and the photomicrographs in the respective zones.
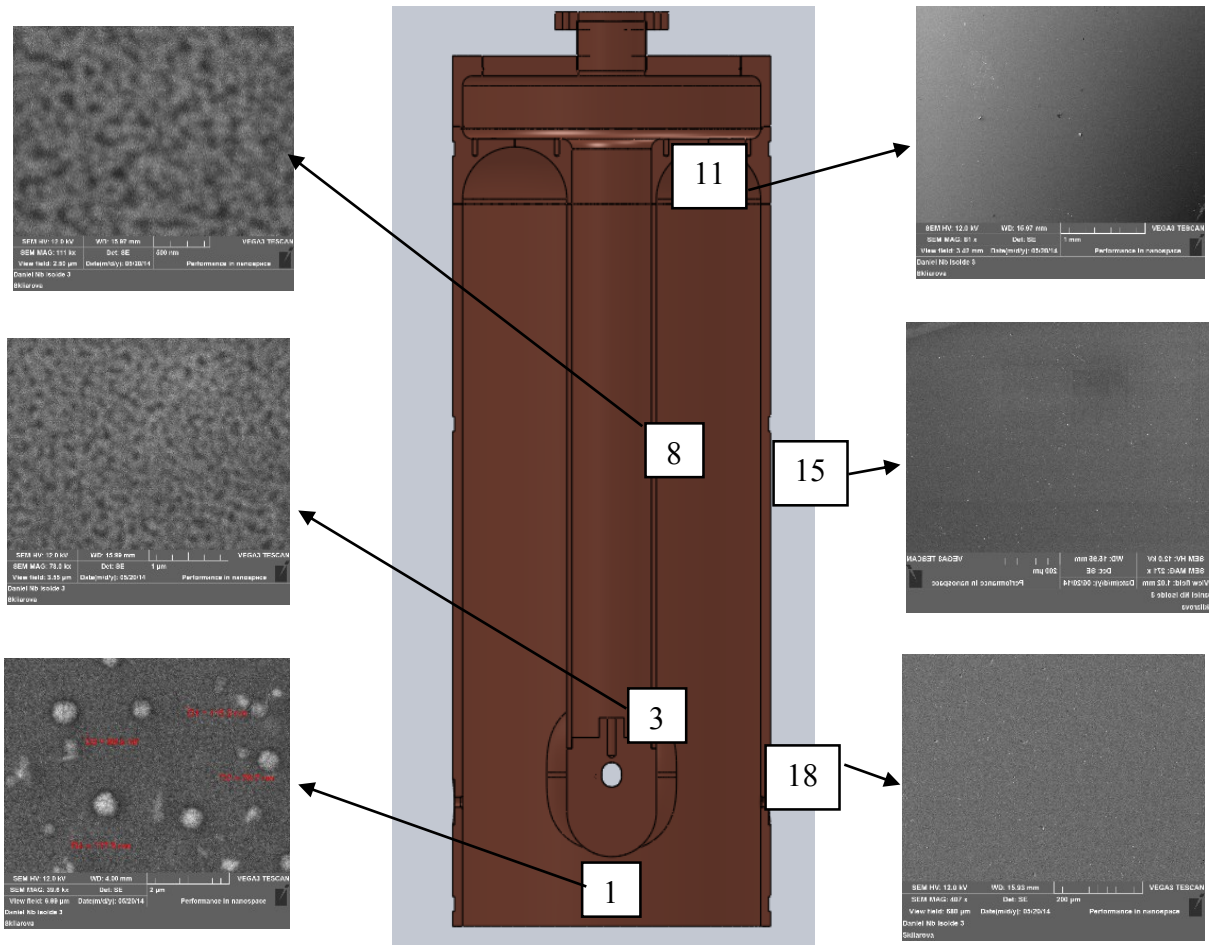
Figure 8.21. Morphology of the niobium samples sputtered at 3Kw for 30 min.

If the niobium films are sufficiently pure and ordered, cavities will show good RF performance. It is well known that a good microstructure is required with well-connected grains and absence of voids [69]. From the SEM photomicrographs, it can be observed that there are differences on the microstructure along the cavity, it was possible to measure the grain size only close to the inner conductor, where the average grain size was around 90 nm. On the top of the cavity and along the external conductor it is possible that the grain size was lower. This differences can be attributed to a non-uniform heating during the sputtering process. Samples placed at the internal conductor are closer to the magnetron and therefore the substrate temperature is higher. In addition the internal samples were heated by an IR lamp placed inside the inner electrode. Due to the small grain size , high sputtered gas content and some oxygen content of the films, the mean free path of the sputtered niobium layer should be lower than 30-60nm, but this grain size value could be correlated with RRR of 10-20. In this case it is possible to correlate the RRR values with a high impurities content [67].

A new deposition was carried out increasing the power of the sputtering process, the parameters are presented below.

Table 12 Parameters used to perform the Run 3 of niobium onto quartz samples.

Run	Sputtering Pressure (mbar)	Base vacuum (mbar)	Power (kW)	Current (A)	Voltage(V)	Time (min)	Heating °C
3	1e $^{-2}$	1e^{-7}	5	17	280	30	150

Thicknesses against sample positions are shown in Figure 8.22
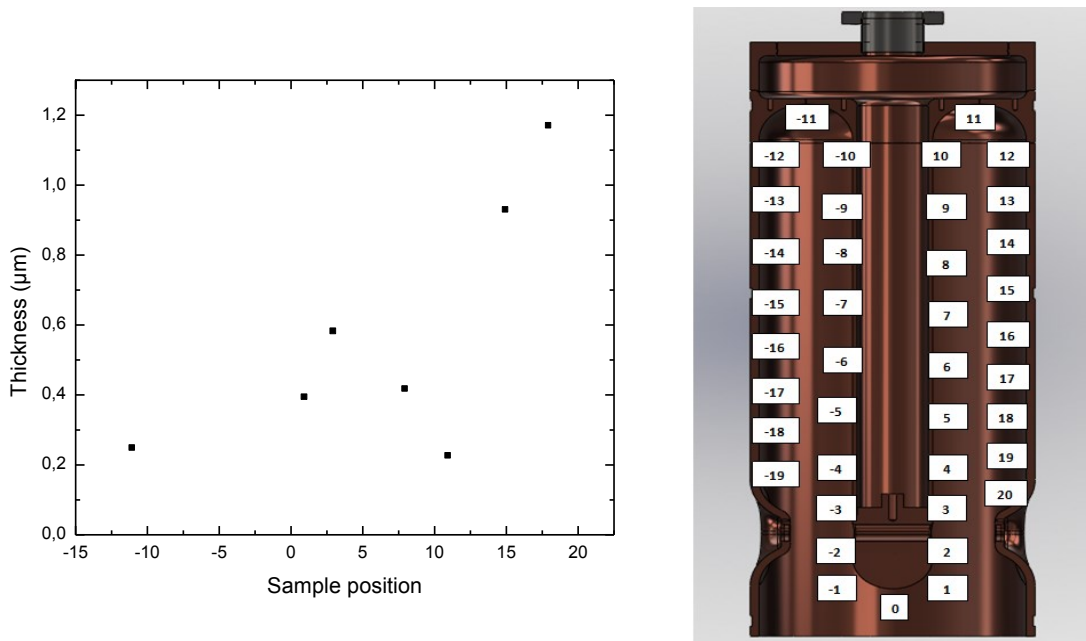
Figure 8.22. Deposition 3.Thickness vs sample position of niobium onto quartz samples.

After seen Figure 8.22, there are not notable improvements on the thickness. The thickness was increased only in the external conductor (represented for samples 15 and 18). The uniformity along the cell is not good, the lowest value is 0, 22 μm on the top of the cavity and the highest value is over 1μm on the external conductor. Following results report the influence of increasing the power in the RRR.

104
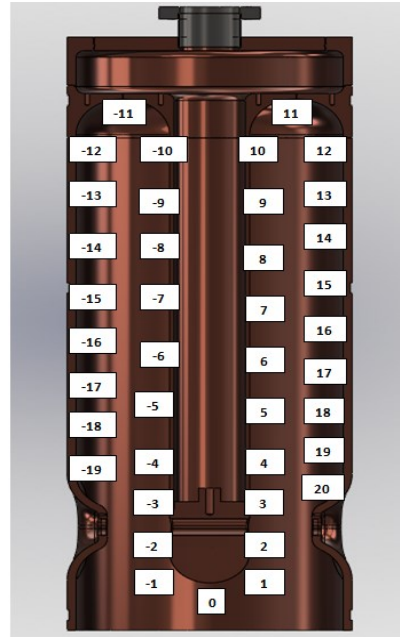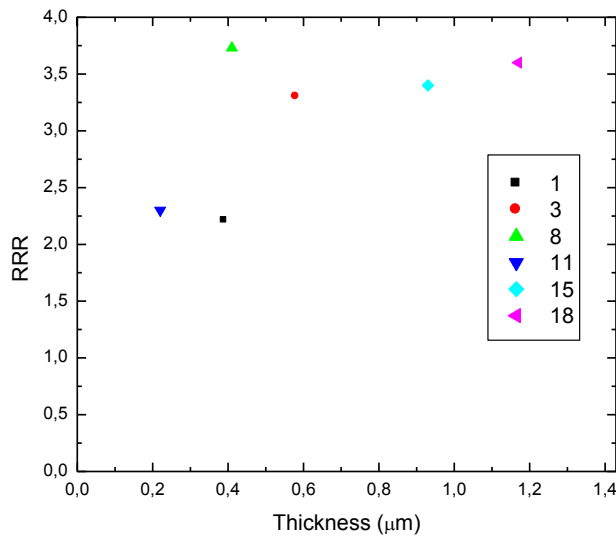
Figure 8.23. Third niobium deposition. Residual Resistivity Ratio in function of the thickness for quartz samples placed in different positions along the cavity.

Respect to Figure 8.23, RRR are higher respect previous depositions. Sample 8 located in the internal conductor has the highest RRR value (3, 73), even if the thickness is quite small (0,41 µm). In this case it is evident that temperature increasing has a greater effect on the resistance. Samples placed closer to the infrared lamp and the magnetron should be heated more.

Also it is notable the continuous improvement of the RRR with the increment of the power during the sputtering process. Probably as was explained before the coating temperature affects the surface mobility during the coating and contributes to reduce the defects and impurities [68].

The following table presents the parameters used to perform four more depositions in which it is highlighted the increment of the sputtering power. The results will be compared taking into account one fix position in order to understand the influence of each parameter on the film properties.

105

Table 13 Parameters used in Run 4, 5 and 6 for depositions of niobium onto quartz samples.

Run	Sputtering Pressure (mbar)	Base Vacuum (mbar)	Power (kW)	Current (A)	Voltage(V)	Time (min)	Heating °C
4	$1e^{-2}$	$3e^{-7}$	10	33	300	30	150
5	$1e^{-2}$	$2{,}66e^{-7}$	15	50	293	30	150
6	$1e^{-2}$	$5e^{-7}$	15	50	300	30	350
7	$1e^{-2}$	$1{,}2e^{-7}$	17	50	330	30	350

In next figure are presented the measured RRR values as a function of the sputtering power at a half height of the external conductor (Position 15)
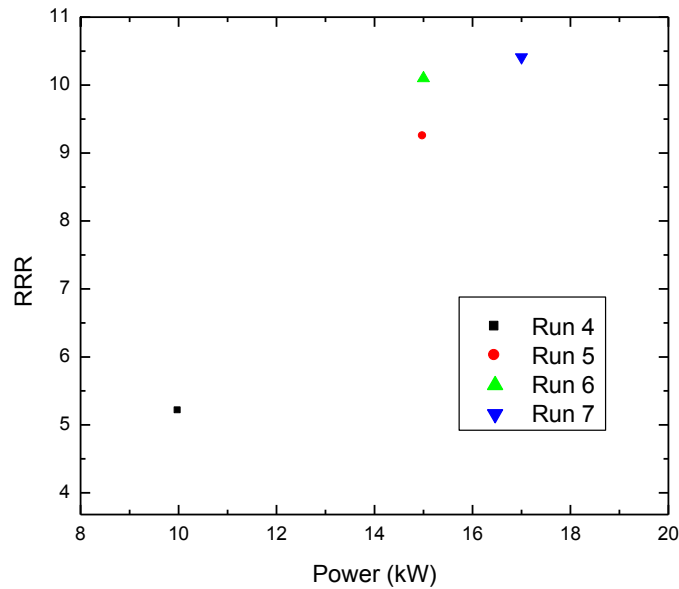
Figure 8.24. RRR vs sputtering power of Nb sample in position 15.

As it is presented in Figure 8.24, the RRR value increases with the increment of the sputtering power. There is a wide difference between Run 4 and Run 5, in which the power was increased from 10 to 15 kW. Higher discharge power increases the flux of sputtered atoms impacting the fil. This effect results in higher surface temperature and, in turn, to higher mobility of the Nb atoms, i.e., to more favorable conditions for growing larger crystal grains. However the maximum discharge power is limited by the heating of the cathode [70] that in this case is cooled. The effect of the heating temperature is seen between Run 5 and 6 in which increasing the substrate temperature, the RRR increased too. As was explained before high substrate temperature helps to enlarge the column size

of thin film. The ion bombardment also assists the improvement of the film structure less prone to defects [72].

Critical temperature against RRR values are presented in next figure
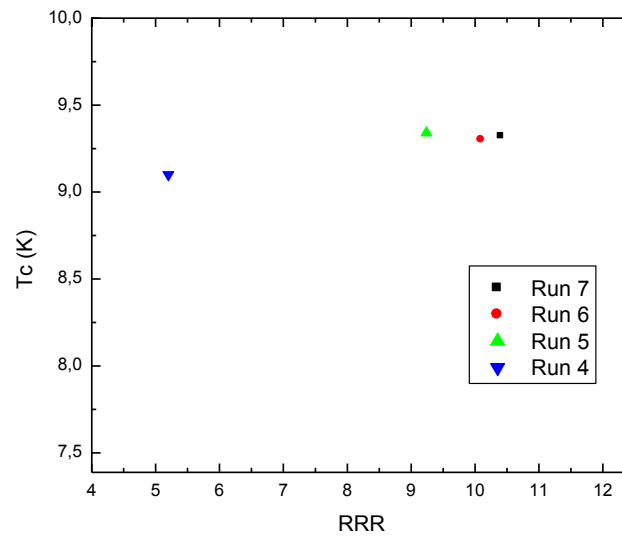
Figure 8.25 Critical temperature vs RRR for a sample located in the 15th position.

From the previous figure is possible to affirm that a higher values of RRR the critical temperature increased to a certain point close to the niobium transition. Sample deposited during Run 1, has the lower transition. It can be caused mainly for two factors: the thickness and the content of impurities. Recent studies has proven the depression of T_c with decreasing film thickness. This explanation is consistent with the results because the sample deposited in run one has lower thickness in comparison with the others samples. As was explained before higher sputtering power during the deposition, means higher substrate temperatures that insides directly on the grain size, crystallinity and impurity content of the film [76]. It is interesting to notice that films with slightly lower transition temperature than solid niobium could be subject to compressive stress of the lattice spacing during the measurement [72].

Following figure shows the transition got during the Run 7 of a quartz sample placed on the 15th position of the cavity. The values of T_c in 9, 32 K and ΔT_c is 0, 03 K. The Nb T_c is 9,32K, that is quiet a good value compared with the Nb bulk value (bulk T_c = 9.26K); moreover the ΔT_c that represent the sharp transition widths, generally (<0.02K) for a bulk Nb is in this case 0.02 [73].

Also during these four depositions, the thickness was measured. Following figure presents the thickness profile in function of the sample positions from Run 4 to Run 7.
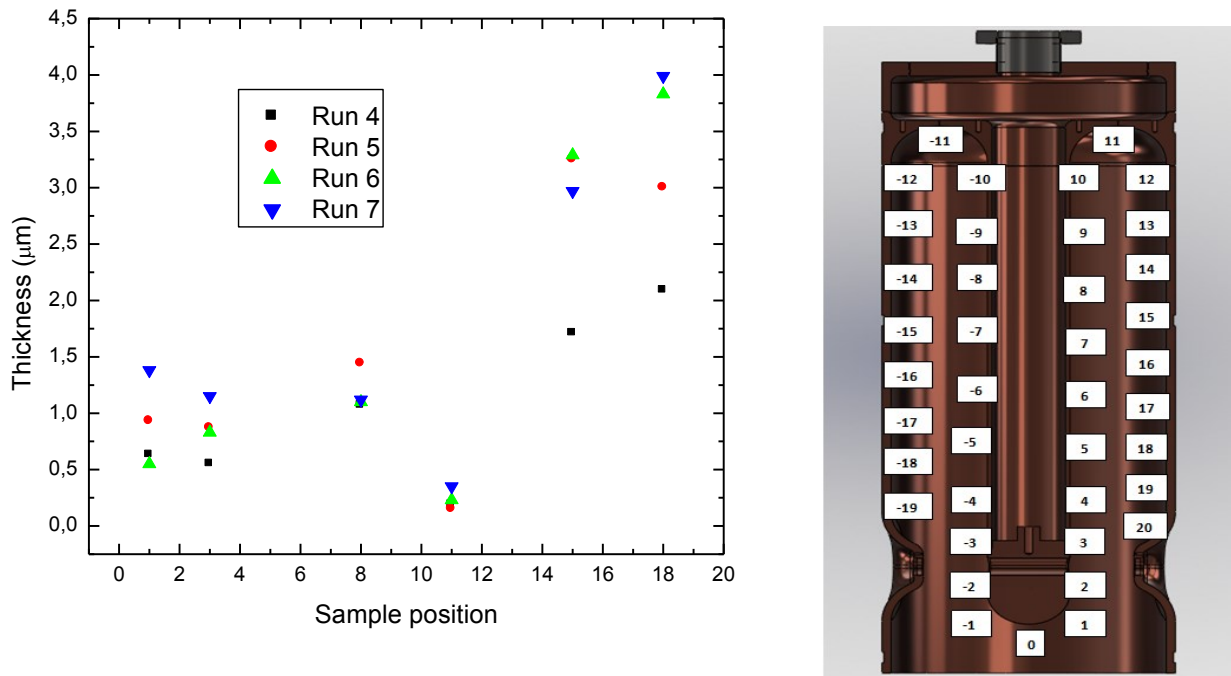
Figure 8.26 Thickness vs sample position using different parameters of process, from Run 4 to Run 7.

Observing Figure 8.26 there is a notable increasing of the thickness along the cavity from Run 4 to Run 7. It is evident the influence of the power on the deposition rate due to a higher ionization of the particles [63]. However the uniformity on the cavity surface is not the best. As usual thinner samples are located on the top of the cavity in position 11. On the other hand thicker samples are located on the external conductor. It is necessary improve the plasma on the top of the cavity and also to understand the influence of the argon pressure during the deposition.

Another set of depositions were performed, in which it is highlighted the increment of the sputtering power. Also in this case the results will be compared taking into account the 15th position in order to understand the influence of each parameter on the thin film properties.

Table 14. Parameters used to perform Run 8,9 and 10 for niobium onto quartz samples

Run	Sputtering Pressure (mbar)	Base vacuum (mbar)	Power (kW)	Current (A)	Voltage(V)	Time (min)	Heating °C
8	1e^{-2}	5e^{-7}	17	51	337	30	380
9	1e^{-2}	2,3e^{-7}	21	60	321	30	380
10	1e^{-2}	1e^{-7}	25	70	340	30	300

Next figure shows the Residual Resistance Ratio in function of the sputtering power. Actually the power increases the RRR because it increases also the rate deposition during the sputtering process as is shown in next equation.

$$fi = \frac{\alpha i N i}{\alpha i N i + R} \qquad \text{(Eq. 8.2)}$$

Where Ni is the number of atoms of species i bombarding unit area of film in unit time; αi is the sticking coefficient and R the deposition rate. In sputtering, there are three possible ways to reduce the contamination: reducing the background vacuum pressure (decreasing Ni); increasing the substrate temperature, increasing the amount of impinging niobium atoms over the impurity ions, hence increasing R [74].

It is possible to affirm the trend seen previously in which increasing the sputtering power, higher discharge are produced, increasing the flux of sputtered atoms. Until this point, it is possible to think about the deposition of the real copper cavity, since the highest RRR measured is 27; at least a RRR=20 is required in a SPC resonator [73]
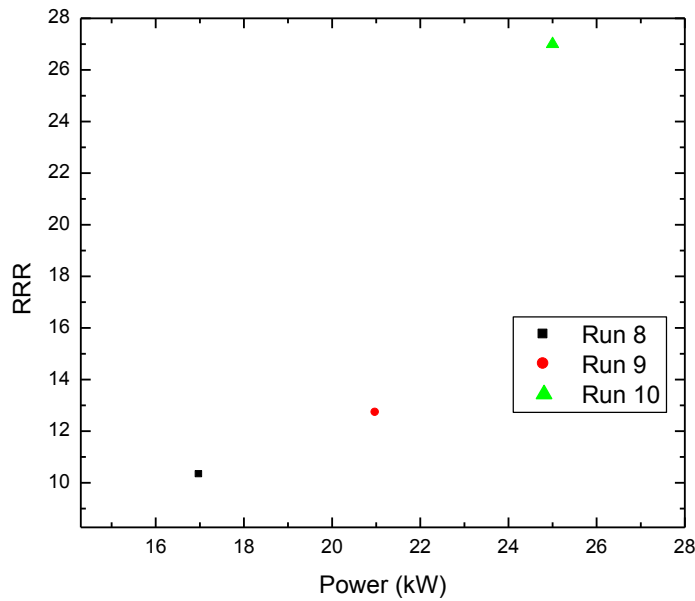
Figure 8.27. RRR vs power for a sample in position 15, using different parameters.

Also critical temperatures are presented in Figure 8.28. In which T_c was plotted against the RRR. As it was explained before, this two values are closely linked and they are indicators of the purity of the film. Here it is evident the improvement of the superconducting properties with the increment of the power. The transition temperature is the same of the niobium bulk for Run 8 and 10. (9, 27 and 9, 28 K respectively). A slightly difference is seen for Run 9 in which the T_c is a little bit higher (9,4K), however is close to the niobium transition
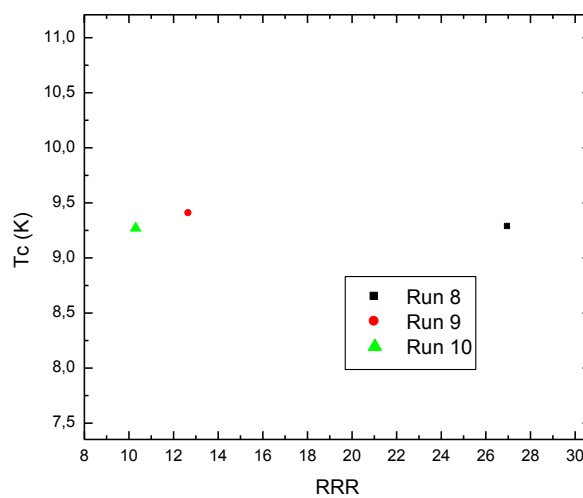
Figure 8.28. Critical temperature vs RRR for a sample located in the 15th position.

110
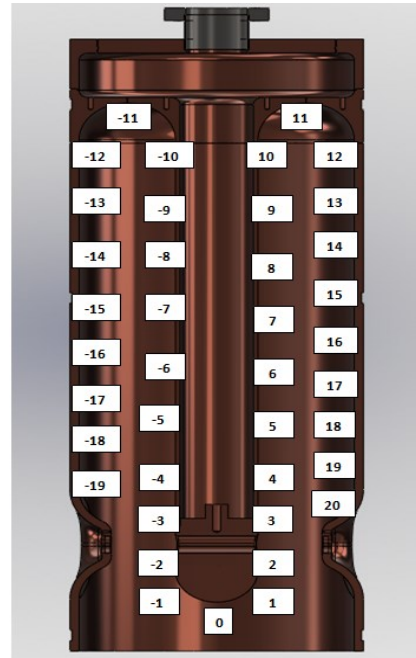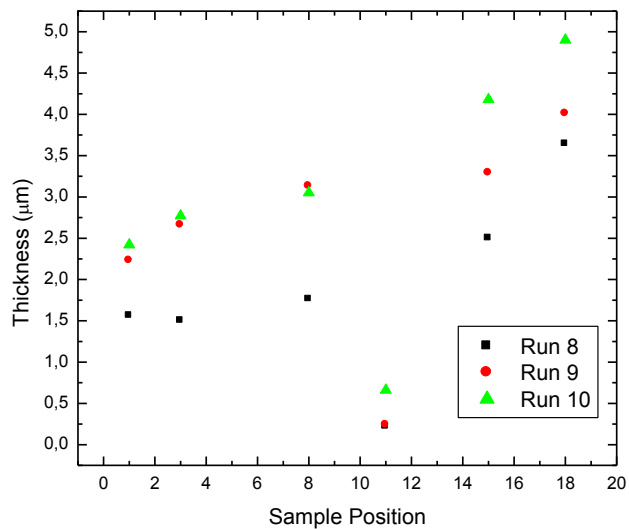
Figure 8.29. Thickness vs. sample position using different parameters of process, from Run 8 to Run 10.

Observing Figure 8.29 there is an increment of the thickness along the cavity from Run 8 to Run 10. Again the increment of the power affects the deposition rate during the sputtering process due to a higher ionization of the particles [63]. The uniformity on the cavity needs to be improved because of the thickness differences observed between the internal conductor, the top and the external conductor. As usual thinner samples are located on the top of the cavity in position 11, however the thickness is higher than before (0,66 μm).

8.2. "U" Path with permanent magnets

Until this point the superconducting properties are quite good to deposit the copper QWR, however the plasma is still weak on the top of the cavity and prevents the deposition of a uniform niobium film along the cavity. For this reason another magnetic field confinement was built and tested. The starting point of this configuration is a curve made with permanent magnets positioned along a stainless steel tube, oriented as is shown in the next figure.

111
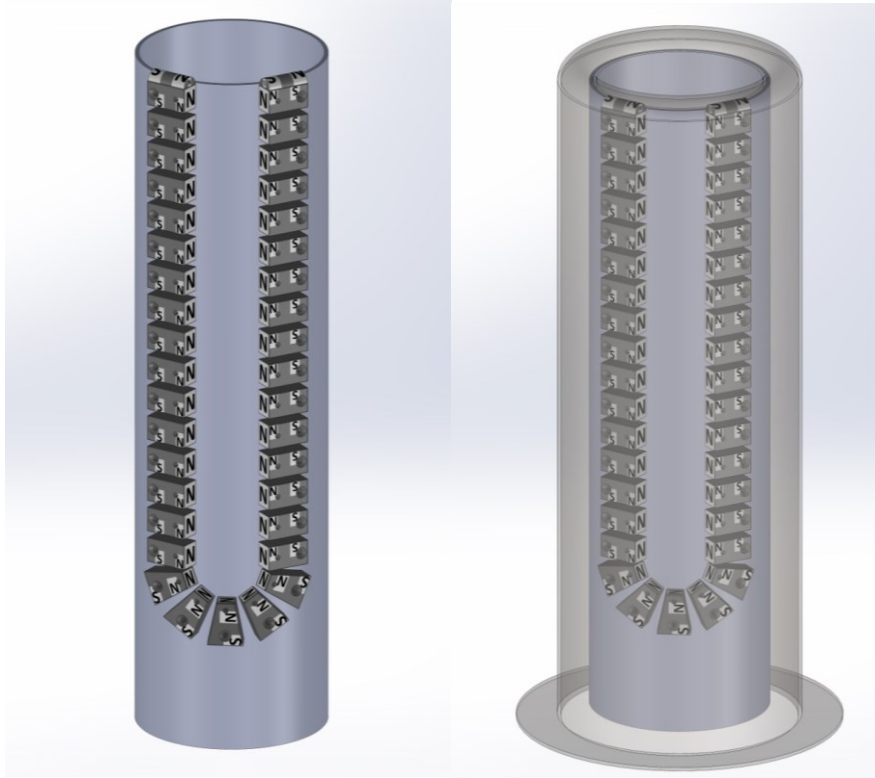
Figure 8.30.a) 3D drawing of second magnetic confinement, b) 3D drawing of second magnetic confinements inside the niobium cathode.

It was built another stainless steel cathode with the same shape of the niobium cathode, in order to simulate the magnetic field lines. A stainless steel cylinder was used as a magnetron body; the permanent magnets were placed along the path to study different configurations of the plasma. This configurations are presented in Table 15.

Table 15 Magnetic confinements test to study the plasma on the top of the cavity with the U path

Magnetic confinement	Plasma	Observations
H:U with permanent magnets		Magnetic field lines not closed
I:U with permanent magnets, decreasing the distance between the magnets and the cathode		Symmetric but low intensity plasma
J:U with permanent magnets + 2 permanent magnets at the extreme		Plasma quite symmetric and stronger than previous configuration
K:U with permanent magnets with modified magnets at the extreme of the U curve		Symmetric plasma but one side is stronger than the other one
L:Two U curves placed on the opposite side of the tube		Higher plasma density on the top of the cavity
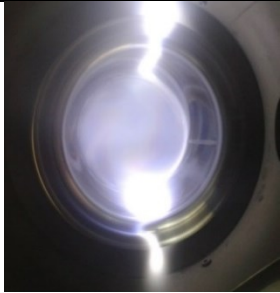
Observing previous table the plasma generated by the configuration **H** is not so strong and the magnetic field lines are not closed at one extreme, so it was decided to decrease the distance between the magnets and the cathode removing the ring at the end of the curve.

Respect configuration **I**, the magnetic field was improved in comparison with the configuration **H**, the plasma is symmetric, but it will be necessary to increase the plasma on the top of the cathode. One possible solution could be to add two more magnets on at the extreme of the curve or to decrease the distance between the magnets placed on the top of the tube and the top of the cathode. Table 15 shows the plasma generated by a magnetic field configuration in which it was added one magnet in each extreme of the curve (configuration **J**).

The magnetic field was improved; the plasma is quite symmetric and stronger than before. Nevertheless, it will be necessary to decrease the distance between the last magnet placed on the extreme and the top of the cathode. Further experiments were carried out focused on the improvement of the magnetic field on the top of the cathode and hence, increasing the deposition rate. It is well known that the superconducting properties of Niobium films are significantly modified by ion bombardment during deposition. In magnetrons, this effect is not uniform because ion density changes from place to place depending on the unbalance of the magnetic confinement, and when sputtering into a coaxial geometry closed at one end, such as into a QWR, this non uniformity is even greater [2]. Configuration **K** shows the argon plasma after decreasing the distance between the magnets and the top of the cathode and also after being modified to lift the magnetic path.

It can be seen also in Table 15, the improvement on the argon plasma by decreasing the plasma between the magnets an the top of the cathode; this parameter influences directly the deposition rate during the magnetron sputtering process; however the efficiency can be proved during depositions in where it has been calculated the uniformity along the cavity and the erosion of the cathode. In this the plasma is being evaluated only qualitatively. Next deposition will be performed with the final magnetic confinement. Also in the plasma generated by configuration **K** it can be noted differences between both sides of the curve.

Even if the plan is to rotate the magnetron during the deposition, the magnets were modified in order to be placed it in higher positions closer to the cathode. This plasma can be seen in Table 15, represents by the configuration **L**

From the table it can be observed more symmetry in both sides of the cathode that could allow to deposit a thicker film on the top of the cavity. However the plasma with the same magnetic confinement seen from another point of view is presented in the following figure, where one extreme seems to be stronger than the other one.
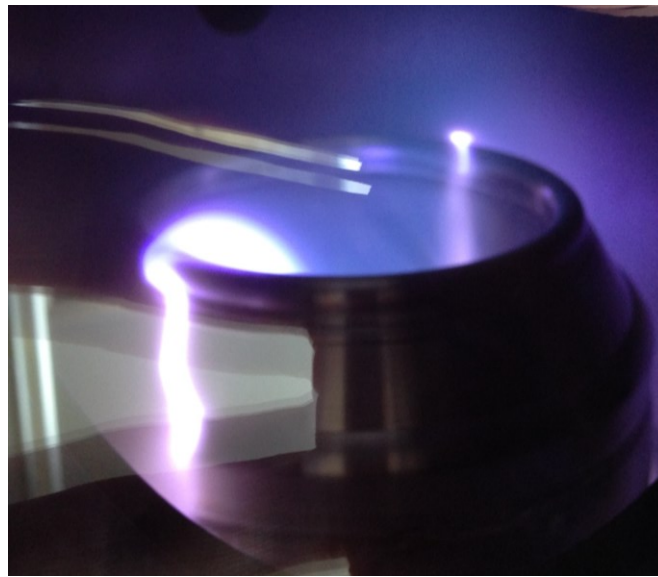
Figure 8.31. Lateral view of argon plasma produced by the modification of magnets placed on the extreme of the magnetic.

From previous experience it is difficult to increase the deposition rate by the modification of magnets or decreasing the distance. For this reason it was decided to add to the previous configuration (**L**) a curve of magnets, placed on the opposite part of the stainless steel tube. The configuration of two curves of magnets (configuration **M**) is presented at the end of Table 15. On the other hand following figure presents the argon plasma generated for this configuration from another point of view.
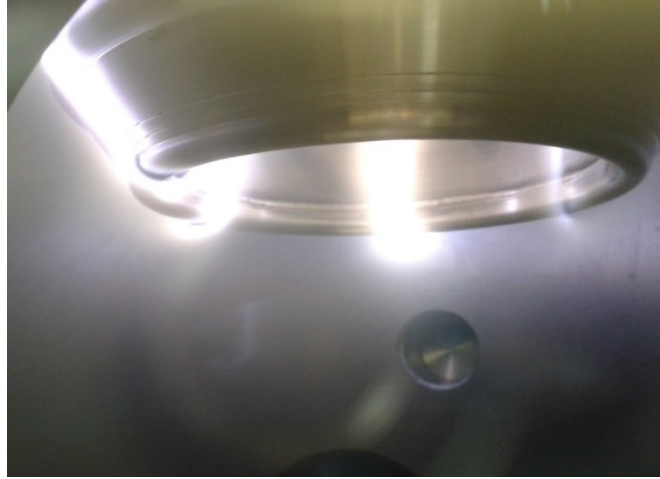
Figure 8.32.Lateral view of argon plasma produced by two curves of magnets placed on the opposite sides of the SS tube.

The plasma is quite intense by this configuration that is better than the previous one, it can be possible to dispose of higher deposition rates and moreover to sputter simultaneously all over the substrate. As was explained before high deposition rates are beneficial for the film purity, since increasing the arrival rate of Niobium atoms to the substrate, it decreases the fraction of impurities trapped in the film. Also in this proposal sputtering configuration exist the possibility to rotate the magnetron during the deposition, so might be expected to have greater influence on the thickness distribution along the cavity.

8.3. Definitive magnetic confinement test

8.3.1. Nb onto quartz samples

The magnetic confinement presented before was the last configuration tested in this study and it was considered the best option to increase the plasma on the top of the cathode and hence on the top of the QWR. Based on this experience, the magnetron was built in real scale, taking into account the dimensions of the resonator and also the niobium cathode, as is shown in Figure 8.33. Next results will be focused on the test of this magnetron configuration.
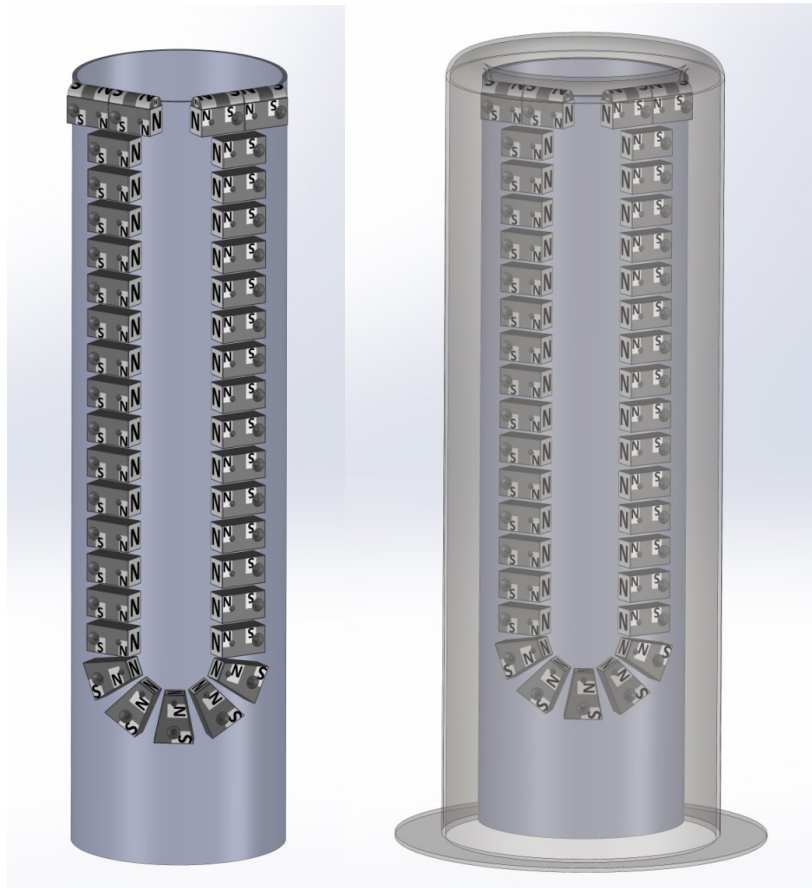
Figure 8.33. a) Lateral view of 3D drawing of final magnetic confinement b) Lateral view of 3D drawing of final magnetic confinements inside the niobium cathode.

The goal of this research was focused on the deposition of the niobium thin film and the RF performance. RF losses depend exponentially of critical temperature (T_c) and they are proportional to the square root of residual resistivity in normal state. Nevertheless, both T_c and Residual Resistivity Ratio (RRR) are affected by contamination by the residual vacuum pressure before the sputtering deposition. The fraction of impurities trapped during film growth is given by the equation 8.2 presented before, where *Ni* is the number of atoms of species *i* bombarding unit area of film in unit time; αi is the sticking coefficient and *R* the deposition rate [74].

In this research it has been deposited several films with the lowest possible pressures in the vacuum chamber. For this reason several leak detection and gas analysis have been done (see appendix B).

The first test deposition with the new magnetic confinement was carried out with a base vacuum of $4e^{-7}$ mbar and setting the following parameters.

Run	Sputtering Pressure (mbar)	Base vacuum (mbar)	Power (kW)	Current (A)	Voltage(V)	Time (min)	Heating °C
1	$1e^{-2}$	$4e^{-7}$	20	75	290	30	100

The setting of the parameters was chosen in order to improve the results that have been gotten before. It was decided to deposit the film at 20 kW and at high temperatures around 300 °C, however, during the deposition some problem arose with the IR lamps and it was impossible to heat at temperatures higher than 100°C.

In order to decrease the pressure on the vacuum chamber, a planar niobium magnetron was placed on the top of the system; as was explained before the niobium can getter ambient gas atoms and impurities. A discharge called "pre-sputtering" was carried out before the deposition for 20 minutes, at $8e^{-3}$ mbar, 1A and 400V. The results of the deposition are presented below. Figure 8.34 presents the thickness profile along the cavity.
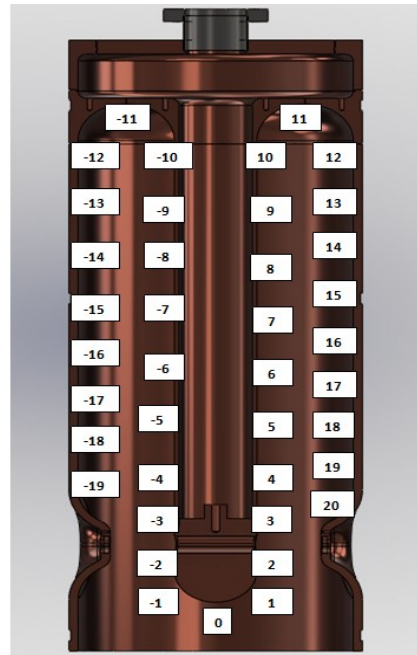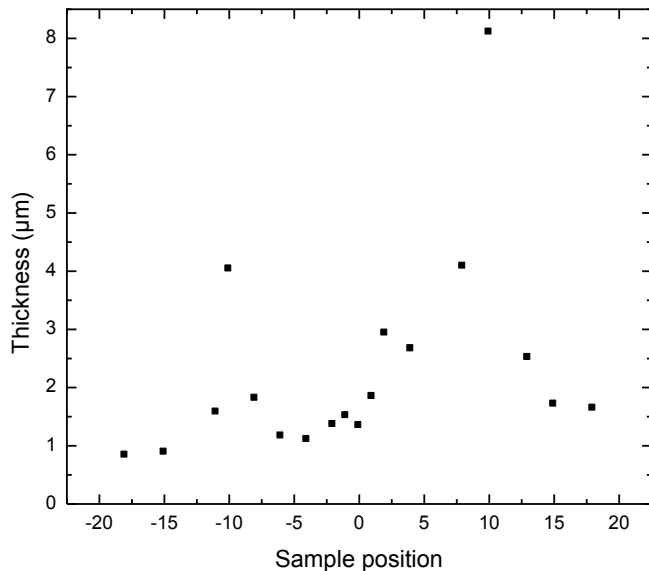

Figure 8.34. Run 1.Thickness profile of quartz samples deposited with niobium, using the definitive magnetron confinement.

118

As is shown, the new magnetron configuration allows to deposit the Nb film over the cavity at high deposition rates. The minimum value (0, 88μm) is located in position -15, while the media is around 1,5 μm. In comparison with the previous depositions the thickness on the top of the cavity was increased and it has similar values to the rest of the cavity. The thickness on the top of the cavity, specifically in position 11 is 1,5 μm. However there is one point located in position 10 where the thickness is much higher (8 μm) in which the film could be delaminated.

Table 17. Superconductive properties of Nb onto quartz samples, using the definitive magnetic confinement.

Sample	8	10	15
Thickness	4,08	8,1	1,71
RRR	10,3	6,37	5,4
T$_c$	9,5	9,16	9,21
ΔT$_c$	1,12K	311mK	67mK

Table 17 presents the superconductive properties (RRR and T$_c$) of Nb thin films onto quartz samples, in three positions: internal (position 8), top (position10) and external (position 15). From the previous table it can be noted that RRR values are different in all positions, probably due to differences on the heating. Higher values are present in position 8, in which the thickness is around 4μm and in which the temperature could be higher because of the distance from the sample to the magnetron body. The critical temperature is a little bit higher respect to the niobium bulk, probably because of the stress during the four point measurement. The lower RRR value was found in sample 15, placed at the external conductor. This sample is located on the external conductor of the cavity, farther from the magnetron respect to samples placed at the external conductor. It is important to highlight that two IR lamps placed over the external part of the cavity did not turn on during the process, therefore the heating in this zone was not efficient. It should be noted the influence of the temperature substrate on the RRR value; as was explained before at higher surface temperatures the mobility of Nb atoms is higher and helps to deposit larger crystal grains less prone to defects [70].

Based on previous results the new magnetron could improve the results. In last depositions with the first magnetic confinement it has been obtained less uniformity and plasma holes, but better RRR values.

Taking into account that previous deposition (using the definitive magnetron configuration) was performed with a non-uniform heating on the substrate and it could be possible to get better results next time. A new test deposition was carried out in order to perform a uniform baking much longer and also to do the sputtering process at higher temperatures (300°C). Table 18 presents the deposition parameters.

Table 18. Parameters used to perform the second test deposition, using the definitive magnetic confinement.

Run	Sputtering Pressure (mbar)	Base vacuum (mbar)	Power (kW)	Current (A)	Voltage(V)	Time (min)	Heating °C
2	6e $^{-3}$	1e^{-7}	30	75	410	30	300
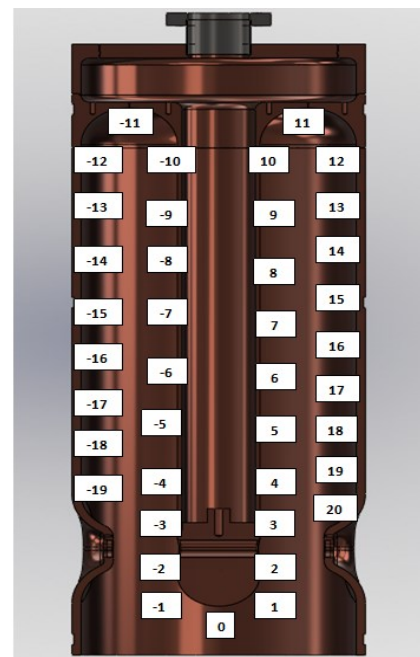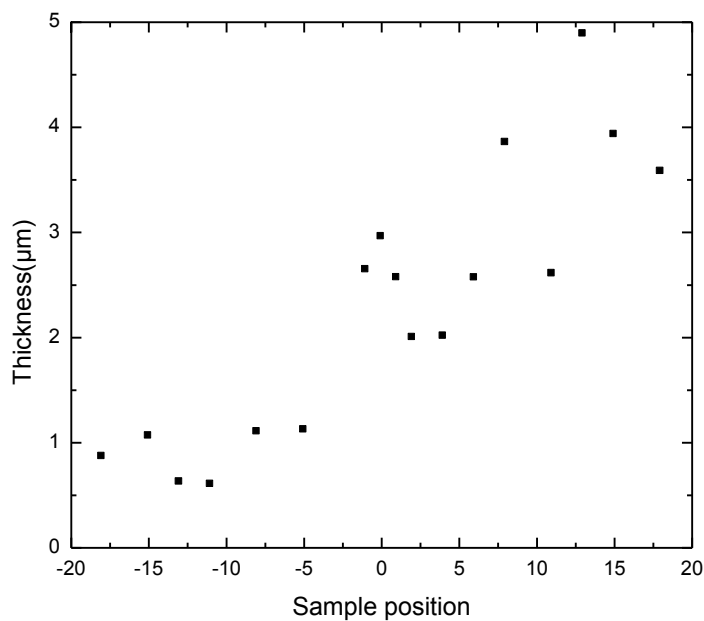
Figure 8.35. Run 2.Thickness profile of quartz samples deposited with niobium, using the definitive magnetron confinement.

From previous figure it is possible to note that the thickness is not uniform and there is not symmetry between the two cells of the resonator. The lowest value was found in position -13 (0,6 μm) and the highest value was found in position 13(4,89 μm). Probably lower argon pressures increased the mean free path between the electrons and hence decreasing the ionization efficiency

during the sputtering deposition. On the other hand next table shows the superconductive properties of the thin film deposited in this run.

Table 19. Run 2.Superconductive properties of Nb onto quartz samples, using the definitive magnetic confinement.

Sample	8	11	15
Thickness	3,25	2,32	3,89
RRR	61	30	27
T_c	9,3	9,31	9,29
ΔT_c	300 mK	201 mK	90 mK

There are some comments about previous results. Once again it is noted the influence of increasing the power on RRR values. About sample 8, increasing the sputtering power two times respect to Run 1, the RRR was increased 6 times. Nevertheless, in this Run the substrate temperature was increased until 300°C, so probably there are two effects on the increment of the RRR. The critical temperature for this sample is very close to the niobium bulk. Sample 11 has a RRR value of 30 with a transition temperature of 9,31K. The lowest measured value was found in position 15, as was found in the Run 1; however is quite good. Remember that at least a RRR value of 20 is required to deposit the QWR. The transition temperature for this sample is also close to the Nb bulk. The differences present along the cavity could be explained with differences on heating. The rotating magnetron allows having the same magnetic confinement in all zones.

Based in results of Run 1 and 2, it is possible to choose the best parameters to deposit the real QWR. It was decided to take from the Run 1 the argon pressure in order to get better uniformity and from Run 2 the power and the substrate temperature to increase the RRR values and a critical temperature close to the Nb bulk.

By the other hand SEM analysis were performed in order to observe the grain size and also to correlate the morphology with the substrate heating. The photomicrographs are presented in the following figure.
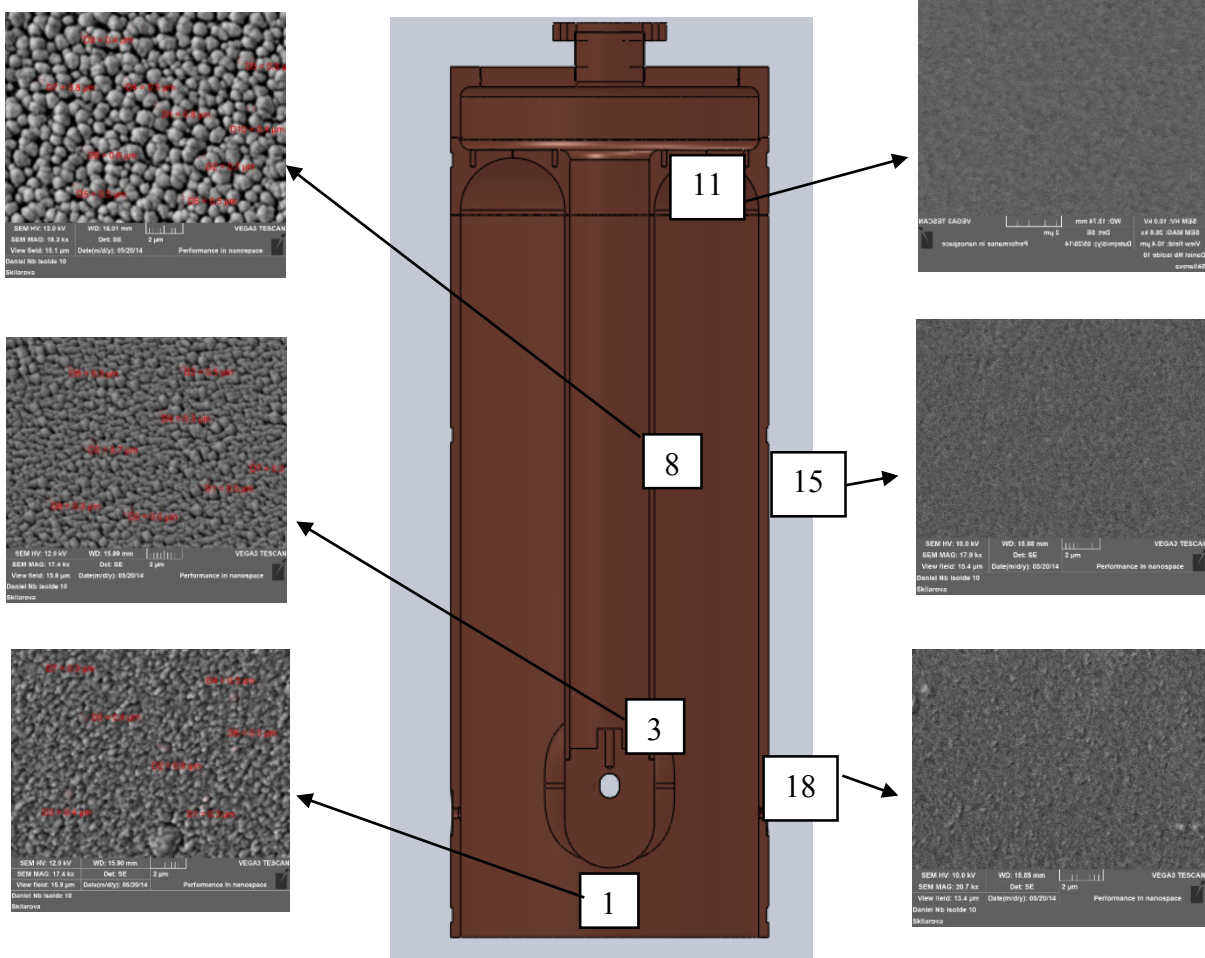
Figure 8.36. Morphology of the niobium samples sputtered at 30Kw for 30 min.

As was explained before it is required a good microstructure and to have sufficiently pure and ordered niobium film to have a good RF performance. From the picture it can be observed some differences between samples placed at the external, at the top and the internal conductor. Grains from sample 8 look well connected and larger respect to other samples, probably due to the more efficient heating in this zone, which is closer to the magnetron. Internal samples have a grain size around 400 -500 nm. On the top of the cavity and along the external conductor it is possible that the grain size was lower. This differences can be attributed to a non-uniform heating during the sputtering process.

Based on this, it will be necessary to improve the heating before the QWR deposition.

8.3.2 Quarter Wave Resonator deposition

Until now the research has been oriented on the configuration of the magnetron, the parameters of the process, the uniformity of the thickness and the superconductive properties of Nb onto quartz samples. Fortunately, it has been found the way to set the correct parameters to deposit the real copper cavity.

The baseline procedure to deposit the cavity starts at CERN with the surface treatment. The copper cavity chemically polished (SUBU) and then it was passivated with sulfamic acid. After the dust free copper substrate treatment was performed with a low pressure (8 bars) ultrapure water rinsing in clean room class 100 [45].

At the end of the surface treatment the copper cavity was sent to the LNL where the cavity was opened in a dust controlled environment and it was placed inside the vacuum chamber to reach the pressure necessary to perform the deposition.

The base vacuum was around $1e^{-6}$ mbar and the outgassing was performed for 72 hours to improve the vacuum. The vacuum chamber was baked at 170 °C and the copper cavity was baked at 400°C.

The following table shows the parameters used to deposit the QWR cavity.

Table 20. Parameters used to perform the first sputtering over the copper QWR.

Deposition	Sputtering Pressure (mbar)	Base vacuum (mbar)	Power (kW)	Current (A)	Voltage(V)	Time (min)	Heating °C
1	$1e^{-2}$	$1e^{-7}$	30	75	408	40	450

After the deposition, the vacuum system was cooled for several days; the cavity was taken out from the vacuum chamber to be cleaned with high pressure ultrapure water rinsing.

The cavity was successfully deposited and looks totally covered. The niobium thin film presents a mirror like surface as is shown in Figure 8.37

Figure 8.37. QWR cavity before and after the Nb deposition.
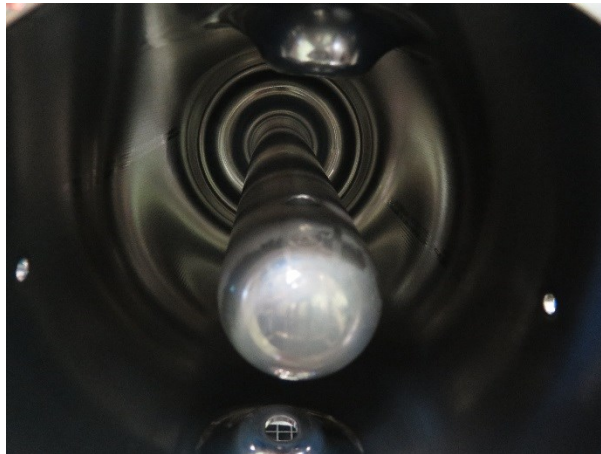
Figure 8.38. Nb/Cu QWR cavity after the high pressure rinsing.

The cavity was dried with ethanol and finally transported to the cryogenic laboratory to be mounted on the cryostat in order to be measured.

After assembling the antennas (pick-up, coupler), thermometers and coupler motion the QWR was fixed on the cryostat stand, it was placed inside the bunker to start the pumping. The cryostat was pumped for 48 hours in order to reach a base vacuum around 1e^{-6} mbar; then the cavity was baked at 100°C for 16 hours with an IR lamp that was placed inside the inner conductor.

The cooling was start opening the N_2 line to fill the gas layer until 77 K. During the cooling it was performed the external RF cable calibration that is independent of the temperature; it is possible to calibrate this part of the system either while the cavity is at room temperature or at helium temperature. The calibration procedure is automatized so it was necessary to follow the instructions of the control panel. The objective of power head sensor calibration and cables is to reduce the thermionic noise and reduce the error in RF measurements [75].

As was explained in chapter 3 the performance of a superconducting cavity is evaluated by measuring the Q_0 as a function of the cavity field level. This curves tell-tale signs of the activities inside the cavity. But before getting the curve some procedures must be followed.

Typical cavity performance is significantly below theoretical expected surface field limit. One phenomenon that limits the RF magnetic field is the "thermal breakdown", of superconductivity, produced at submillimeter size region of RF loss, called defects. When the temperature outside the defect exceeds the superconducting transition temperature T_c the losses increases, as large regions become normal conducting. Also high electric fields can limited the performance of superconducting cavities, by emission of electrons from local spots in the high electric field regions. In the case of QWR the high electric field is at the end of the inner conductor and the magnetic field is higher on the top of the QWR cavity [67]. Observing Figure 8.37, the inner conductor looks well deposited, however Nb coating looks different respect to the cavity walls; for this reason the performance of the cavity could be affected by field emission [3].

In early stages of the development of superconducting cavities, a major performance limitation is the multipacting that is a resonant process in which an electron avalanche builds up within a small region of the cavity surface. The essential idea to avoid multipacting with the conditioning process.

During the cooling the warm multipacting conditioning was carried out. After finding the resonant frequency of the cavity at room temperatures (101, 209272 MHz) by the critical coupling the cavity was partially conditioned. Figure 8.39 and Figure 8.40 show the cavity search at resonant frequency and the RF signal during the multipacting conditioning.
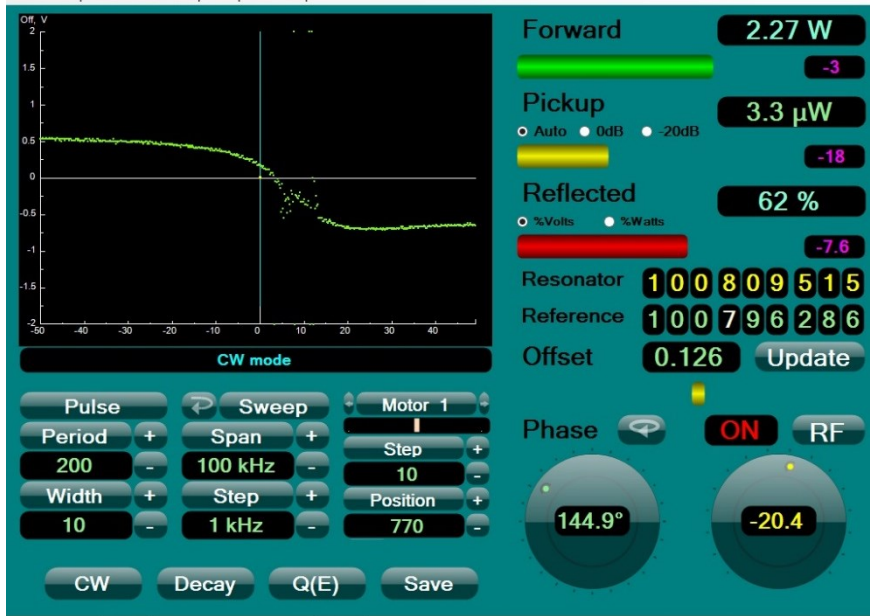
**Figure 8.39.Cavity search at resonant frequency.**
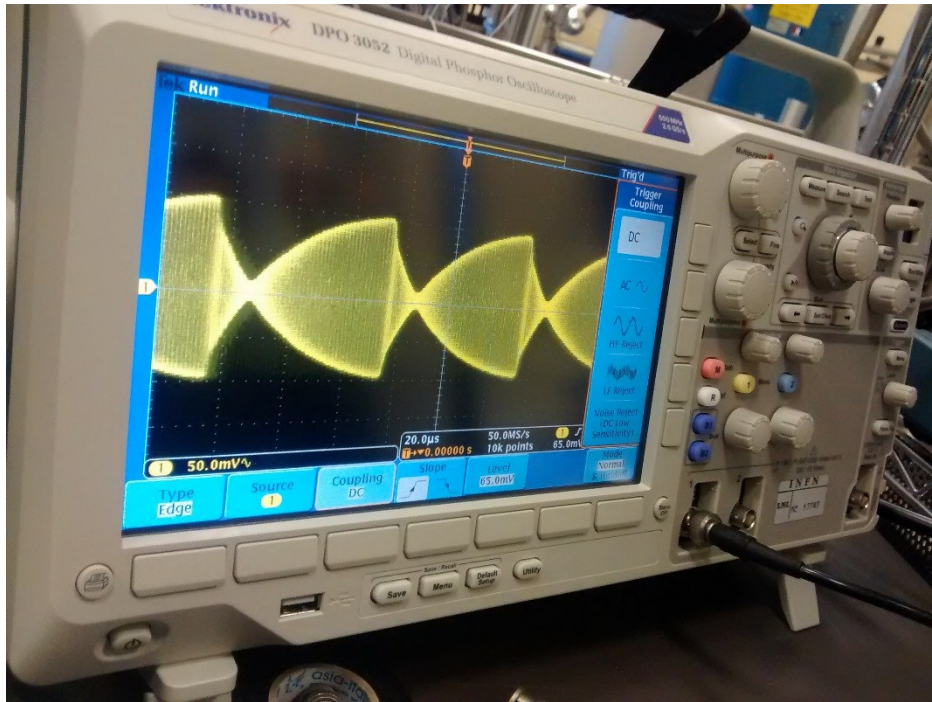
Figure 8.40.Oscilloscope signal during the multipacting conditioning.

The warm cavity conditioning at room temperature was performed in continuous wave (CW) at 3,2 Watt for three hours.

At this point it was possible to measure the Q_0 pick-up, through the decay procedure. This measurement was done only to see if the Q0 pick-up has a reasonable value. The decay time is not

important because it is used to calculate the Q values, so it is a redundant information. The results of the decay is shown in the following table in which are presented the preliminary results.

Table 21. Decay results of first RF measurement.

Decay time (s)	$1{,}137e^{-5}$
Q_0 pick-up	$2{,}586e^{9}$
Q (cal)	$1{,}439e^{4}$

The Q_0 pick-up at room temperatures has a relation with the Q_0, measured at 4, 2 K. From this value it was possible to have an idea about the Q of the cavity around 10^8.

In order to measure the quality factor at low temperatures, the cryostat was filled with liquid Helium. A Dewar of 250 liters was necessary to reach a temperature of 4,2k in 5 hours. Once the temperature reached the cool cables calibration was done and the cool multipacting conditioning was performed for at least 3 hours at 2,33 Watt with subsequent pulse power of 8WAt this time a second decay was done and increasing the power it was possible to obtain the points to plot the Q vs E_{acc} curve. The following figure shows the quality factor in function of the accelerating field.
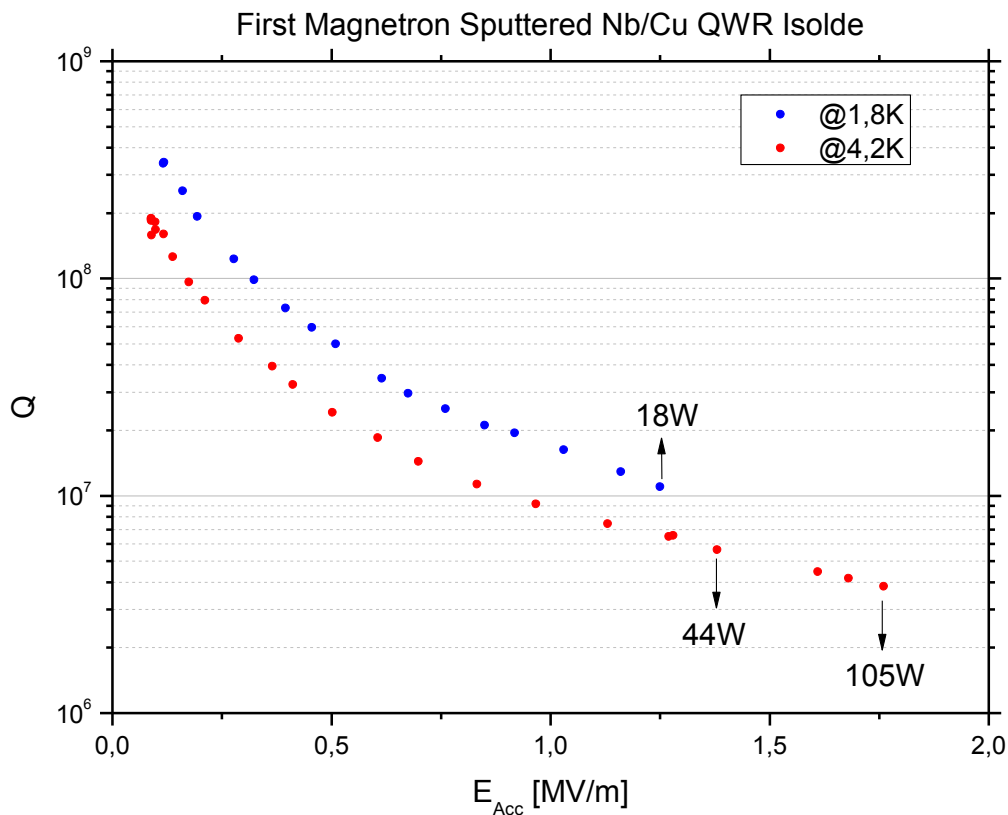

Figure 8.41. First measurement of Q vs Eacc of Nb/Cu cavity.

The Q curve plots the quality factor in function of the accelerating field. From this curve is possible to get information of dissipative processes of the cavity. If the curve is a horizontal line, the RF losses are constant, hence the ohmic resistance is independent of the accelerating field. If the resistance depends linearly of the accelerating field the Q curve has a slope. Increasing the accelerating field, if the heat is not removed properly, the temperature increases and also the Rs. The Q slope is typical of Nb sputtered cavities in which the grain size is lower respect to Nb bulk. Between grains, the resistance increases with the current, therefore the Nb sputtered film has an obstacle.

Increasing the current it is possible to have transitions from the super conducting state to normal conducting in small areas on the cavity surface; it can produces "Q switches" that are reductions on Q value that from a certain value of E_{acc}, moving the curve to lower values.

If increasing the direct current, the accelerating field does not increases and the curve goes down, there is a multipacting. Increasing the power, the E_{acc} remains constant until the multipacting level is not conditioned. A drop, usually concave downward curve is related to field emission, increasing the direct power the X-ray are emitted. A conditioning using helium can be efficient to straighten the curve. This mechanism is absent in this cavity because no electron emission or X-rays were detected during the measurement. Accelerating field was too low, so field emission is not the major factor of this losses.

Taking the models explained before the Q-drop of experimental results could be related to the presence of niobium oxides clusters in niobium, located at the oxide-metal interface, increasing the surface resistance (Rs).

Non uniform surface oxide layer can cause the presence of hot spots, which could cause the quench. The same effect can be produced by defects like vortex penetration at grain boundaries or precipitates. This effect generally is present in high fields.

Due to the strong difference between the residual resistance between the normal state and the superconducting state, small normal conducting areas can decrease the Q value of a resonator. It can be the explanation of the Q curve gotten before. Probably the thickness is not thick enough in certain zones in which the copper is seen by the RF field. The presence of surface defects, powder particles or contaminants in the film could increase the ohmic losses and therefore decrease the Q [76].

The Q_0 of previous figure ($2e^8$) is below CERN specifications, it was possible only to support very low accelerating fields (less than 2MV/m). Remember that is required a cavity with at least 5e8 of Q factor at 6 MV/m of accelerating field. As was explained before one possibility of the bad perform of the cavity RF fields, could be that the thickness is not enough in certain zones, therefore the cavity is normal conducting in this areas. For this reason it was decided to deposit a new layer of niobium over the niobium thin film deposited before. The deposition was done taking into account the same parameters used in the last deposition, but this time increasing the substrate temperature. Next table shows the parameters used to perform the deposition.

Table 22. Parameters used to perform the second deposition of the copper QWR

| Deposition	Sputtering Pressure (mbar)	Base vacuum (mbar)	Power (kW)	Current (A)	Voltage(V)	Time (min)	Heating °C
2	$1e^{-2}$	$8,2e^{-8}$	30	75	410	40	550
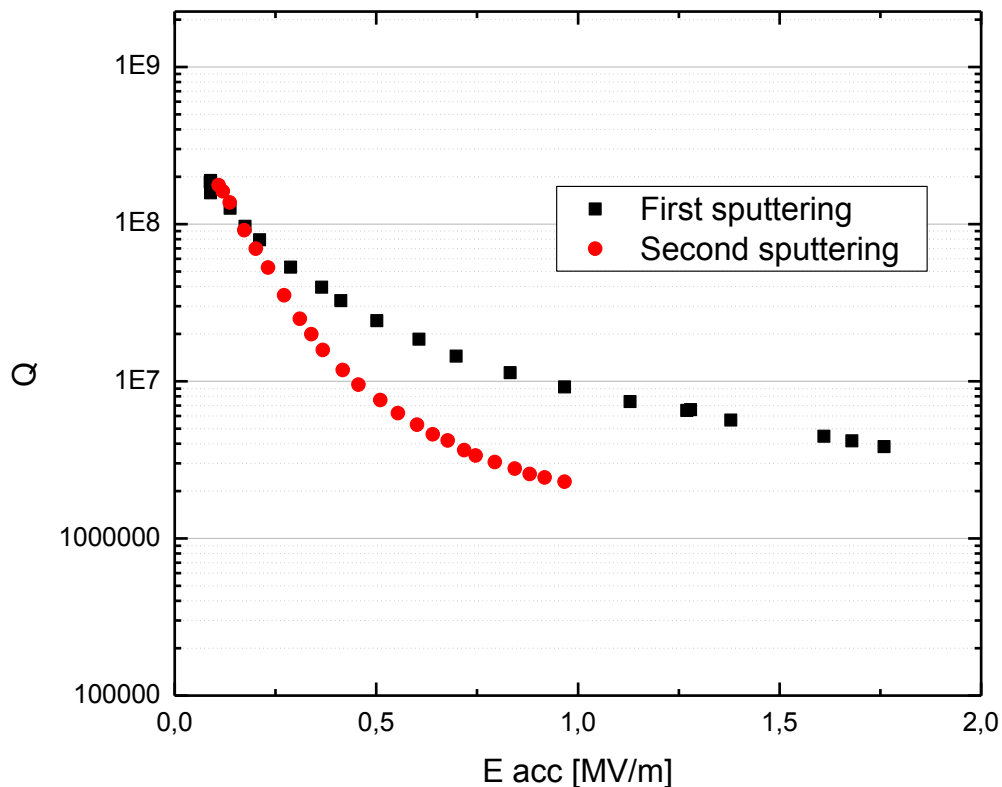
Figure 8.42. Second measurement of Q vs E acc. of Nb/Cu cavity at 4,2K.

There is a remarkable similarity between the Q disease shown in figure 7.11 and the Figure 8.42, in which the Q drops drastically from the beginning. When at accelerating field close to zero starts the degradation of the quality factor, it is possible to have hydrogen contamination of the niobium surface that is exposed to RF fields. This mechanism is usually absent in Nb/Cu cavities due to less demand on cryogenic system cooling velocity and reliability. [58]. However, Nb lattice has a large affinity for hydrogen, formation of hydrides in the RF surface during the cool down at 150-60 K [57].

As was explained before, during the thermal breakdown, part of the RF surface exceeds the critical temperature, becoming normal conducting and rapidly dissipating the stored energy in the resonator. In this measurement the transition to a normal conducting material was observed at low fields, so probably is linked to the oxygen effect and impurities. The niobium thin film was deposited while a magnetic path that rotated quite quickly; getting several thin film coating. In this case, those films are prone to accumulate the oxygen content throughout its thickness, increasing the possibility to decrease the Q value.

Another explanation can be related to the low Q is the contamination of the film after the deposition. However the baking effect on the BCS resistance remains after long terms exposure to air and high pressure water rinsing; unless the baking has been inefficient.

As is shown in Figure 8.42 after depositing the QWR the behavior was not improve respect to the first measurement. Actually the quality of the film is worse. The Q slope in the red curve drops much more drastically in comparison to the first deposition, reaching only 1MV/m. The Q_0 was kept around $2e^8$. One probably explanation of this performance could be correlated to impurities from the first coating, specifically (oxygen content) that has been absorbed for the second niobium thin film during the high pressure rinsing. The final recommendation of this research is focused on the outgassing of the cavity after the deposition and before the measurement in order to avoid the influence of impurities on the RF performance. Also it will be performed another deposition over the niobium thin film, reducing the motor speed in order to deposit a thicker film.

Chapter 9.

CONCLUSIONS

After carrying out and completion of each one of the objectives proposed in this research, it has been reached the following conclusions:

It has been built a vacuum chamber to be used on the deposition of thin films over Quarter Wave Resonators of HIE-Isolde type. It has been equipped with a new rotating magnetron sputtering source in order to deposit niobium coatings uniformly. It was necessary the construction of a test vacuum chamber in order to study the plasma on the top of the cathode.

The setting of the magnetron sputtering parameters was necessary to deposit a uniform thin film with good superconductive properties; it was demonstrated that a power of 30 Watts, an argon pressure of $6e^{-3}$ mbar and 30 minutes of time are required to deposit around 2 ± 1 µm of film along the cavity. It was chosen the second magnetic confinement as the best source to deposit the copper cavity. Power and the substrate temperature are the most influent parameters to increase the deposition rate and improve the superconductive properties of the film, increasing the mobility of niobium atoms during the sputtering process.

Respect the superconductive properties of the films, very good results were obtained. The niobium film has a minimum RRR of 20 on the top of the cavity and a maximum of 61 closer to the inner conductor. The critical transition of the niobium thin film was around 9.3 K.

SEM results allowed to analyze the microstructure of the niobium film. Bigger grains were founds on the inner conductor closer to the magnetron source; for this reason four IR lamps were placed over the cavity in order to improve the substrate heating during the deposition.

A test cryostat was successfully built in order to measure the RF performance; the system can be useful to perform measurements at 4.2 and 1.8 K. Respect to the RF performance Nb/Cu cavity is under the specifications of CERN with a maximum Q value of $2e^{8}$ and an accelerating field of 2MV/m; however some parameters will be changed in order to improve the performance and push the SRF community to use the magnetron sputtering technique as an economical method to deposit superconducting cavities in short times.

Chapter 10.

REFERENCES

[1] C. Benvenuti, N. Circelli, M. Hauer and W. Weingar, "SUPERCONDUCTING 500 MHz ACCELERATING COPPER CAVITIES SPUTTER-COATED WITH NIOBIUM FILMS," *Proceeding of SRF workshop,* vol. 21, no. 34, p. 628, 1984.

[2] V. Palmieri et. al, "NEW RESULTS ON NIOBIUM-SPUTTERED COPPER QUARTER WAVE RESONATORS," *Proceedings of the 6th Workshop on RF superconductivity,* vol. 2, p. 868, 1993.

[3] W. Venturini et. al, "Nb Sputtered Quarter Wave Resonators for the HIE-ISOLDE," *Proceeding SRF 2013,* vol. A, no. 03, pp. 767-772, 2013.

[4] CERN, "How acellerator works," CERN, 22 March 2014. [Online]. Available: http://home.web.cern.ch/about/how-accelerator-works. [Accessed 22 March 2014].

[5] L. Suelzle, «Progress on RF electron superconducting accelerators,» in *Proceeding accelerator conference 1973*, Standford, California, 1973 pp 44.

[6] CERN, "The ISOLDE radioactive ion beam facility," 22 March 2014. [Online]. Available: http://isolde.web.cern.ch/. [Accessed 22 March 2014].

[7] CERN, "ISOLDE facility," CERN, 22 March 2014. [Online]. Available: http://isolde.web.cern.ch/facility. [Accessed 22 March 2014].

[8] M. Pasini, "A SC UPGRADE FOR THE REX-ISOLDE ACCELERATOR AT CERN," in *Proton and Ion Accelerators and Applications*, Victoria, Canada, 2008, pp. 123-126.

[9] CERN, "HIE ISOLDE," CERN, 2012. [Online]. Available: http://hie-isolde.web.cern.ch/hie-isolde/pdf/HIE-ISOLDE%20long%20description.pdf. [Accessed 10 June 2014].

[10] A. Abrikosov, "Superconducting metals," in *Fundamentals of the theory of metals*, Netherlands, Elsevier science publishers, 1988, p. 315.

[11] C. Poole, "Supercondcuctor types," in *Handbook of superconductivity*, San Diego. USA, Academic press, 2000, pp. 71-108.

[12] V. Palmieri, "The clasical superconductivity phenomenology of low temperature superconductors," *on A. Barone, A. Morini, L. Frunzio eds., European Training on Technologies and Industrial Applications of Superconductivity, World Scientific Publ.,* p. 12, 1992.

[13] E. Minot, "http://www.physics.oregonstate.edu/~minote/COURSES/ph672_2009/doku.php?id=hw8," 3 March 2009. [Online]. Available: http://www.physics.oregonstate.edu/~minote/COURSES/ph672_2009/doku.php?id=hw8. [Accessed 15 September 2014].

[14] J. Bardeen et al, "Theory of superconductivity," *Physical review,* vol. 108, p. 1175, 1957.

[15] G. Lanza, «NEW MAGNETRON CONFIGURATIONS FOR SPUTTERING NIOBIUM THIN FILMS,» in *PHD thesis University of Padua*, Padua, 2008, pp. 3-23.

[16] A. Pippard, «Superconductivity,» *Proc.Roy sos,* vol. A, n. 203, p. 98, London 1950.

[17] J. Waldram, «Surface Impedance of Superconductors,» *Adv. Physics,* vol. 1, p. 13, 1964.

[18] V. Palmieri, «Superconducting resonant cavities,» *A. Barone, A. Morini, L. Frunzio eds. European training on technologies and industrial applications of superconductivity,* pp. 224-255, 1992.

[19] H. Padamsee, RF SUPERCONDUCTIVITY for accelerators, New York: John Wiley and sons, 1998. Pp. 8.

[20] I. Ben-Zvi, "THE QUARTER WAVE RESONATOR AS A SUPERCONDUCTING LINAC ELEMENTS," *Nuclear Instruments and Methods,* vol. 212, pp. 73-79, 1982.

[21] G. Barbato, «Electrodeposition of tantalum and niobium using ionic liquid,» in *Graduate Department of Materials Science and Engineering. University of Toronto*, Toronto, 2009.

[22] L. Catani, «Deposition and Characterisation of Niobium Films for SRF Cavity Application,» in *EUROCON, 2007. Presentation at The International Conference on Computer as a Tool*, Warsaw, 2007.

[23] H. Padamsee, RF superconductivity science, technology and applications, NY. USA: Willey-VCH, 2008. Chapter 5. Pp. 207.

[24] J. Splett et al, "AComparison of Methods for Computing the Residual Resistivity Ratio of High-Purity Niobium," *Journal of Research of the National Institute of Standards and Technology,* Vols. Volume 116,, no. 1, p. 489, 2011.

[25] W. Singer et al, "RRR-Measurement Techniques on High Purity Niobium," in *TTC*, Chicago, 2010.

[26] C. Antoine, «PHYSICAL PROPERTIES OF NIOBIUM AND SPECIFICATIONS FOR FABRICATION OF SUPERCONDUCTING CAVITIES,» in *Technical Division Note FERMILAB*, Chicago. USA, August 2006.

[27] P. Bosland et at, "Preparation and RF Tests of L-Band Superconducting Nb Coated Cu Cavities," *IEEE Trans. on Appl. Superc.,* vol. 9, no. 2, p. 896, 1999.

[28] S. Calatroni et al, "HIGH-Q, HIGH GRADIENT NIOBIUM-COATED," *Proceeding at the 9th Workshop on RF Superconductivity,* vol. MOA, no. 002, p. 9, 1999.

[29] P. Bauer et al, "A collection of selected high fields Q- slope studies, models and comments," in *Review of Q-drop in SRF cavities*, TD 05-56, 2006 Pp 4-30.

[30] B. Visentin, ""High Field Q-Slope and Oxygen Diffusion," in *Presentation at the workshop on RF superconductivity*, Ithaca, USA, July 2005.

[31] P. Kneisel, "Preliminary Experience with in-situ Baking of Niobium Cavities," in *Proceedings of the 1999 workshop on RF superconductivity*, Santa Fe. USA, 1999 Pp 328.

[32] G. Eremeev, "New Results on the High Field Q-Slope," in *presentation at the 2005 workshop on RF superconductivity*, Ithaca.USA, 2005.

[33] J. Halbritter, ""Material Science of Nb RF Accelerator Cavities: Where do we stand," in *10th Workshop on RF Superconductivity. MA006*, Tsukuba - JAPAN, 2001.

[34] V. Palmieri, «THE PROBLEM OF Q-DROP IN SUPERCONDUCTING RESONATORS REVISED BY THE ANALYSIS OF FUNDAMENTAL CONCEPTS FROM RF-SUPERCONDUCTIVITY THEORY,» *Proceedings of the 12th International Workshop on RF Superconductivity,* vol. TUA, n. 02, pp. 162-166, 2005.

[35] A. Grassellinoet al, «Medium field Q-slope studies in quarter wave cavities,» *Proceeding SRF 2009,* vol. TUPP0, n. 62, p. 375, 2009.

[36] A. Valente et al, «"Study of the Residual Resistance of Superconducting Niobium Films at 1.5 GHz",» in *Proceeding of the 1999 workshop on RF superconductivity*, Santa Fe. USA, 1999 Pp. 550-554.

[37] P. Kneisel, ""Performance of Large Grain and Single Crystal Niobium Cavities"," in *Presentation at the 2005 workshop on RF superconductivity*, Ithaca. USA, 2005.

[38] F. Schlander, Study of Quality and Field Limitation of Superconducting 1.3 GHz 9-Cell RF-Cavities at DESY, Hamburg: PHD thesis, 2012 Pp 20-23.

[39] A. Porcellato, Presentation at "Corso macchine acceleratrici", Legnaro. Padua, 2003.

[40] H. Padamsee, "Multipacting and field emmision," in *RF superconductivity*, Weinheim, Wiley-VCH, 2009, pp. 85-128.

[41] H. Padamsee, «Field emission,» in *RF superconductivity science, Technology and Applications*, Weinheim, Wiley-VCH, 2009, p. 94.

[42] Cornell University document, "SRF cavities," October 2014. [Online]. Available: http://www.classe.cornell.edu/Research/SRF/SrfCavitiesAPrimerTwo.html].

[43] J. Böhlmark, "Fundamentals of High Power Impulse," in *Linköping Studies in Science and Technology*, Linköping, 2006, p. 16.

[44] L. WELLINGTON, "SPUTTER DEPOSITION OF ZNO THIN FILMS," in *PHD thesis. University of Florida*, Florida, 2001, p. 63.

[45] R. Behrisch, "Sputtering by Particle Bombardment III," in *Topics in applied physics*, California, Springer-Verlag, 1991, pp. 3-28.

[46] R. Behrisch., "Sputtering by particle bombardment II," in *Top. Appl. Phys*, Berlin, Springer, 1983, pp. 231-269.

[47] K. Klabunde, "Thin films from free atoms and particles.," Orlando, Academic Press, INC. ISBN, (1985), p. 257.

[48] P. Kelly and R. Arnell, "Magnetron sputtering: a review of recent developments and applications," *Vacuum technlogies,* vol. 56, pp. 159-172, 2000.

[49] D. Franco, "CONSTRUCTION OF AN INNOVATIVE CYLINDRICAL MAGNETRON SPUTTERING SOURCE FOR E FOR ISOLDE SUPERCONDUCTING Nb/Cu QWRs," in *Master thesis University of Padua*, Padua, 2011.

[50] D. Glockera, "Recent developments in inverted cylindrical magnetron sputtering," *Surface and coating technologies,* vol. 146, p. 457–462, 2001.

[51] X. Li et al, "Influence of deposition on the reactive sputter behaviour during rotating cylindrical magnetron sputtering," *Journal of applied physics,* vol. 41, pp. 1-6, 2008.

[52] M. Martinello, "SPUTTERING DI FILM SUPERCONDUTTORI DI NIOBIO IN CAVITÀ ACCELERATRICI A QUARTO D'ONDA," *Tesi di Laurea Università di Padova,* p. 37, 2010.

[53] B. Ferrario, "Introduzione alla tecnología del vuoto", Bologna: Patron editore, 1999.

[54] S. Avdiaj and B. Erjavec, "OUTGASSING OF HYDROGEN FROM A STAINLESS STEEL VACUUM CHAMBER," *Original scientific article/Izvirni znanstveni ~lanek,* vol. 2, pp. 161-167, 2012.

[55] W. Frisken, « NON-UNIFORMITIES IN HYDROGEN AND OXYGEN CONCENTRATION IN NIOBIUM FILMS,» *Proceedings of the 1999 Workshop on RF Superconductivity,* pp. 312-317, 1999.

[56] C. Benvenuti, "Evolution of the getter technolody during the last 40 years," *Particle accelerators and solar panels,* vol. 29, no. 01-2, p. 31, 2013.

[57] W. Frisken et al, «NON-UNIFORMITIES IN HYDROGEN AND OXYGEN CONCENTRATION,» *Proceedings of the 1999 Workshop on RF Superconductivity,* vol. TUP, n. 040, pp. 312-318, 2004.

[58] Dektak 8 Surface Profiler - Bruker –, "Decktak 8 user manual," 2014. [Online]. Available: http://www.tstvn.com/en/nanotechnology-a-semiconductor/metrology-tools/opticalprofiler/bruker/bruker-.html.

[59] S. Stark, "Instrumentation and Software Upgrade of Tc and RRR Measurement System," *LNL Annual report,* p. 185, 2012.

[60] K. Vernon-Parry et al, "Electronic and structural properties of grain boundaries in electron-irradiated edge-defined film-fed growth silicon," *Sheffield Hallam University Research Archive,* vol. 1, pp. 1-4, 2004.

[61] N. Jecklin, "NIOBIUM COATINGS FOR THE HIE-ISOLDE QWR SUPERCONDUCTING ACCELERATING CAVITIES," *Proceedings of SRF2013,* vol. TUP, no. 073, pp. 605-607, 2013.

[62] J. Weisend, The Handbook Of Cryogenic Engineering, Philadelphia USA: Taylor and Francis, 1998 Pp 259.

[63] Adam L. Woodcraft, "An introduction to cryogenics," *Edimburgh University report,* pp. 1-10, 2007.

[64] http://www.technifab.com/cryogenic-resource-library/about-vacuum-technology.html].

[65] S. Stark and A. Porcellato, "WIDE BANDWIDTH LOW COST SYSTEM FOR CAVITY MEASUREMENTS," *Proceedings of HIAT09 , Venice, Italy,* vol. C, no. 08, pp. 274-277, 2009.

[66] M. Stirbet, "RF Conditioning: Systems and procedures," in *Presentation at High Power Couplers Workshop*, NewportNews, 2002.

[67] M. Farooq, "Optimization of the Sputtering Process for Depositing Composite Thin Films," *Journal of the Korean Physical Society,* vol. 40, no. 3, pp. 511-515, 2002.

[68] Kurt J. Lesker, "Practical Process Tips," *Lesker tech,* vol. 7, 2010.

[69] Y. Zhang, "Sputtering niobium films into a RFQ model & Sputtering of superconducting V3Si films," *PHD thesis. China Institute of Atomic Energy,* 1998.

[70] J. Halbritter, "Transport in superconducting niobium films for radio frequency applications," *Journal of applyed physics,* vol. 083904, p. 97, 2005.

[71] H. Padamsee, "The science and technology of superconducting cavities for accelerators," *Superconductor science and technology,* vol. 14, pp. 28-51, 2001.

[72] R. Russo, "INFLUENCE OF COATING TEMPERATURE ON NIOBIUM THIN FILMS," *Proceedings of the 1997 Workshop on RF Superconductivity,* vol. D, no. 11, pp. 890-897, 1997.

[73] A. Soublet, "PRELIMINARY RESULTS OF NB THIN FILM COATING FOR HIE-ISOLDE SRF CAVITIES OBTAINED BY MAGNETRON SPUTTERING," *Proceeding SRF 2013,* vol. TUP, no. 073, pp. 605-607, 2013.

[74] G. Schucan, "Niobium films produced by magnetron sputtering using an Ar-He mixture asdischarge gas," *Proceedingsofthe1995WorkshoponRFSuperconductivity,* vol. C, no. 22, pp. 479-483, 1995.

[75] G. Wu, "Energetic Deposition of Niobium Thin Film in Vacuum," in *PHD thesis Virginia Polytechnic Institute and State University*, 2002.

[76] F. AL GHAMDI et al, "FM AL GHAMDI PREPARATION AND PROPERTIES OF NIOBIUM THIN FILMS," *K.A.U Sci.,* vol. 5, p. 99, 1993.

[77] R. Russo et al, "High quality superconducting niobium films produced by an ultra-high vacuum cathodic arc," *Supercond. Sci. Technol.,* vol. 18, pp. 41-44, 2005.

[78] D. Tonini et al, "MORPHOLOGY OF NIOBIUM FILMS SPUTTERED AT DIFFERENT TARGET-SUBSTRATE ANGLES," *Proceeding of 11th Workshop on RF Superconductivity,* pp. 1-8, 2003.

[79] R. Thakur et al, "SRF measurement procedure of tesla type 6GHz cavities," Padua, 2012.

[80] A. Porcellato, "QWR niobium sputtering," *Presentation at "12° International workshop in RF superconductivity",* 2005.

[81] Phiffer, «Rotary pumps».

[82] K. Sang-hoon, "Superconducting RF Cavities Development at Argonne National Laboratories," *AKPA - IBS Symposium on Special Topics in Physics,* p. 4, 2014.

[83] Y. Kadi and A. Herlert , "The HIE-ISOLDE Project," *Journal of Physics: Conference Series312,* vol. 311, pp. 1-2, 2011.

[84] M. Pasini et al, "Progress on RF electron superconducting accelerators," *ProceedingsofLINAC08,* 2008.

[85] M. Pasini et al, "HIE-ISOLDE LINAC: STATUS OF THE R&D ACTIVITIES," in *Proceedings of HIAT09,,* Venice, Italy, 2009, pp. 165-169.

APPENDIX A

Next figures show the different arrangement studied between the spiral magnetron body (first configuration studied) and different magnetic confinements placed above it.
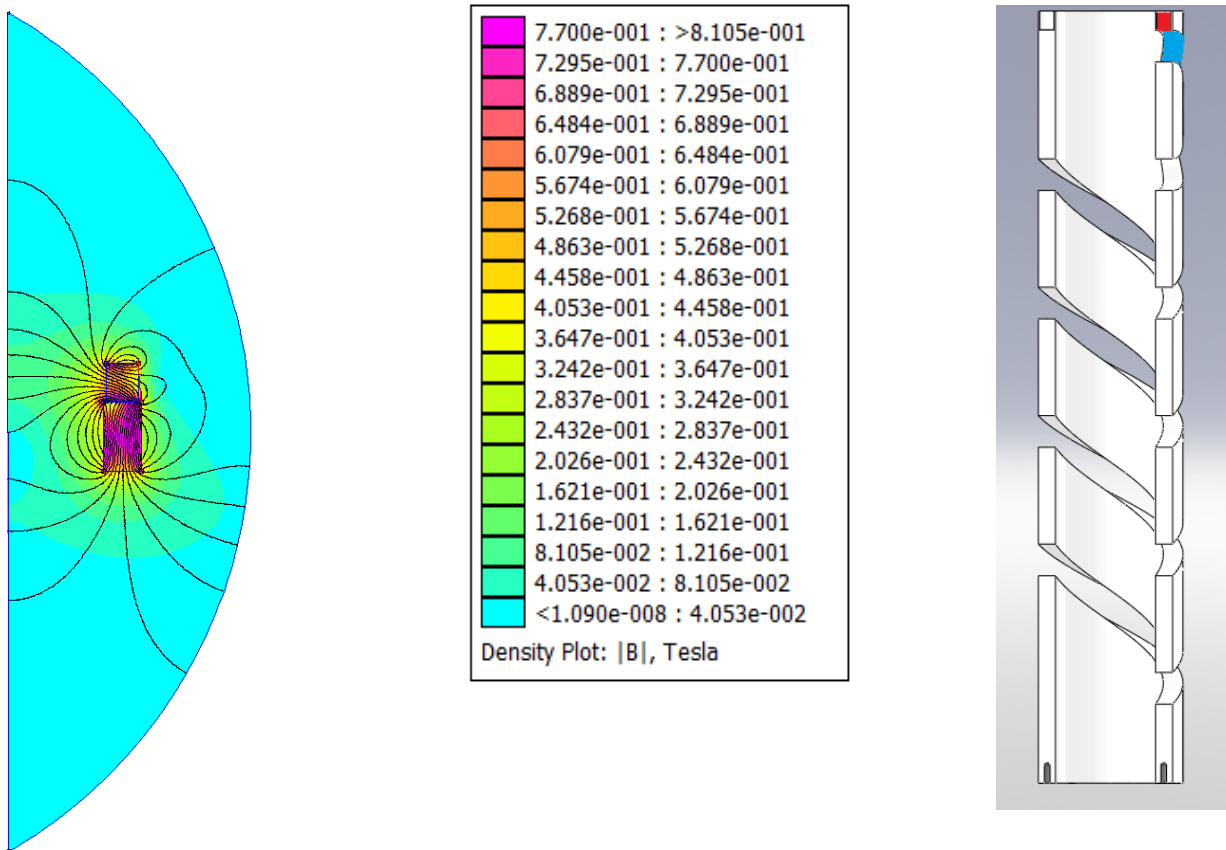

Figure A.1 Interaction between spiral of NdFeB and layers of NdFeB placed on the top of the crown.
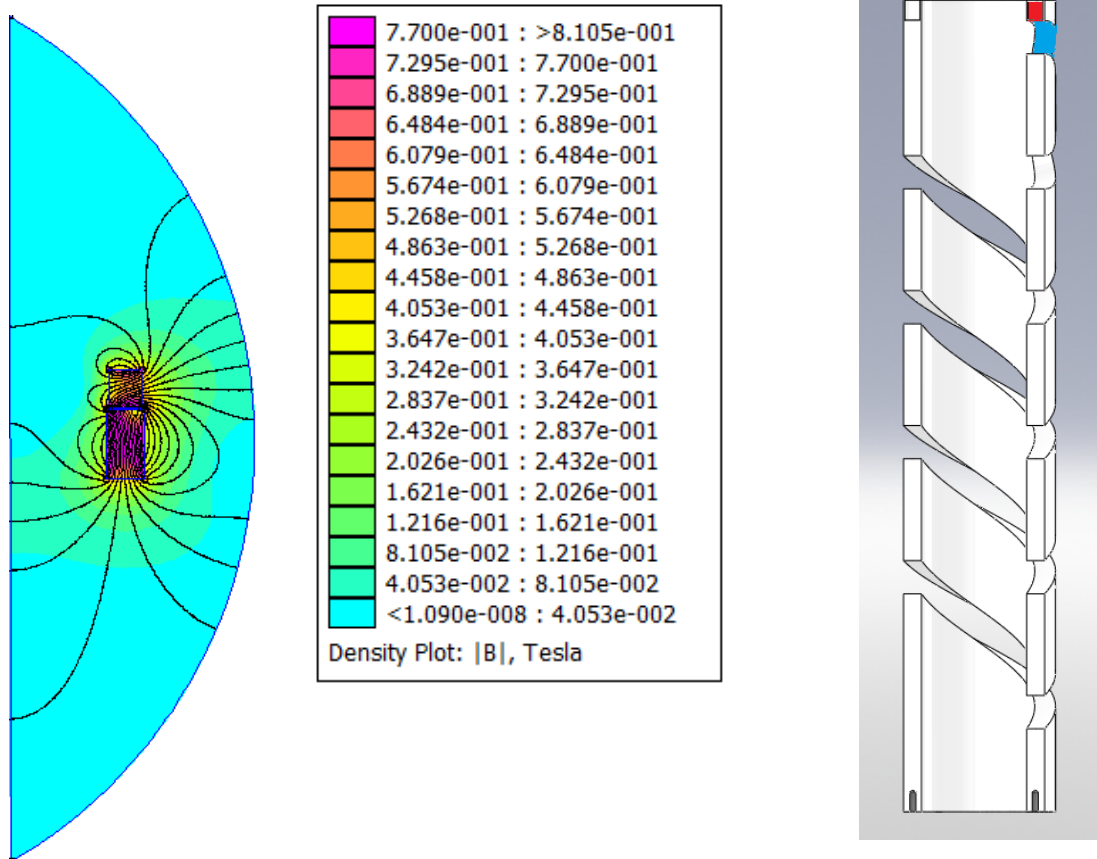
Figure A.2 Interaction between spiral of NdFeB and layers of NdFeB placed on the top of the crown.
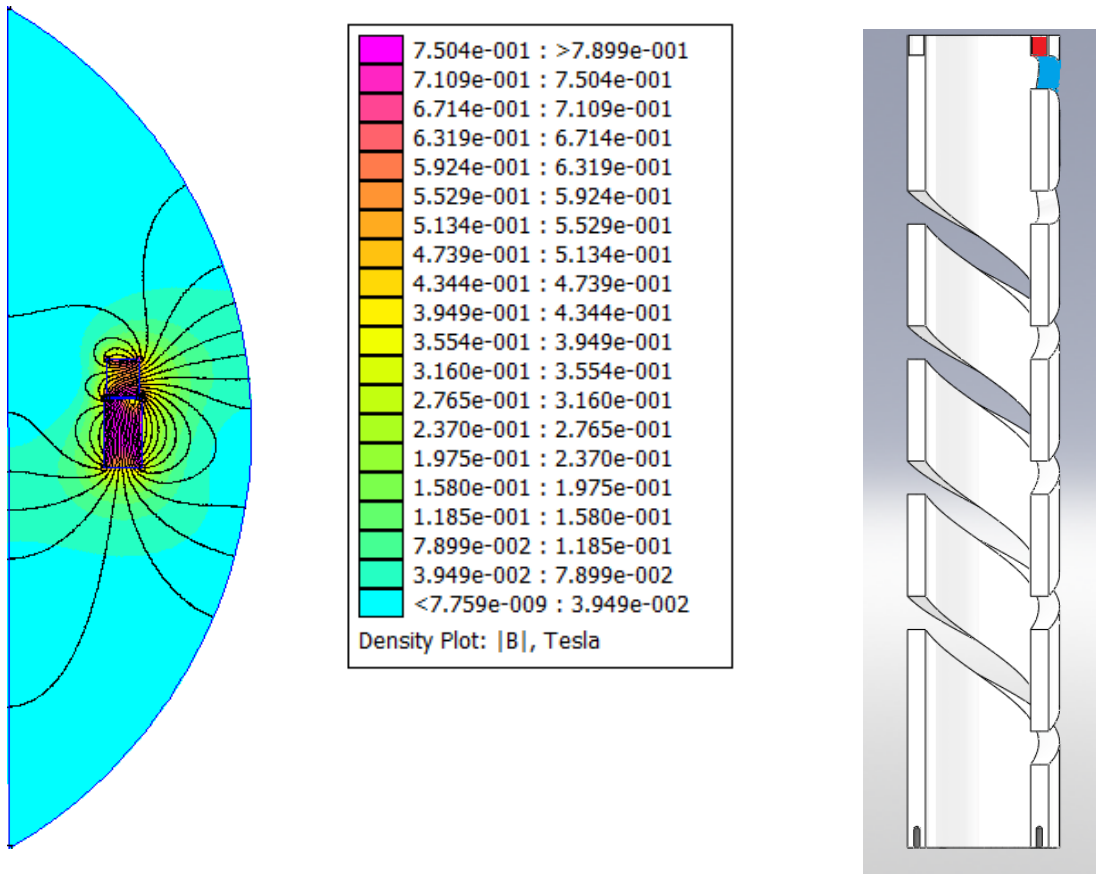
Figure A.3. Interaction between spiral of NdFeB and layers of NdFeB placed on the top of the crown.

From previous figures it was possible to study the magnetic field generated by turns of magnetic material. It was extremely important to see the magnetic field lines by placing of a crown made of NdFeB (Plastimag). After this studies it was possible to have an idea about the distance between the spiral configuration and magnets placed on the top of the magnetic path.

Due to Pastimag is industrially sold as a coil, it was also important to understand how many tuns generate a strong plasma confinement.

Following figures show the different magnets configuration to be placed on the top of the magnetron body.
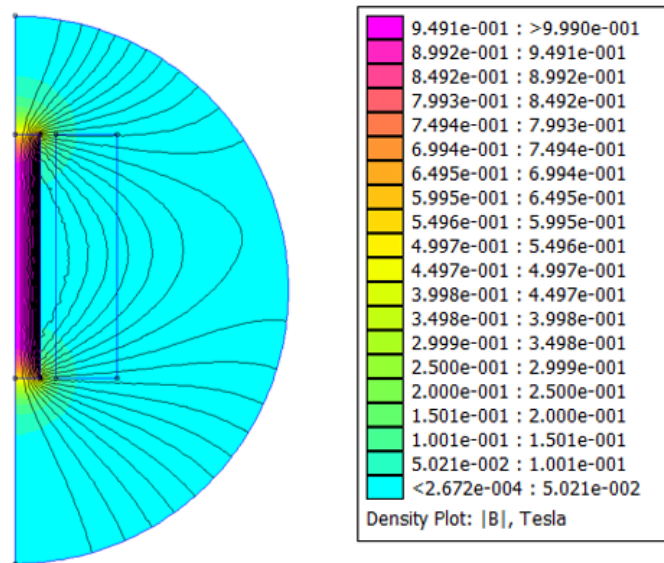
Figure A.4 NdFeB (D=5mm)-Air.
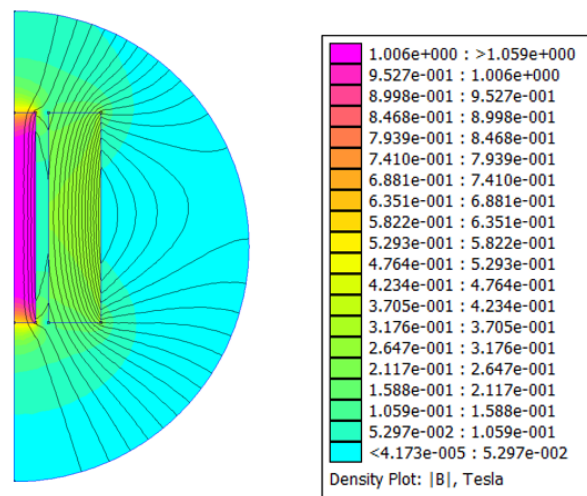
Figure A.5. NdFeB (D=5mm) - Plastimag (Dext= 20mm).
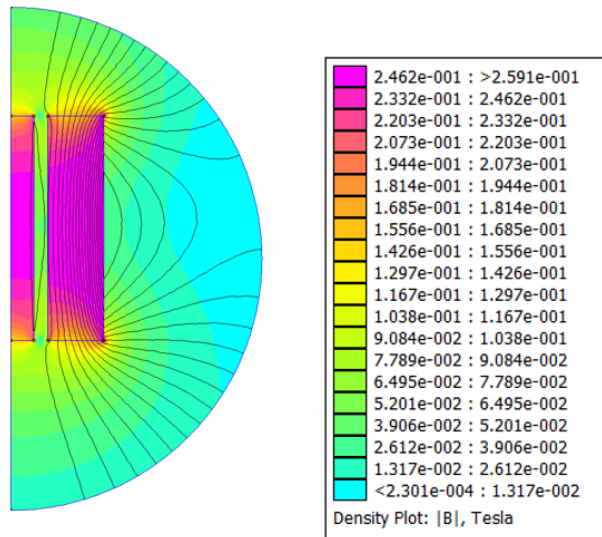
Figure A.6. Plastimag (D=5mm)-Plastimag (Dext=20mm).
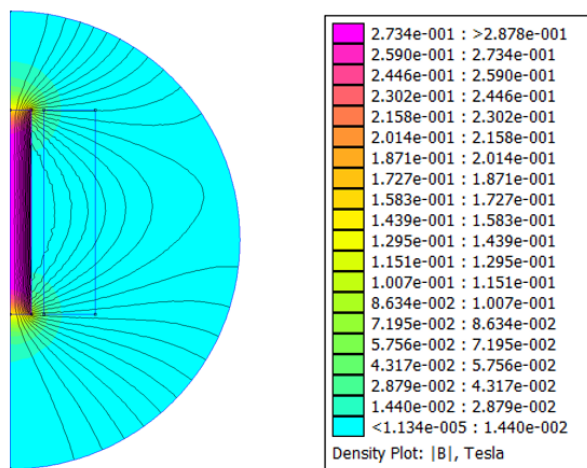
Figure A.7. Plastimag (D=5mm)- Air.
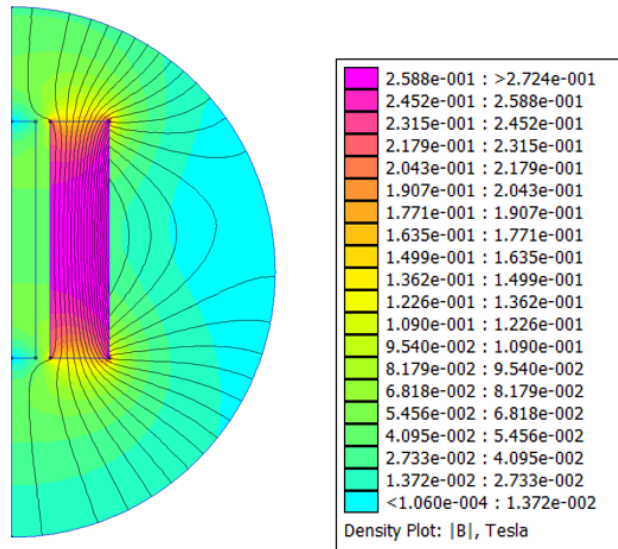
Figure A.8. Air- Plastimag (Dext=20mm).
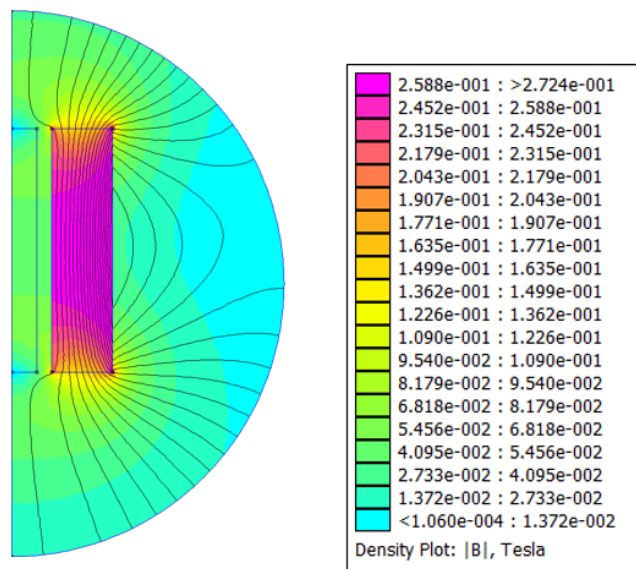
Figure A.9. NdFeB (D=5mm) - Plastimag (Dext= 20mm).
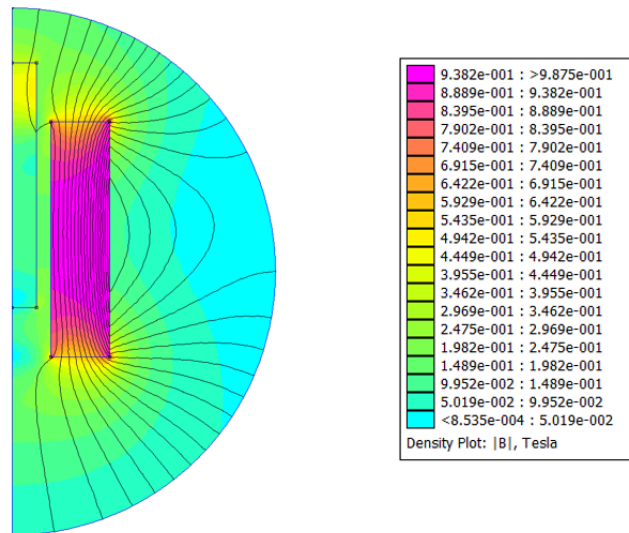
Figure A.10. Plastimag (D=5mm) - NdFeB (Dext= 20mm).
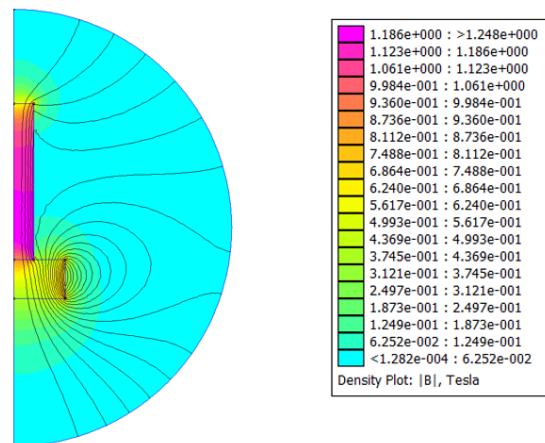
Figure A.11. NdFeB (D= 5mm)-NdFeB (D=6,4mm, h=4,8mm)

Last magnetic confinements helped to understand the most convenient magnets in order to be used in a second magnetic path placed over the spiral. Then it was compared the magnetic field lines generated by permanent magnets and the magnetic field lines generated by Plastimag material.

APPENDIX B

Following figures presents the element picks obtained in order to analyze the impurity content during after the vacuum pumping
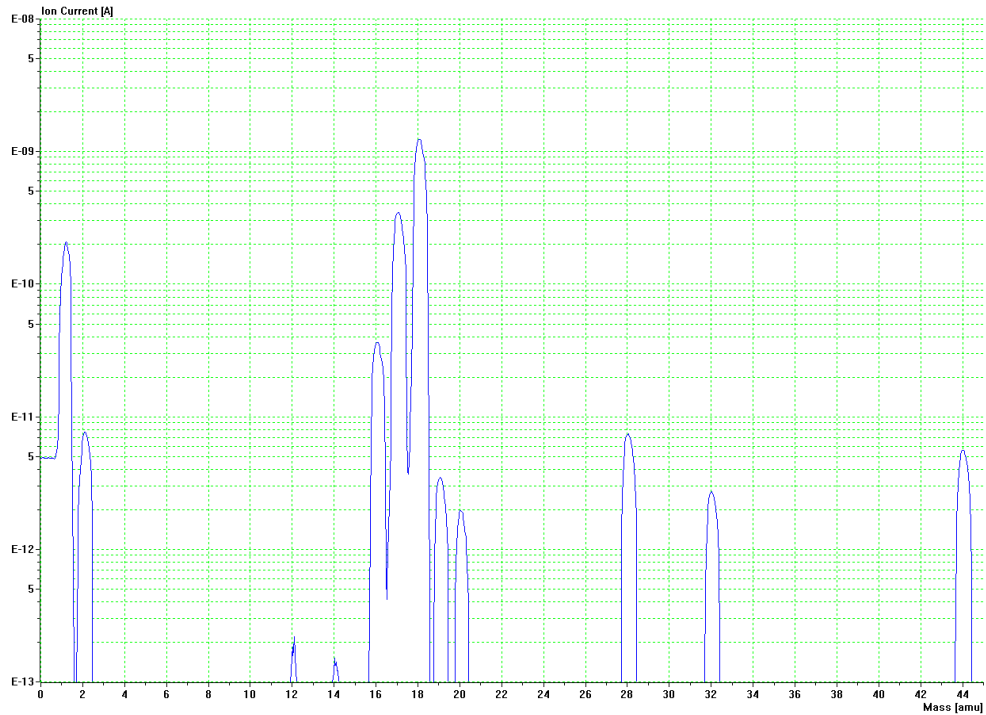
Figure B.1. Gas analyzer before baking.
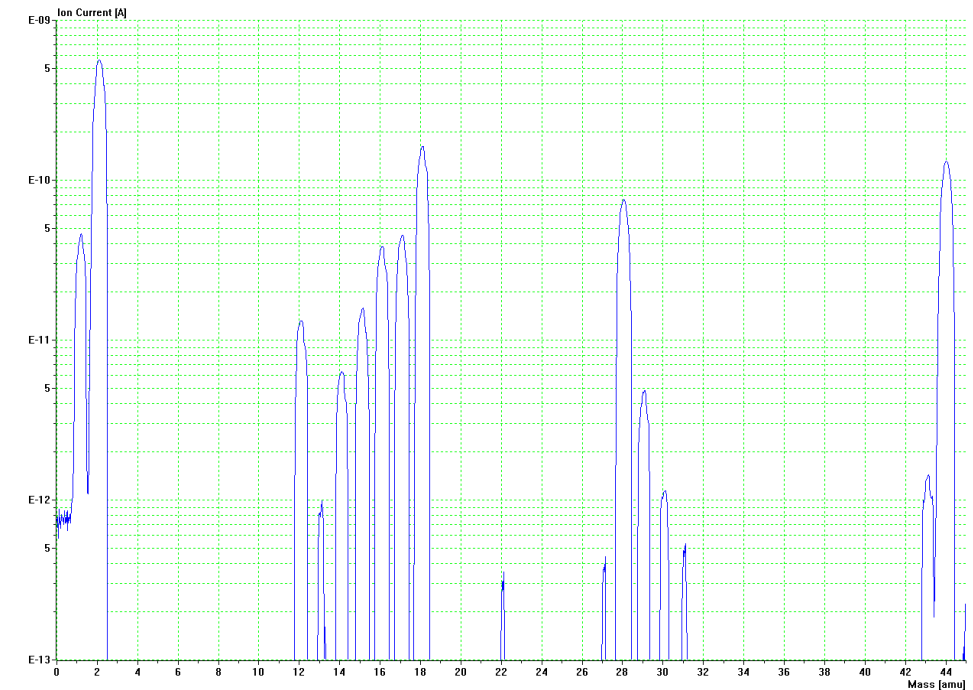
Figure B.2. Gas analyzer after 48 hours baking.
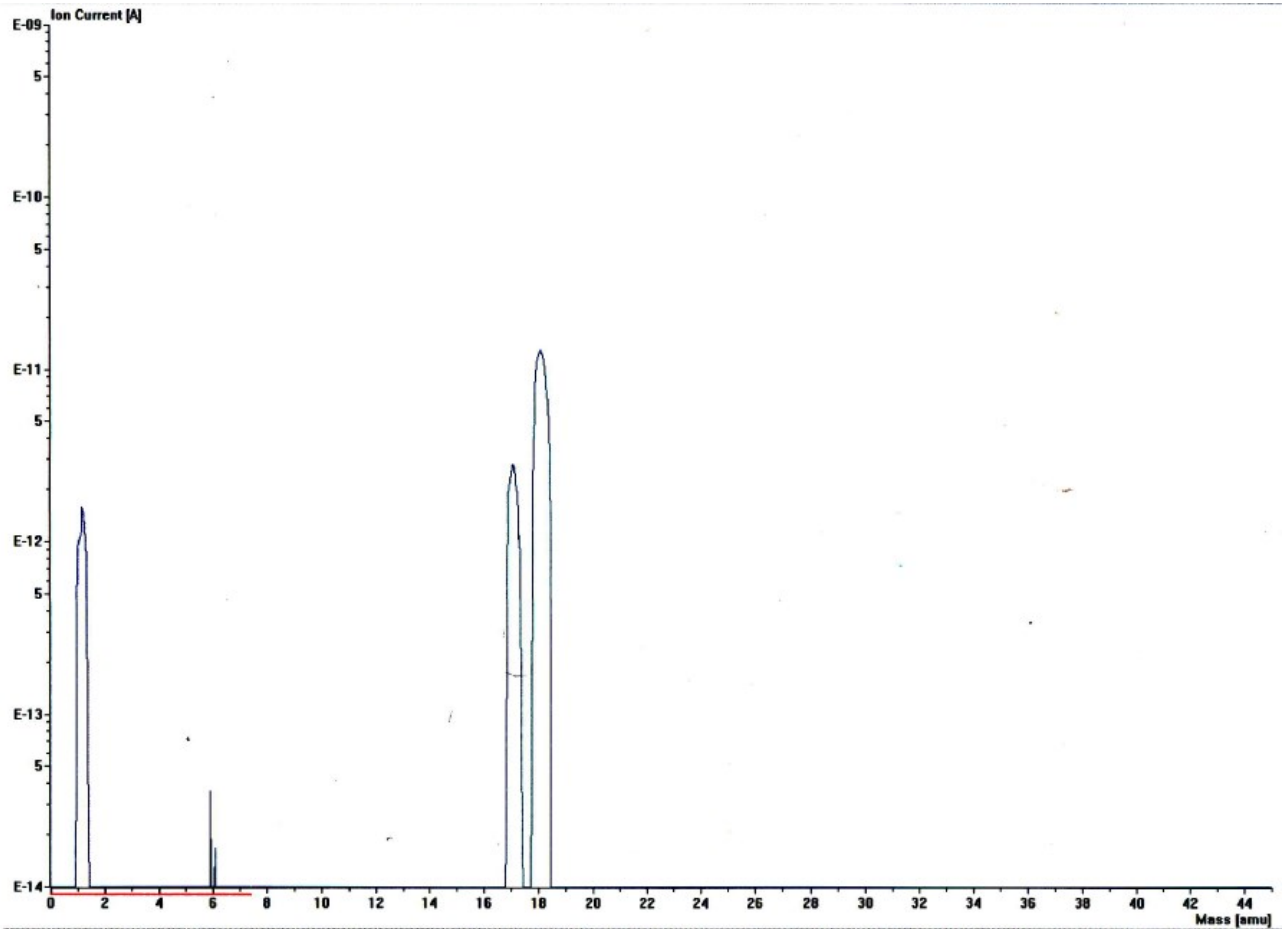
Figure B.3. Scanning of the system (58h baked) @25°C.

Last figure shown the presence of impurities inside the vacuum chamber before the thin film deposition. The presence of water was quite common due to each substrate was washed in an ultrasonic bath before generating the vacuum. For this reason, it was necessary to improve outgassing of the camera with a baking process.

APPENDIX C

Following figures show the 3D drawings of the QWR cryostat stand.
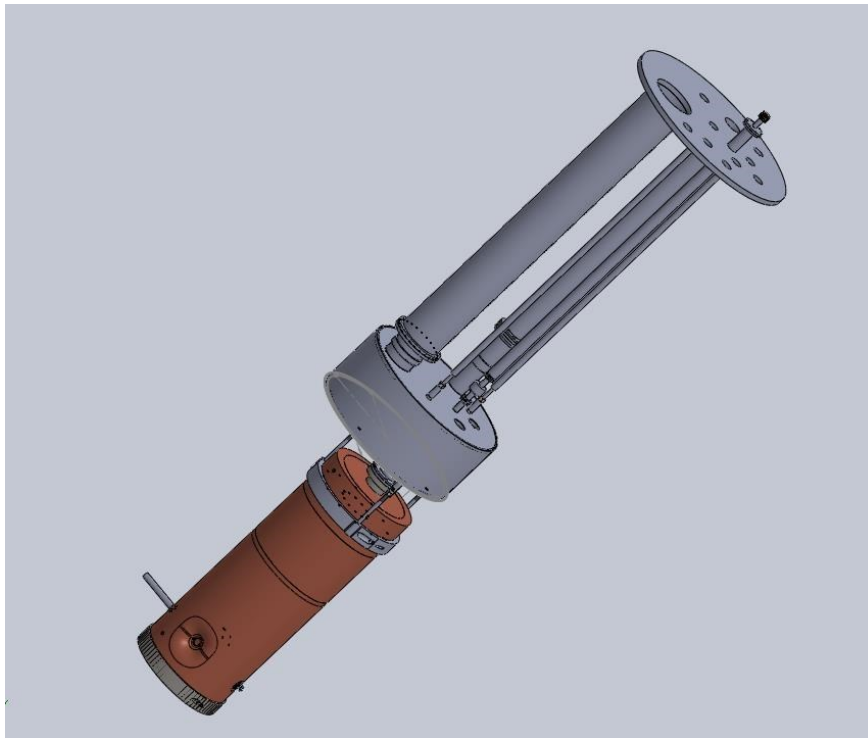
Figure C.1 side view of the cryostat stand.
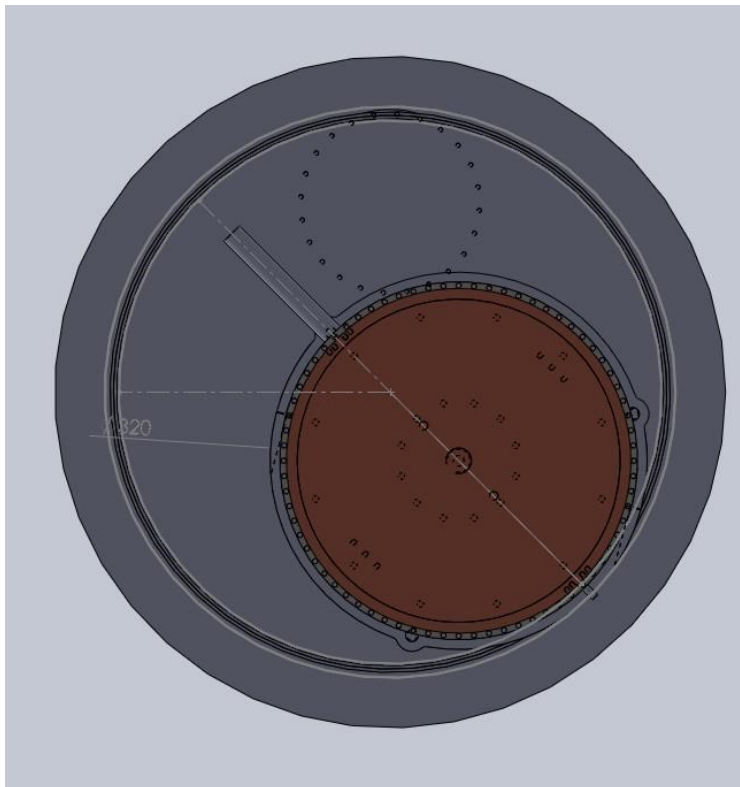
Figure C.2. Bottom view of the cryostat stand. The cavity is not centered in order to connect the coupler antenna.
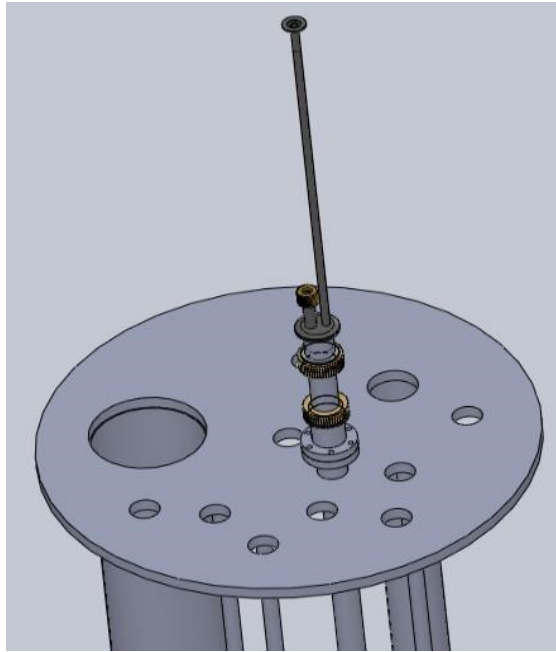
**Figure C.3 Liquid Helium transfer line.**
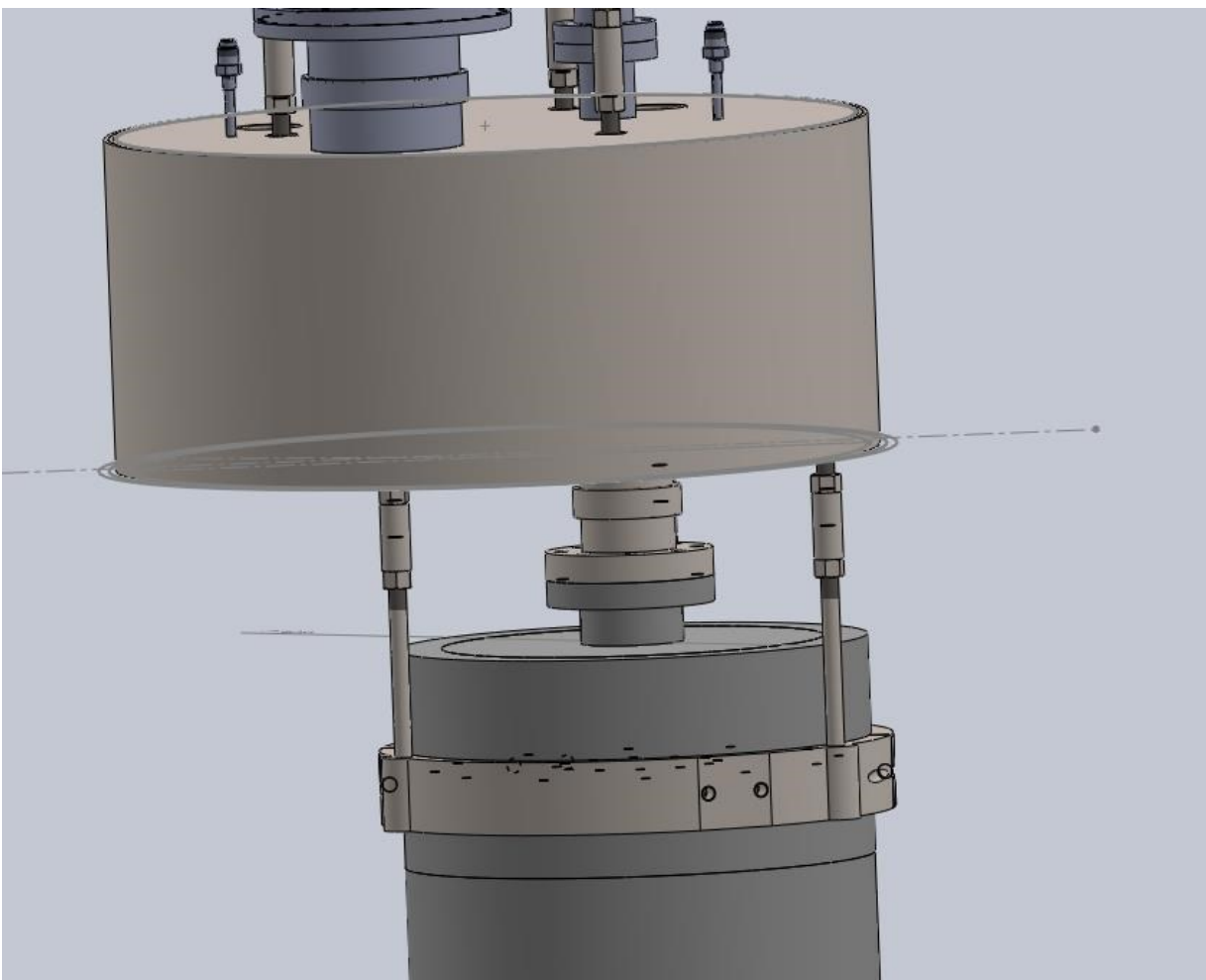
Figure C.4. QWR holder.

153
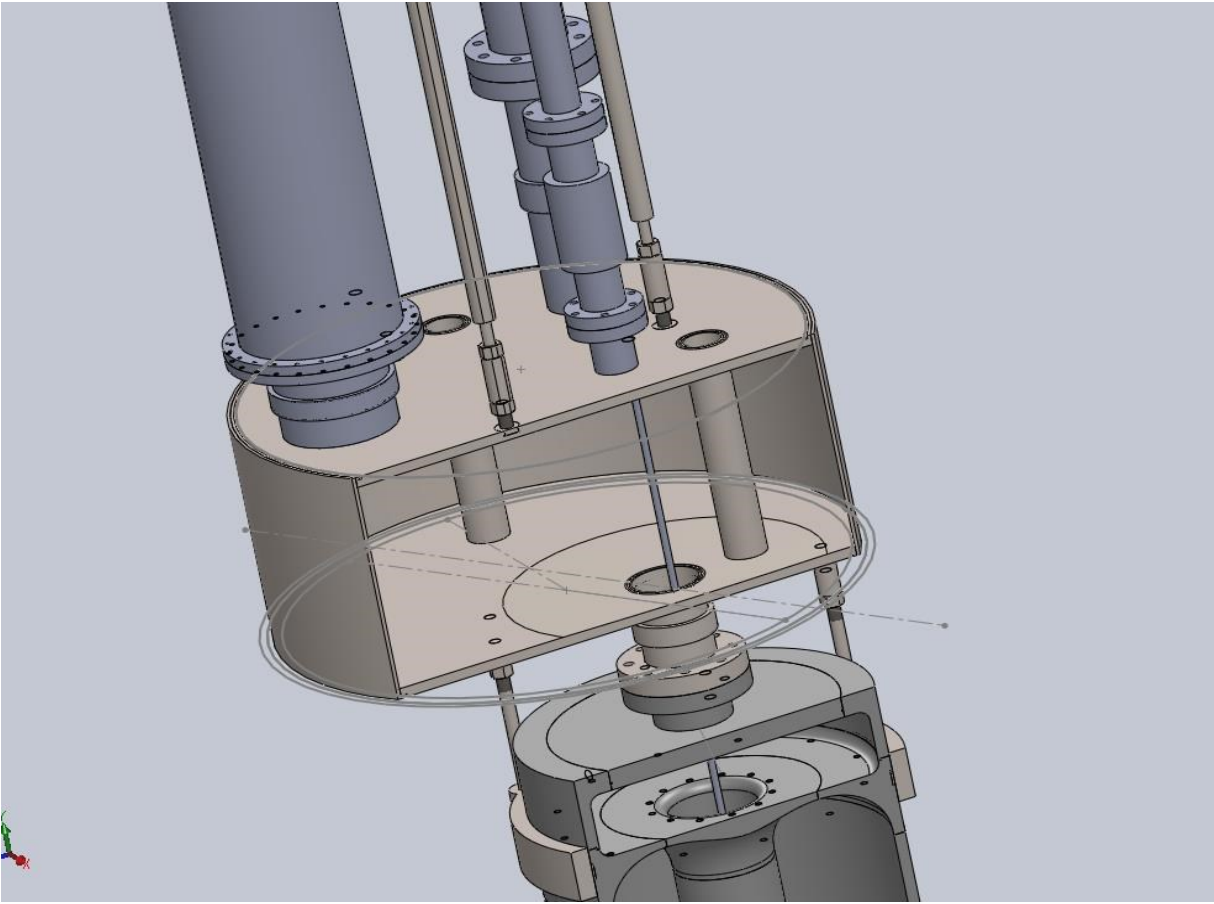
Figure C.5. Cross view of the Helium tank